Irradiators for Measuring the Biological Effects of Low Dose-rate Ionizing Radiation Fields

by

Matthew Allen Davidson

B.S., Chemical Physics (2005)
Catholic University of America

SUBMITTED TO THE DEPARTMENT OF NUCLEAR SCIENCE AND ENGINEERING IN PARTIAL FULFILLMENT OF THE REQUIREMENTS FOR THE DEGREES OF

MASTER OF SCIENCE IN NUCLEAR SCIENCE AND ENGINEERING

AT THE

MASSACHUSETTS INSTITUTE OF TECHNOLOGY

JUNE 2011

Signature of Author: ....
Matthew Allen Davidson
Department of Nuclear Science and Engineering
May 31, 2011

Certified by: ....
Jacquelyn C. Yanch
Visiting Scientist, Department of Nuclear Science and Engineering
Thesis Supervisor

Read by: ....
Richard C. Lanza
Principal Research Scientist, Department of Nuclear Science and Engineering
Thesis Reader

Accepted by: ....
Mujid S. Kazimi
TEPCO Professor of Nuclear Engineering
Chair, Department Committee on Graduate Students

Irradiators for Measuring the Biological Effects of Low Dose-rate Ionizing Radiation Fields

By

Matthew Allen Davidson

Submitted to the Department of Nuclear Science and Engineering
on May 9, 2011 in Partial Fulfillment of the
Requirements for the Degree of Master of Science
in Nuclear Science and Engineering

Abstract

Biological response to ionizing radiation differs with radiation field. Particle type, energy spectrum, and dose-rate all affect biological response per unit dose. This thesis describes methods of spectral analysis, dosimetry, biological assays, and mathematical modeling for determining the relative biological response for low dose-rate fields.

The spatial dimensions of optically stimulated luminescence dosimeters make them ideal for measuring dose at a specific location. However the response of these dosimeters varies with photon energy. A method is presented for measuring dose delivered by several fields with photon energies less than 60 keV using these optically-stimulated luminescence dosimeters. This method is confirmed using an ion chamber dosimeter and computer simulation. The construction of ^{241}Am irradiators for tissue culture and animal experiments using this dosimetry method is also described. The results of tissue culture experiments performed using these irradiators are presented, and the relative biological effectiveness (RBE) is determined for two fields with approximately equal dose-rates produced by shielding ^{241}Am foil sources with aluminum and polyethylene.

Biological effects can result from single instances of energy deposition within a cell or from the combination of separate instances, but at low dose-rates biological repair mechanisms reduce the probability of effects resulting from the combination of separate instances. At a sufficiently low dose-rate the effects due to combination of separate instances are negligible. A model of low dose-rate energy deposition within a cell nucleus was developed to determine this dose-rate. In this model the proportion of biological effects due to single instances of energy deposition within a cell nucleus is described in terms of the DNA repair rate of the biological system and the dose-rate and lineal energy transfer of the radiation field. This model also describes the projection of RBE values for fields with dose-rates below this threshold.

Thesis Supervisor: Dr. Jacquelyn Yanch
Title: Visiting Scientist, Department of Nuclear Science and Engineering

Acknowledgements

This project could not have been completed without the support of many people at the Institute and beyond. I am extremely grateful to everyone who has helped prepare me for this project and complete the work described in this document. Most importantly my thesis supervisor, Dr. Jacquelyn Yanch, deserves much credit for making this project a success. She went above and beyond her duties by continuing to provide guidance for this project even after leaving her post as Professor of Nuclear Science and Engineering. Also I must thank my thesis readers, Dr. Richard Lanza and Prof. Bevin Engelward, for their helpful critiques, advice, and encouragement.

Bill McCarthy, Deying Sun, and especially Mitch Galanek of the MIT Radiation Protection Office deserve recognition for their commitment to finding ways to conduct all radiation experiments safely and also for loaning essential dosimetry equipment and sources. Also Rachel Batista was essential in helping me acquire experimental supplies. Her kindness and compassion is greatly appreciated.

I must also thank Anurag Maheshwari, David Weingeist, Orsolya Kiraly, Werner Olipitz, James Mutamba, and Michelle Sukup Jackson for teaching me excellent techniques for experimental biology and providing helpful discussions concerning DNA damage and repair.

Beyond these people at the Institute many others deserve recognition. I am grateful to Prof. David Brenner for providing comments on my thesis draft. Also I must recognize my undergraduate research advisors Prof. Leopold May, Prof. Robin Selinger, and Prof. Gavin Brennen. Thanks to their guidance and encouragement, I realized the joy of scientific discovery and chose to pursue graduate studies in science.

The many friends whom I have met along the way were also helpful in providing advice, support, and entertainment. Jennifer Anttonen deserves credit for convincing me that anything that went wrong was always my fault.

Finally I must thank my family in Alabama, who worked hard to give me opportunities that they never had. I dedicate this thesis to my parents, Mitchell and Linda Davidson.

Table of Contents

Chapter 1: Introduction and Background

1.1 Introduction

The biological effects of ionizing radiation have been shown to vary with particle type, energy spectrum, and dose-rate of a radiation field. Many studies have examined the relative biological effects of different radiation fields at acute dose-rates (~1 Gy/min). However fewer studies have examined the relative biological effects of radiation fields at lower dose-rates (< 100 cGy/h). Instead of measuring these effects experimentally at lower dose-rates, the relative biological effects are often predicted based on biological data observed at acute dose-rates.

This thesis describes methods of experimentally determining relative biological effectiveness (RBE) for low dose-rate fields using spectral analysis, dosimetry, biological assays, and mathematical modeling. Using these methods it is possible to determine RBE for low dose-rate fields without estimation based on biological data from acute exposures.

These methods are demonstrated using low dose-rate fields from ^{241}Am sources. These ^{241}Am foil sources described have great potential for applications in radiobiology research. There are many unanswered questions concerning the biological effects of low-energy (10-60 keV) photon radiation at low dose-rates, and these sources provide a radiation field capable of addressing these questions.

In order to design experiments to answer these questions, it was necessary to characterize the photon field emitted by these sources. Since no standard method existed for performing this characterization for 10-60 keV photons, several detectors and dosimeters were used. This characterization is presented in Chapters 2 and 3.

With this characterization performed it was possible to design irradiators to be used in biological experiments. Tissue culture irradiators were designed for the purpose of measuring the relative biological effectiveness of the different photons emitted by the ^{241}Am foil sources. The design and implementation of these irradiators is described in Chapter 4. Animal irradiators were also designed for the purpose of measuring the effects of long-term low dose-rate radiation exposure in mice. These irradiators are described in Chapter 5.

Before considering these sources specifically, it is important to understand the motivation for their development. The following chapter is a review of relevant background material and previous studies of the biological impact of radiation which have provided this motivation.

1.2 Overview of the Biological Effects of Ionizing Radiation

Ionizing radiation has been used for biological applications for decades. Its ability to fatally impact biological systems is employed in the field of medicine to treat cancer and in industry as a means of sterilizing food and supplies. Beyond these applications there are many other biologically relevant applications which do not result in death of the cell or organism involved. Humans may absorb radiation from these applications and from other environmental, occupational, or accidental exposures which are described below. In the following sections the amount of radiation absorbed is quantified in terms of dose and equivalent dose.

Dose is a quantity defined as the amount of energy absorbed per unit unit of mass. Dose data reported in this study are in terms of gray (Gy), which is defined as one Joule of energy deposited per kilogram of mass. Other data in this study are reported in terms of equivalent dose. Equivalent dose quantifies biological impact as well as energy absorbed. Since some types of radiation have been observed to have a greater impact on biological systems per unit energy absorbed, dose equivalence is defined as the dose multiplied by a quality factor which describes the degree of this impact. For photons this quality factor is 1, but quality factors are as high as 20 for heavy charged particles. Dose equivalence data are reported in units of sievert (Sv), which is 1 J/kg quality-corrected.

1.2.1 Instances of Exposure

Doses slightly above natural background levels may be used to provide diagnostic images of biological systems. X-ray computed tomography imaging, x-ray absorption imaging, and positron emission tomography scanning are all examples of beneficial applications of sublethal levels of radiation.

Beyond these applications, humans are exposed to radiation in many other ways. Humans are constantly exposed to background radiation from cosmic rays. Exposure to cosmic radiation is elevated at higher altitudes and greater distance from the earth's equator. For this reason, taking high-altitude flights increases exposure.

Humans may also be exposed to radiation from radionuclides in the environment, such as granite stonework which contains trace amounts of uranium. Humans may also be exposed to radiation from security scanning devices, as part of an occupation, in an accident, or due to terrorism.

Many workers require some degree of radiation exposure, including pilots, flight attendants, radiotherapists, x-ray technicians, and workers in the nuclear power industry. The radiation dose received by these workers is typically monitored and limited, but these limits are based on risk estimates determined using a limited set of biological data as described below.

Several instances of accidental radiation exposure have been recorded since work with nuclear technology began late in the 19th century. Nuclear waste and fuel processing sites have leaked radionuclides into the surrounding environment. Workers have ingested radionuclides without realizing the possible harmful effects. Animals have ingested radioactive material near nuclear facilities and subsequently been eaten by humans. Radionuclides have been melted down with scrap iron and forged into steel for use in construction.

Nuclear reactor accidents such as those events at Three Mile Island and Chernobyl have the potential to release large amounts of radioactive material (13 million curies from Three Mile Island [1] and 4.5 billion curies from Chernobyl [2]) into the environment. In the case of Chernobyl, some nearby areas containing more than 40 curies of ^{137}Cs per square kilometer have been confiscated and closed by the Ukrainian government [3]. All entry into these areas has been illegal for decades, resulting in the displacement of 336,000 people [2].

To date no radioisotopes have been released into the environment as part of a terrorist attack; however, the danger persists. Such an attack could contaminate a populated area with radioisotopes which would expose everyone in the area and could necessitate evacuation and decontamination. Under current annual dose limits set by the Nuclear Regulatory Commission (100 mrem/year for the general public [4]), any attack could result in forced evacuations and property confiscations in the surrounding area, which could have a large economic impact.

The annual dose limits set by the Nuclear Regulatory Commission (NRC) are based on experimental data obtained by observing cancer incidence in the population of atomic bomb survivors. The model used to set these limits estimates the dose delivered to an individual survivor and correlates the dose received with the probability of developing cancer among the survivors. This model ignores the effects of dose-rate and photon energy and considers only the estimated dose received.

With this limitation of the current risk model and the potential consequences of its inaccuracy in mind, it was the goal of this study to develop and analyze radiation sources that will enable researchers to broaden this set of biological data in ways that had not previously been possible. In order to accomplish this goal effectively, previous research efforts that have generated relevant biological data were considered. Sections 1.2 and 1.3 below describe several studies which show that dose-rate and energy are important in determining biological effects of radiation.

Many studies have been conducted to attempt to gather a better understanding of the biological impact of ionizing radiation. Some of these studies have focused on the low dose-rate photon radiation similar to that considered in this thesis. Other studies have focused on different types of radiation with higher dose-rates, but in general much of what has been inferred about the mechanism of biological impact is valid for all types of radiation. The experiments conducted in this study were designed with the intent of generating data which would provide greater insight into these mechanisms. An outline of the mechanisms of biological impact of ionizing radiation is presented in the following section.

1.2.2 Mechanisms of Biological Impact of Ionizing Radiation

The physical mechanisms of biological impact of ionizing radiation may be divided into two types: direct action and indirect action. Direct action is defined as the direct interaction of an incoming ionizing particle with a bio-molecule. Indirect action is defined as the interaction of a bio-molecule with a free radical intermediate created by ionizing radiation rather than with the ionizing particle itself [5].

Radiation may ionize atoms that make up the molecules of DNA or other important molecules within a cell. When these ionization events occur, the covalent bonds between atoms in the DNA sugar phosphate backbones may be broken. The hydrogen bonds between base pairs in the DNA structure may also be broken. Other interactions with bio-molecules may also result, such as the cleaving of covalent bonds within RNA molecules proteins. When these molecules are damaged, cellular functions may be inhibited or interrupted resulting in cell cycle delay or inability to reproduce.

These bonds may also be broken by secondary and tertiary particles produced by ionizing radiation. DNA and other biological molecules make up a small fraction of the mass of a cell relative to the water within the cell, so ionizing radiation is much more likely to ionize atoms within water molecules than those atoms within the DNA structure. Radiation may ionize both hydrogen and oxygen atoms within water molecules to produce a variety of ionized molecules, secondary and tertiary electrons, and other radicals. Some of these species are shown in Table 1. Radiation may also ionize other molecules within cells such as lipids and sugars, but these ionization events are less likely than ionization of water due to the proportion of water within the cell.

Name	**Formula**
Hydrogen peroxide	H_2O_2
Hydroxide radical	$HO\bullet$
Superoxide anion-radical	$O_2^-\bullet$
Hydronium	H_3O^+

Table 1. Reactive oxygen species created by ionization of water.

As these unstable chemical species are produced, they interact with other neighboring molecules. In some cases, these molecules are DNA, RNA or other molecules with a biological function. In other cases, these chemical species interact amongst themselves, producing stable species that do not interact further with bio-molecules.

The number, type, and concentration of chemical species produced varies with the energy, type, and dose-rate of ionizing radiation producing them. This study focuses on photon radiation only, which can give rise to different concentrations of chemical species depending on the energy of the photon. The dose-rate and photon energy are varied, different chemical and physical effects are predicted, and different biological effects are observed. These observations are discussed in the sections below.

1.3 Biological Effects of Rate of Delivery of Ionizing Radiation

Many studies have considered the impact of ionizing radiation at varying dose-rates. In the following section, literature data along with relevant experimental details are presented. Others who have compiled similar data sets [6] have found that there is a correlation between dose-rate, rate of proliferation, and rate of repair of sublethal damage. For the purposes of comparison these details have been noted as well as the type and energy of radiation involved. Also explained is the unique ability of the ^{241}Am sources to provide useful information to supplement the available findings to yield a more complete understanding of biological effects at low dose-rates.

1.3.1 Biological effects of Low Dose-rate Radiation on Cells in Culture

In 1973, Bedford and Mitchell studied the effects of dose-rate on clonogenic survival of CHL-F cells [7]. This variant of the CHL3-J3 cell line had a cell-cycle time of approximately 16 hours. They found that for cells exposed to the same amount of dose, survival was influenced by the dose-rate at which the dose was delivered. They found orders of magnitude of difference in survival for a total dose-rate of 2.5 Gy of ^{60}Co lead-filtered gamma photons between cells irradiated at dose-rates of 0.36 cGy/min and 16 cGy/min as illustrated in Figure 1.

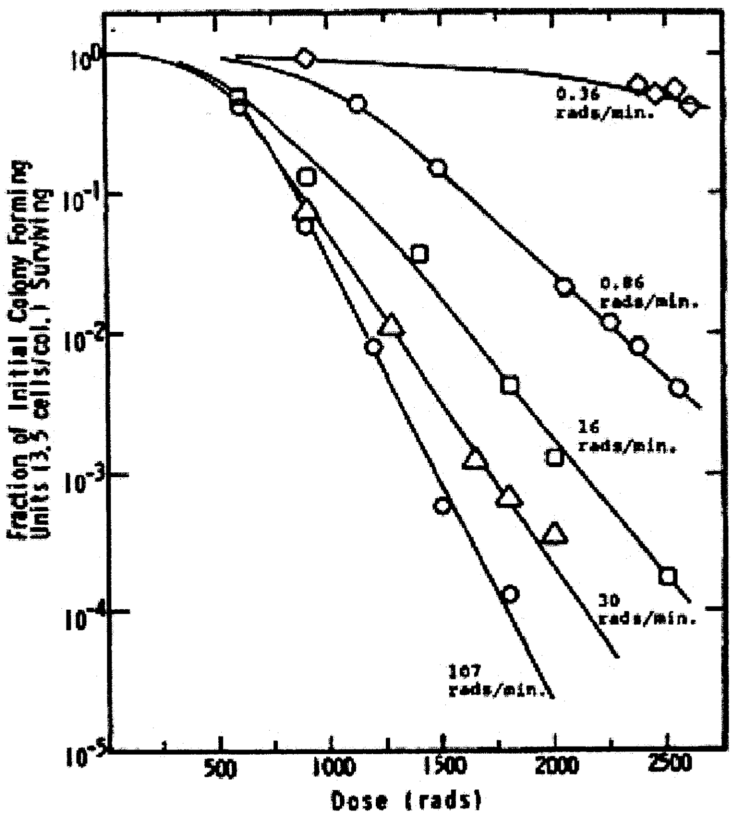

Figure 1. Survival curves for CHL-F cells at various dose-rates of ^{60}Co gamma photons.

This study clearly illustrated that survival is dependent on dose-rate over the range of doses in question for this particular cell and radiation type. S3 HeLa cells, with a doubling time (DT) of 22 hours, mouse LP59 (DT=22 hours), Indian mutjac (DT=28 hours), Chinese hamster V79 (DT=10 hours), rat kangaroo (DT=31 hours), and pig kidney cells (DT=26 hours) were also cultured under varying dose-rates of ^{137}Cs gamma photons and found to have dose-rate dependence as well [7]. One notable feature of the data presented in this study is the minimal sensitivity of the V79 relative to the other cell types, which may be due to its faster rate of proliferation. These findings show that dose-rates as low as 22 cGy/h, a factor of 10 greater than the dose-rates delivered by a single ^{241}Am foil source, are capable of reducing cell survival.

Apoptotic response has been directly measured using the TUNEL assay, a method of detecting DNA fragmentation by labeling the terminal end of nucleic acids, for dose-rates of 4.3 and 48 cGy/h delivered to HeLa-Hep2 cells by a ^{60}Co source. H. Mirzaie-Joniani et al. found that doses of 2 Gy delivered at 4.3 cGy/h yielded increased apoptosis over non-irradiated controls and that the percentage of apototic cells varies with time after irradiation and total dose delivered at constant dose rate [8]. The study shows evidence of a measurable biological effect at dose-rates of 4.3 cGy/h, a factor of 2 different from the dose-rate delivered by a single ^{241}Am foil.

Ueno, Furuno-Fukushi and Matsudaira found a variation in micronuceli formation, cell killing, and mutation for L5178Y mouse lymphocytic leukemia cells exposed to both ^{60}Co gamma photons and tritiated water at dose-rates ranging from 12-48 cGy/h [9]. An analysis of the relative biological effectiveness of these radiation fields will be considered in the section on relative biological effectiveness. The data presented in this study show significant differences in survival for different dose-rates. For example survival for 6 Gy of ^{60}Co gamma photons differs by more than a factor of 10 for the 12 and 48 cGy/h cases. This result illustrates the large differences in biological impact for different dose-rates. The ^{241}Am foils could be implemented to perform similar experiments at dose-rates of 2 cGy/h and below.

The data mentioned thus far have presented an overall trend of increased survival or lessened biological impact for lower dose-rates. However, this trend is contradicted by other findings. In cell culture studies, some researchers have found evidence of an inverse dose-rate effect in which lower dose-rates sometimes result in lower survival than the same dose delivered at a higher dose-rate.

One example of this inverse dose-rate effect is presented by Mitchell, Bedford, and Bailey [10]. In this example HeLa cells were found to exhibit a lower percentage of survival when irradiated by a ^{60}Co source at 37 cGy/h relative to 74 cGy/h at total accumulated doses above 1.4 Gy. The authors suggested that this effect may be due to cell cycle timing delays which result in more damage occuring in a prolonged G2 phase. DeWeese found an inverse dose-rate effect for six human prostate carcinoma cell lines (LNCaP, DU 145, PC-3, PPC-1, and TSU-Pr1) irradiated with ^{60}Co gamma photons at dose-rates of 25 cGy/h and 1 Gy/min but did not find accumulation in the G2 phase in this case, suggesting that another mechanism is needed to explain the case of these cell lines [12]. This inverse dose-rate phenomenon and the mechanism producing it could be investigated at lower dose-rates with the ^{241}Am foil sources.

Mitchell, Folkard, and Joiner irradiated PC3, T98G, and A7 cell lines at dose-rates 2-100 cGy/h with a ^{60}Co source [11]. These cell lines had previously been shown to exhibit hypersensitivity, a greater biological response to low doses of radiation relative to higher doses. These cells exhibited an inverse dose-rate effect in which lower dose-rate radiation produces greater biological effects than higher dose-rate radiation per unit dose. Another another cell line, U373MG, which had not exhibited hypersensitivity did not exhibit the inverse dose-rate effect. No accumulation in the G2 phase of the cell cycle was found for any of these cell lines. The study of the link between hypersensitivity and the inverse dose-rate effect is another potential application of the ^{241}Am foils.

Studies involving mice have revealed large variations in response to low dose-rate radiation. In the section below, some of these examples are considered.

1.3.2 Effects of Low Dose-rate Ionizing Radiation on Mice

Many studies of mice exposed to low dose-rate radiation have been reported. This section is a summary of some of these studies which have motivated the work with ^{241}Am foil sources. In these studies the type of mouse, source of radiation, dose-rate and total dose are varied. These factors have been included in the data below in order to present a collection of the relevant data which could explain variations in response to radiation in mice.

In some studies, the biological effects of low-dose rate radiation exposure have been seen as protective, inducing greater immune response or longevity. In other studies, low-dose rate radiation has been seen to produce tumors and produce other harmful effects.

One such study revealing the possibility of radiation-induced tumors at low dose-rates is that performed by Gragtmans et al. [13]. The authors investigated the effects of 0.3-2.0 Gy of 200 kV photons delivered over a period of 10 days. This study showed an increase in the incidence of tumors with dose-rate as well as total dose accumulated. Using ^{241}Am, a similar experiment examining tumor incidence could be performed for the purpose of comparison of the effectiveness of 200 kV photons relative to the lower-energy ^{241}Am photons. It would also be possible to consider a wider range of dose-rates over longer periods of time with the ^{241}Am foils.

Yamamoto, Seyama, Jo, Terato, Saito, and Kinomura considered dose-rates of 0.1-2 cGy/h delivered to C57BL/6N and C3H/He female mice by tritiated drinking water [14]. These dose-rates resulted in a 70-80% incidence of tumor development. Thymic leukemia was found to be the main cause of death for the dose ranges from 0.2-1 cGy/h, but the incidence of thymic lymphoma was sharply reduced below 0.2 cGy/h, while the incidence of other tumors increased. This study also brought forward useful comparisons with ^{60}Co gammas which will be discussed in the section below concerning relative biological effectiveness. The ^{241}Am foil sources could be used in similar studies of tumor incidence at dose-rates of 12 cGy/h and below without the radioactive waste generated by tritiated water.

Another study concerning the harmful effects of low dose-rate radiation is that performed by Liu et al. [15]. In this study 200 kV x-rays filtered by 0.5mm Cu were used to deliver doses of 2.5-20 cGy at a dose-rate of 4.5 cGy/h. These studies showed apoptosis increasing with dose from 0-7.5 cGy of radiation 12 hours after exposure in both spermatogonia and spermatocytes. This study could be conducted at lower dose-rates with ^{241}Am to investigate the effect dose-rate on apoptosis of these cells.

Other studies have found evidence of protective effects induced by low-dose rate ionizing radiation. In 1951 Lorenz et al. found evidence of prolonged life-span for mice exposed to 0.11 cGy/day of [16]. This result has been echoed more recently by Lacoste-Collin et al. who studied the effects on 560 SJL/J mice of 10 cGy/year of ^{232}Th in the form of thorium nitrate within plastic bags. The mean energy of this source was 60 keV [17]. They found that life-span was prolonged for irradiated mice. This study illustrates that radiation has been observed to have beneficial effects for some dose-rates. With the ^{241}Am foil sources, dose-rates from natural background rates up to 0.5 cGy/h can be delivered to further investigate any potential benefits of radiation in this low dose-rate range.

In another recent study, Tanaka et al. found no such increase in longevity when 4000 B6C3F1 mice were irradiated at dose-rates of 0.0002-0.0875 cGy/h of ^{137}Cs photons [18]. In the case of the mice irradiated at 0.0875 cGy/h and 0.0458 cGy/h longevity was found to decrease significantly. These data would seem to conflict those findings of increased longevity reported above, but direct comparisons cannot be made since dose-rate, photon energy, and mouse type were not the same in these studies.

From these data it is evident that radiation type and energy, dose-rate, accumulated dose, and mice type may all have some impact on the biological response of mice to low-dose rate radiation. In order to gather the most accurate determination of which factors are most important in determining biological response, it is important to have good experimental control over these factors when conducting experiments. This control has been the goal with the ^{241}Am foil sources in this project. Motivations for their use are presented in section 1.5 below.

1.4 Studies of Relative Biological Effectiveness

Current assumptions about the health risks of exposure to photon radiation have been made based on cancer incidence among atomic bomb survivors who were exposed to photons of energy greater than 1 MeV. No difference in biological effect is assumed for photons of lower energy, although there is much evidence that lower energy photons, especially those photons below 100 keV, have biological effects of greater magnitude per unit dose than photons of higher energies. One of the motivations behind this study is the exploration of this energy dependence of biological effects.

In the following sections biological effects are discussed in terms of relative biological effectiveness (RBE). RBE is defined as the dose of a particular radiation field required to produce the same biological result as a known dose of a reference field.

$$\mathrm{RBE} = \left.\frac{\text{dose}}{\text{reference dose}}\right|_{\text{endpoint}} \tag{1}$$

Several studies have investigated the biological effects of different radiation types and energies. Many of these studies have been conducted at acute dose-rates of approximately 1 Gy/min. Fewer studies have investigated the relative effects of different types of radiation at low dose-rates. In the sections below some of these studies are recounted in order to explain the unique ability of the ^{241}Am foils to provide new data necessary for a greater understanding of the effect of photon energy on biological effects.

1.4.1 RBE at Low Dose-rates

Two studies have compared the biological effectiveness of ^{60}Co photons relative to 5.7 keV tritium betas. Yamamoto et al. [14] studied the life shortening effects in C57VL/6Nx63H/He mice and found that the betas produced greater life-shortening effects per unit dose-rate in the 0.008-0.42 cGy/h range. Ueno et al. [9] studied tritium betas relative to ^{60}Co gammas at dose-rates of 10-40 cGy/h. For L5178Y cells in culture they found RBE values of 1.5 for cell killing, 2.0 for micronuclei formation, and 1.8 for mutation induction.

Although these studies do not compare low dose-rate photon radiation, they provide some insight into the feasibility of observing RBE differences even at low dose-rates. Since 5.7 keV photons are in the same energy range as some of those photoelectrons created by ^{241}Am foils, these data suggest that it is likely that an RBE of greater than one would be observed for these photons even at low dose-rates.

1.4.2 RBE at Acute Dose-rates

Several researchers have attempted to quantify the differences in RBE for photons of different energy. In recent years much attention has been focused on the effects of mammography spectra (16-30 kV) relative to higher photon energies. Low energy photons in the mammography range have been seen to have greater biological effects than photons of higher energies.

Bistrovic et al. analyzed survival of V79 Chinese hamster ovary cells exposed to 20 kV, 70 kV, and 42 MV x-rays as well as ^{60}Co gamma photons and 40 MeV electrons at acute dose-rates (3-5 Gy/min) [19]. They report RBE values of 1.40+/- 0.07 and 1.19+/-0.06 for 20 and 70 kV x-rays respectively relative to ^{60}Co gamma photons.

Panteleeva et al. studied the effects of 25 kV and 200 kV x-rays on clonogenic survival of HEKn, NIH/3T3, and V79 cells [20]. They found for the 10% survival endpoint RBE values of 1.33+/-0.27 for HEKn, 1.25+/-0.07 for NIH/3T3, and 1.25+/-0.07 for V79 cells at 25 kV relative to 200 kV.

Hoshi et al. studied survival of V79 cells exposed to 40 kV, 50 kV, and 180 kV x-rays along with ^{60}Co gammas [21]. For the 10% survival endpoint, they found RBE values of 1.5-1.6 for the lower kV x-rays and 1.29 for the 180 kV x-rays relative to the ^{60}Co gamma photons.

In a review of biological effects seen at different photon energies, M. A. Hill discusses the results of several studies conducted at acute dose-rates. Different cell types and endpoints have been studied for various photon energies, each yielding results which suggest that relative biological effectiveness increases with decreasing photon energy [22]. The general trend is that lower photon energies have higher RBE, but the exact dependence is a function of the endpoint and cell-type studied. Also it cannot be assumed that this RBE as a function of photon energy is monotonic. Kellerer has suggested [23] that inflections may be due to the electron energy spectra produced by photons of various energies.

This energy dependence is explained by density of energy deposition within the biological sample which is quantified in terms of linear energy transfer. Linear energy transfer (LET) is defined as the amount of energy lost per unit length traversed by an ionizing particle.

$$LET = -\frac{dE}{dx} \tag{2}$$

Photons interacting with matter produce ionized atoms and secondary electrons which also transfer their energy to surrounding matter. Tertiary and quaternary electrons may also be produced depending on the energy of the secondary electrons produced. The distribution of energies of these electrons is dependent on the incoming photon energy. This distribution of electron energies determines LET, so LET is dependent on the incoming photon energy and type of material being traversed. RBE is dependent on LET, so electron distributions are important in developing an understanding of the biological effectiveness of different photon energies.

Kellerer discusses the relationship between RBE, electron spectra, and photon energy [23]. He notes that between 20-100 keV there is a transient decrease in electron energy due to a transition from photoelectric effect to the Compton effect. The photoelectric effect is the ejection of an electron from an atom caused by the absorption of a photon, leaving the electron with kinetic energy of the photon energy less the electron binding energy. For low atomic number atoms like those atoms found in tissue, the effect is dominant at lower photon energies (less than 50-60 keV). Above this energy range the Compton effect, which is the partial absorption of photon energy by an electron, becomes dominant. The variation of electron energies due to incoming photon energy is described in Figure 2 reproduced from Kellerer [23].

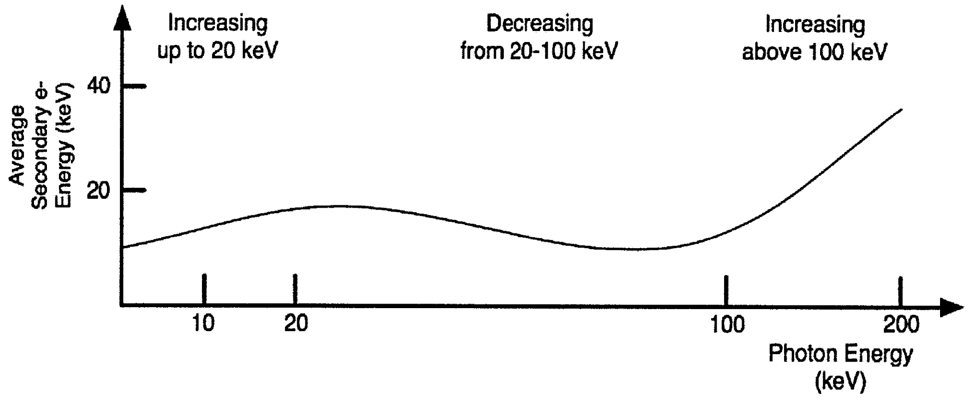

Figure 2. Variation in secondary electron energy as a function of incoming photon energy [23].

The transient reduction in electron energy over the 20-100 keV energy range is an important feature which must be investigated to understand the dependence of RBE for low energy photons. In Kellerer's study to determine RBE for photons of different energies, Kellerer analyzed 30 kV and 200 kV x-ray spectra at acute dose-rates. Using these energy spectra, he found a maximum RBE difference between the two energy spectra of 1.7, but the possibility of an inflection in RBE in the 20-100 keV range was not specifically investigated since the spectra considered were not of appropriate energies to make the comparison. The ^{241}Am foil sources offer the ability to investigate this RBE inflection, since photons are emitted in the 10-26 keV range along with the 59.54 keV gamma photons. This ability is discussed in detail in Chapter 4.

The work of Michalik and Frankenberg also suggests such an inflection in the RBE of photons in the 20-100 keV range [24]. Using the Trion Monte Carlo code, which is designed for simulating radiation action on chemical species, they analyzed the probability of two DNA double strand breaks within a 600-700 nm distance as a function of incoming photon energy. They found a decrease in the number of double strand breaks per unit dose from 30 to 60 keV and an increase from 60 to 100 keV. They simulate the double strand breaks generated by incoming photons in order to gather an understanding of how the secondary electron spectrum generated by incoming photons may influence LET and RBE. In this study, double strand breaks are divided into two categories: simple strand breaks which do not have additional base damage to neighboring bases, and complex strand breaks which have multiple damaged bases in vicinity with double strand break. The results of this simulation are shown in Figure 3. In this Figure, note the inflection of the probability of two double strand breaks in close proximity in the 30-100 keV photon energy range.

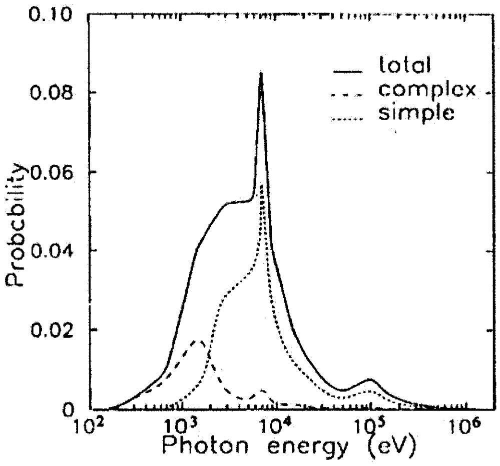

Figure 3. Yields of simple and complex double strand breaks as a function of photon energy [24].

The dependence of LET and RBE on electron spectra has been modeled by Brenner et al. [25]. Using experimentally determined electron spectra generated by various photon energies, they find the lineal energy transfer due to these electron spectra and weight the dose delivered based on this lineal energy transfer quantity according to a quality factor determined by the ICRU [26]. This model incorporates the effects of dose-rate and is presented in more detail in Chapter 4 as a basis for our experimental determination of RBE for the various photons emitted by the ^{241}Am foils.

In order to design experiments to establish a more complete understanding of the dependence of RBE on photon energy, analysis of available data was first necessary. Here some of the literature data have been presented for the RBE of low-energy photons. Chapter 4 details the use of the ^{241}Am foils to gather data relevant to the study of energy and dose-rate effects.

1.5 Motivations for Developing ^{241}Am Foil Sources

The studies presented above have motivated our work with ^{241}Am. Although they do not fully explain the mechanisms of biological response to ionizing radiation, they do demonstrate several factors may influence the observed biological effect of photon radiation, including total dose accumulated, dose-rate, energy spectrum, assay type, and cell or animal being studied. The ^{241}Am irradiators were developed to deliver dose-rates and energy spectra to produce new biological results to further explain the mechanisms of biological response to ionizing radiation. In the following section, some existing sources which provided motivation for the development of the ^{241}Am foil sources are discussed.

1.5.1 Problems with Existing Radiation Sources

The studies above consider the effects of conventional radiation sources, keV and MeV x-rays, ^{60}Co gammas, ^{137}Cs gammas. These sources offer the advantage of being characterized and standardized by the National Institute of Technology (NIST) and other standards laboratories. Gathering dose/dose-rate for these sources is a simple process since dosimeters can be calibrated by exposing them to a known dose delivered by a standard source.

However, these sources also have limitations. For the study of biological effects of different photon energies, it would be ideal to study monoenergetic sources, but x-ray bremsstrahlung spectra are continuous, preventing analysis of the RBE of a single photon energy.

The gamma photons produced by ^{60}Co and ^{137}Cs are far removed from the low-energy range where non-linearity is suspected to occur for RBE. The ^{232}Th source discussed above produces photons of 63 keV but delivers a dose-rate of only 10 cGy/year. This limited dose-rate is due to the infrequent probability of the gamma-producing nuclear transition and the large half-life of ^{232}Th, 1.405×10^{10} years. Because of these factors and its density of 11.7 g/cm^3, self-attenuation within the source becomes problematic for generating higher dose-rates.

Beyond the problem of energy spectrum, conventional sources are often difficult to implement in a continuous radiation scheme. X-ray tubes produce photons only if they are powered and cooled continuously. A failure in the power supply or cooling system of an x-ray tube could ruin long term experiments if radiation was halted. Isotope sources used in low dose-rate studies to date also have limitations. The ^{60}Co and ^{137}Cs sources produce high-energy photons which are very penetrating, making it necessary to use large amounts of shielding to reduce dose-rates to the area surrounding the experiment to regulatory limits.

1.5.2 Physical Characteristics of the ^{241}Am Foils

Our design goals for the ^{241}Am foils were guided by the limitations of other conventional radiation sources. The irradiators were designed to meet several conditions. A consistent dose-rate over the period of an experiment was desired, so a half-life on the order of years was necessary in order to prevent reduction in dose-rate due to decay during an experiment. From a safety standpoint, the dose-rate to the surrounding area must be limited so that other biological samples or lab workers could be located nearby. To study the dose-rate effect over several orders of magnitude above the background radiation level, an unshielded dose-rate of 1-10 cGy/h was necessary. Experiments to investigate the RBE for low energy photons were of interest, so photons below 100 keV were necessary. For an animal irradiator, it was necessary to maintain a consistent dose to the full depth of the animal so photons could not be completely attenuated within the animal.

To meet these goals ^{241}Am in thin foils was chosen. The ^{241}Am foils are pictured in Figure 5, and a cross section is shown in Figure 6. Known mostly for its capacity as an alpha emitter, ^{241}Am also emits gamma photons at 26.34 keV and 59.54 keV as illustrated in the decay scheme in Figure 4. In addition to these photons, lower energy fluorescence photons in the 10-25 keV range are emitted. Shielding materials may be used to selectively remove photons from this spectrum. This use of different shielding materials allows for control of the energy spectrum, which is discussed in detail in Chapter 2.

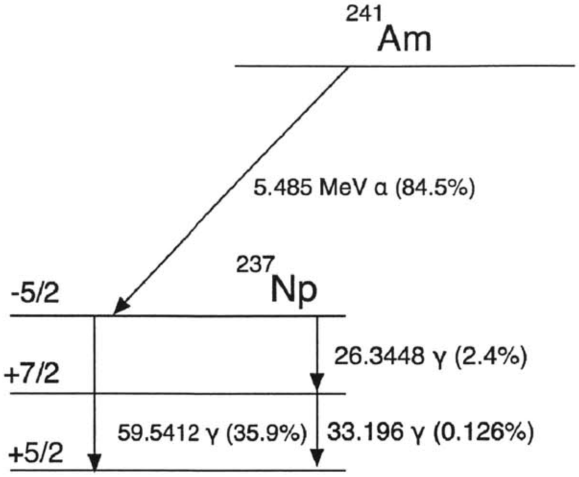

Figure 4. Decay scheme for ^{241}Am.

In this decay scheme, note the gamma photons at 59.5412 keV and 26.3448 keV. The ratio of the number of photons observed at these energies is important for the efficiency correction of the spectrometers used in Chapter 2.

Figure 5. ^{241}Am foils on a lab table.

In this figure note the gold-plating on the surface of the ^{241}Am foils.

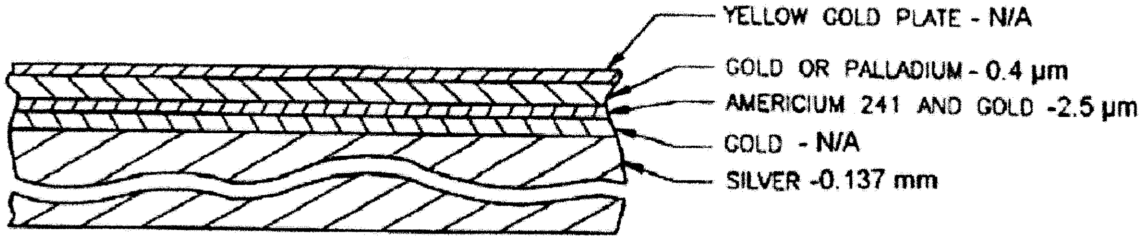

Figure 6. Cross section view of ^{241}Am foils.

In this cross-section note the presence of silver, gold, and palladium which produce fluorescence x-rays. These fluorescence x-rays are described in detail in Chapter 2.

These foil sources yield dose-rates of 2 cGy/h when unshielded and can be shielded to reduce the dose-rate without significant changes to the energy spectrum using methods described in Chapter 2. They can be placed directly under biological samples in a water-jacketed incubator without affecting the dose-rate in neighboring incubators since the photons emitted are attenuated effectively by the incubator walls. They can also be implemented in a long-term animal irradiator which limits the doses to animal care workers to levels acceptable for the general public by the NRC. This animal irradiator design is described in Chapter 5.

1.5.3 Potential for Generating New Low Dose-rate Data

These irradiators have potential to yield valuable new data in the study of low-dose rate radiation and relative biological effectiveness of low energy photons. Using the ability to control both dose-rate and energy spectrum, the effect of the 60 keV photons as well as lower energy fluorescence photons can be studied. Since no data exist for monoenergetic photon spectra in the 60 keV energy range for the dose-rates available, new experiments can be designed which may validate or contradict the models of RBE which describe an inflection in the 20-100 keV photon range.

With these benefits came several challenges. Since the energy spectra produced by these sources varies greatly with the amount and type of shielding material applied, it was necessary to develop a method of determining these spectra accurately. A method for determining the best estimate of these energy spectra is described below in Chapter 2. Since the dose-rate is an important factor in determining the biological effect of a radiation field, it was also necessary to develop a method of accurately determining dose-rates for the several energy spectra produced by these irradiators. Methods described in detail in Chapter 3 were employed for this purpose.

With the physical characterization of the foils complete, biological experiments were designed and performed to display the ability of these irradiators to provide new data on the effects of low dose-rate low photon energy radiation. These experiments are described in detail in Chapter 4.

The ^{241}Am foil sources were also used to design an animal irradiator capable of irradiating animals in four standard mice cages at dose-rates of 0.5 cGy/h. The design and analysis of these irradiators is presented in detail in Chapter 5.

Together these irradiators for cell culture and animal experiments will offer the opportunity to study low dose-rate ionizing photon fields which have never before been studied in radiobiology. These sources may yield valuable data concerning the risks of radiation exposure at low-dose rates and low-photon energies. These data will have direct applicability to all scenarios in which individuals are exposed to low-energy photon radiation.

By studying the effects of the fluorescence photons produced by these irradiators in the energy range 10-25 keV, it may be possible to determine the degree of irreparable damage caused by these photons. The biological effectiveness of these photons has direct applicability to the use of low energy photons in mammography and brachytherapy.

Since both of these applications employ low-energy photons which have been shown to have increased biological effectiveness relative to photons above 100 keV, it is important to understand the risks due to these low energy photons before assigning risks associated with these applications. These risk estimates are currently based on the MeV γ-ray spectra to which atomic bomb survivors were exposed, and it is likely that a better model for risk which incorporates the effects of dose-rate and photon energy could be generated. The ^{241}Am foils could be used to generate data which could contribute to a new model of risk of radiation exposure.

1.5.4 Validation of RBE Models

Using the methods presented in this thesis, it may also be possible to discover more about the dependence of RBE on photon energy for photons in the 20-100 keV range by comparing data generated with our sources to data generated using other photon sources. These observations may allow validation of the models proposed by Brenner et al. [25] and Kellerer [23] which would have important implications for both mammography and brachytherapy. If it is possible to demonstrate that RBE for 60 keV photons is greatly reduced over lower energy photons, it should motivate further investigation into the photon energies applied in these applications.

In this thesis a new model of energy deposition within a cell nucleus for low dose-rate ionizing radiation is proposed that provides a basis for estimating RBE for low dose-rate fields. Using this model and the methods described in this thesis, it may be possible to motivate a new evaluation of the way biological effects are projected for low dose-rate fields.

These studies and motivations have guided development of the ^{241}Am foil sources and methods presented in this thesis. With the development of any new technology, benefits are apparent, but challenges of implementation are also present. These challenges and their solutions are presented in the following chapters.

1.6 References

1. Report of the President's Commission on the Accident at Three Mile, President's Commission on the Accident at Three Mile Island, October 1979, Washington, DC.
2. C. Norman, Hazy Picture of Chernobyl Emerging, Science, 232, 4756, 1311-1449.
3. Boris Porfiriev, Disaster Policy and Emergency Management in Russia, Nova Science Publishers, Hauppage, NY, 1997.
4. Regulatory Dose Limits, Health Physics Society, http://hps.org/publicinformation/ate/faqs/regdoselimits.html, viewed April 5, 2010.
5. E. J. Hall, Radiobiology for the Radiologist, 4th Edition, 1994, J.B.

Lippincott, Philadelphia.

6. A H. W. Nias, "An Introduction to Radiobiology", John Wiley, New York, 1990.

7. J. S. Bedford and J. B. Mitchell, Radiation Research, 54, 316-327, 1973.

8. H. Mirzaie-Joniani, D. Eriksson, A. Sheikholvaezin, A. Johansson, P. Löfroth, L. Johansson, T. Stigbrand, Cancer, 94, S4, 2002, 1210-1214.

9. A. M. Ueno, I. Furuno-Fukushi, H. Matsudaira, Radiation Research, 91, 1982, 447-456

10. J. B. Mitchell, J. S. Bedford, S. M. Bailey, Radiation Research, 79, 1979, 520-536.

11. C. R. Mitchell, M. Folkard, M. C. Joiner, Radiation Research, 158, 2002, 311-318.

12. T. L. Deweese, J. M. Shipmana, L. E. Dillehay, and W. G. Nelson, Journal of Urology, 159, 2, 1998, 591-598.

13. N. J. Gragtmans, D. K. Myers, J. R. Johnson, A. R. Jones, L. D. Johnson, Radiation Research, 99, 3, 1984, 636-650.

14. O. Yamamoto, T. Seyama, H. Itoh, N. Fujimoto, International Journal of Radiation Biology, 73, 5, 1998, 535-541.

15. G. Liu, P. Gong, H. Zhao, Z. Wang, S. Gong, L Cai, Radiation Research, 165, 2006, 379-389.

16. E. Lorenz, C. Gorgdon, M. Deringer, J. Hollcraft, Journal of the National Cancer Institute

17. L. Lacoste-Collin, S. Jozan, V. Cances-Lauwers, B. Pipy, G. Gasset, C. Caratero, M. Courtade-Saidi, Radiation Research, 168, 6, 2007, 725-732.

18. S. Tanaka, I. B. Tanaka, S. Sasagawa, K. Ichinohe, T. Tatabatake, S. Matsushita, T. Matsumoto, H. Otsu, F. Sato, Radiation Research, 160, 2003, 376-379.

19. M. Bistrovic, M. Biscan, T. Viculin, Radiotherapy and Oncology, 7, 1986, 175-180.

20. A. Panteleeva, D. Slonina, K. Brankovic, K. Spekl, J. Pawelke, C. Hoinkis, W. Dorr, Radiation and Environmental Biophysics, 42, 2003, 95-100

21. M. Hoshi, S. Antoku, N. Nakamura, W. J. Russell, R. C. Miller, S. Sawada, M. Mizuno and S. Nishio, International Journal of Radiobiology, 54, 4, 1988, 577-591

22. M.A. Hill, Radiation Protection Dosimetry, 112, 4, 2004, 471-481.

23. A. M. Kellerer, Radiation Research, 158, 2002, 13-22

24. V. Michalik, D. Frankenberg, Radiation and Environmental Biophysics, 35, 1996, 163-169

25. D. J. Brenner, C. Leu, J. F. Beatty, R. E. Shefer, Physics in Medicine and Biology, 44, 1999, 323-333.
26. ICRU, "The quality factor in radiation protection", ICRU Report 40, Bethesda, MD.

Chapter 2: Spectral Analysis of ^{241}Am Foil Sources

2.1 Introduction

Biological response to radiation is influenced by the type and energy of the radiation involved [1]. Dosimeters available for measuring dose delivered by a photon field are also energy dependent for photons below 100 keV [2]. In order to measure the dose delivered by ^{241}Am photons and design biological experiments using ^{241}Am, it was necessary to develop the best estimate of the ^{241}Am photon spectrum.

Literature data are available for the ^{241}Am photon spectrum [4][5], however these data are for unshielded ^{241}Am and so do not include the effects of fluorescence and attenuation due to the layers of metal surrounding the ^{241}Am in the foil sources studied in this project. This difference prevents our use of these data for the purposes of dosimetry or biological effectiveness comparisons. Instead a method was developed for experimentally determining the photon spectrum of the ^{241}Am foils.

By combining spectral data from multiple detectors and literature sources, the best estimate of the photon spectrum emitted by ^{241}Am foils was established. This method is described in the sections below.

2.2 Overview of Detection and Spectrometry of Low Energy Ionizing Photon Radiation

Several methods exist for detecting ionizing photons of energy less than 100 keV. Each has a specific physical mechanism whereby radiation is converted into an electrical signal for readout. These methods and their underlying physical mechanisms are described below. Their applicability for use with low energy photon radiation fields is discussed.

Every method of radiation detection discussed here involves the detection of charge pairs, ions and free electrons, created by ionizing radiation. When a low energy photon interacts with an atomic electron, it may either impart all or part of its energy to the electron.

When all of the photon energy is absorbed by an atomic system, an electron is ejected from the atom, creating a positively charged ion and free electron. If the photon imparts a fraction of its energy to the electron, the electron may or may not be freed from the atom, depending on the amount of energy absorbed. In this process, known as Compton scattering, a photon of a lower energy results and may go on to create further scattering or ionization events.

Detectors are characterized by their efficiency and energy resolution. Energy resolution is the degree to which a detector is able to distinguish particles of differing energies and is defined based on the shape of a peak in the energy spectrum produced by a detector. For a peak in a pulse height spectrum, the full width at half-maximum in units of pulse height divided by the average pulse height is defined as the energy resolution.

Absolute efficiency is defined as the number of total ionization events recorded divided by the number of total particles emitted by a radiation source. Intrinsic efficiency is the number of total ionization events recorded divided by the number of particles entering a detector. In order to determine an energy spectrum for ^{241}Am, a measure of absolute uncertainty was unnecessary since only the relative numbers of photons of different energies were important. In the following text, the term efficiency has been used in place of intrinsic efficiency.

An ideal detector would detect all incoming photons with 100% efficiency and perfect energy resolution, but this has not been achieved. In order to gain a complete understanding of a low-energy photon radiation field, it was necessary to gather data on the energies and intensities of the field. The methods outlined below may be used to gather these data and gain the most complete understanding of the radiation field possible.

2.2.1 Scintillation Detectors

When ionizing photons interact with some materials, photons of lesser energy are released in a process called scintillation. Scintillation may occur with organic materials including organic crystals, organic compounds in solution, and polymerized organic compounds. Scintillation may also occur in inorganic crystalline compounds. The physical processes which lead to the emission of these photons vary with material.

In some organic materials, the electrons within individual molecules may be excited to unstable energy states. As these electrons transition back to their stable ground states, energy is released in the form of a photon.

Some organic compounds have been used as scintillators for the detection of x-rays and gamma photons below 100 keV. In particular, the plastic NE316 loaded with 10% tin has been used for detection in this energy range [2].

In inorganic crystalline compounds, the crystalline lattice structure determines the possible energy states of electrons within the crystal just as the molecular structure determines the possible energy states of electrons within a molecule. As ionizing radiation excites electrons within an inorganic solid, electrons may transition from the valence band of energy states to the conduction band of energy states. In some crystalline materials, transitions between activator states also occur. These activator states are lesser in energy than conduction band states and greater in energy than valence band states, and are due to irregularities in the crystalline structure. As an electron in an elevated energy state transitions to a lower energy state, energy is released in the form of a photon. Scintillation materials are chosen such that these scintillation photons are typically within the range for which photodetectors are most efficient (300-750 nm) [2].

These scintillation photons are counted using photodetectors (either photocathodes and photomultiplier tubes or diode photodetectors) and used to determine the amount of energy deposited in the crystal by incoming ionizing photons. As photons are counted over a period of exposure, the energy spectrum of the incoming photon field can be estimated.

Since the methods of counting photons are not 100% efficient (typically 20% efficient for photocathodes [2]), information about the amount of energy deposited in the scintillator is lost in the photon to electron conversion process. This information loss results in poor energy resolution relative to other detectors which do not rely on the conversion of ionizing photon to visible photon to electron [2]. This relatively poor efficiency is illustrated in Figure 1, in which an energy spectrum measured using a sodium iodide spectrometer is compared to an energy spectrum measured using a high purity germanium detector.

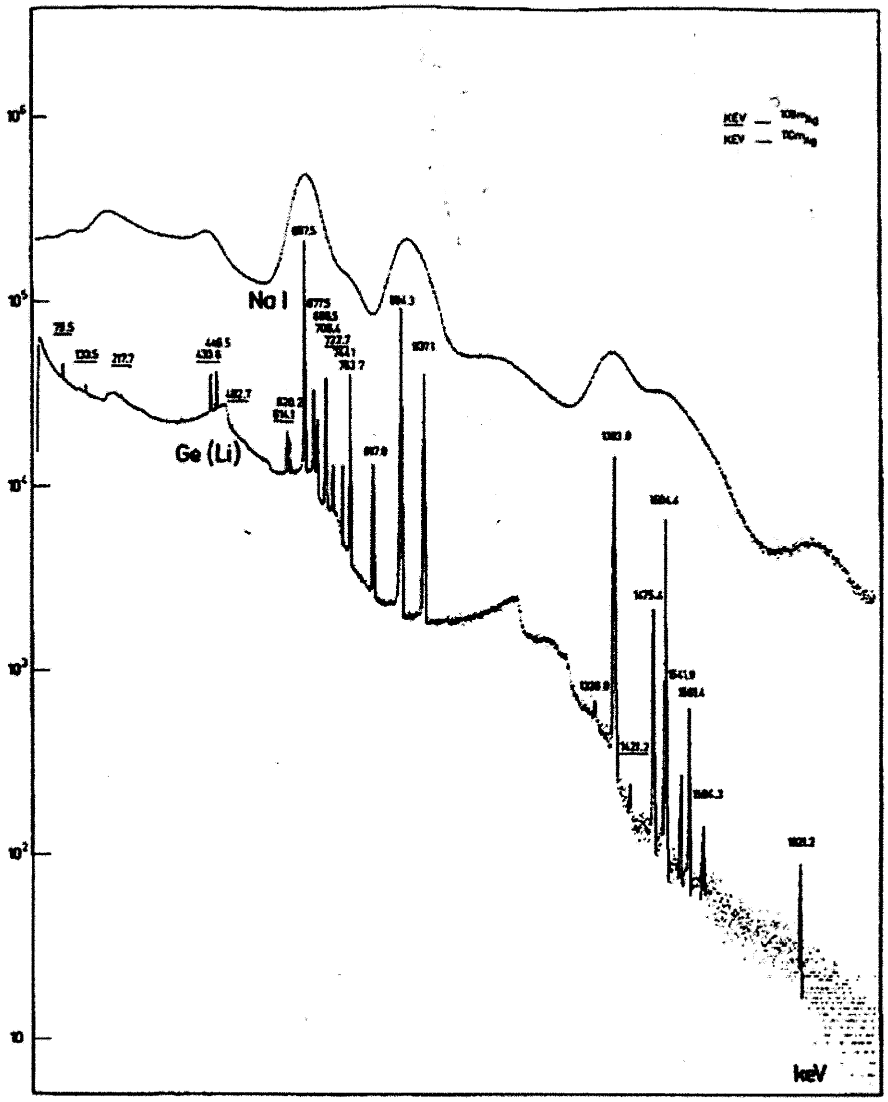

Figure 1. Same photon field measured by a sodium iodide scintillation detector (top curve), compared to a lithium drifted germanium detector (bottom curve) [2].

Since it was necessary to have sufficient energy resolution to resolve the individual photons of the ^{241}Am spectrum to develop the best estimate of photon spectrum emitted by the ^{241}Am foil sources, and other methods of spectroscopy provided better energy resolution, scintillation detectors were not used in this project.

2.2.2 Semiconductor Detectors

In a semiconductor detector, a radiation field creates electron/hole pairs within a semiconductor crystal lattice. A bias voltage applied to the crystal causes the electrons and holes to drift under the influence of the electric field inside the crystal. The current created by these drifting electrons and holes is detected. This current is proportional to the number of electron/hole pairs and is thus proportional to the energy of the incoming particle.

Some semiconductors have an energy level structure which enables their use for detecting ionizing radiation. Two bands of energy levels, the valence band and the conduction band, are separated by a band gap of approximately 1 eV (1.12 eV for silicon and 1.4 eV in the case of cadmium telluride). Because of this energy difference, an ionizing photon entering such a material needs only to impart 0.7 eV to an electron to create an ionization event. This gives semiconductors better energy resolution than scintillation detectors which need 20-30 eV to create an ion pair [2].

Several types of semiconductor detectors are available. For the purpose of spectroscopy of low-energy photons, the energy-dependent efficiency is an important factor. Germanium-based detectors have constant energy efficiency between 20 keV and 100 keV [8]. A germanium K-shell at 11.1 keV reduces efficiency of detection of photons between 11.1-20 keV as K-shell electrons ejected by photons of these energies escape the detector volume and their energy is not fully deposited in the crystal [8].

Silicon-based detectors offer good energy resolution (136 eV at 5.9 keV for the Amptek X123 described below) and have constant energy efficiency between 8-11 keV [11]. Outside of this range, energy efficiency is reduced due to attenuation effects at below 8 keV and low probability of interaction for the low Z silicon above 11 keV.

Cadmium telluride detectors have poorer energy resolution than silicon-based detectors but do offer constant energy resolution from 10-20 keV and 30-50 keV [11]. Cadmium florescence photons between 22-26 keV cause inaccuracy in this range [5]. This energy range is important for the spectroscopy of ^{241}Am with its 26.34 keV gamma photon.

There is no one detector with consistent efficiency for the entire ^{241}Am energy range (8-60 keV). The strategy outlined below is a method of using multiple detectors in combination with literature data to provide a better estimate of the spectrum than possible with a single detector.

2.3 Dectector Implementation

After considering the technologies available for spectroscopy of ^{241}Am low-energy photons described above, the ^{241}Am photon spectrum was measured with germanium and silicon-based detectors and these data were compared with literature sources. Through this comparison, a method was developed for collecting spectra experimentally and correcting these for energy efficiency, background, and fluorescence within the detector. This method is described in the following sections.

2.3.1 Literature Data

The Table of Radioactive Isotopes (7th Edition) provides a tabulated energy spectrum of ^{241}Am [5]. These data are reproduced in Table 1. Energy and frequency information are included for ^{241}Am gammas as well as ^{237}Np fluorescence x-rays which are also present in the energy spectrum. To obtain this data, Genous-Lubain et al. measured a 30 mCi unsealed source with a Ge(Li) detector [3].

Energy	Frequency	+/-
13.927	0.13	0.012
17.611	0.202	0.024
20.997	0.052	0.007
26.3445	0.024	0.001
59.5364	0.357	0

Table 1. Energies and frequencies of photons from the decay of ^{241}Am reported by the Table of Radioactive Isotopes.

Subsequently Bland et al. have presented an alternate version of this spectrum. In this study the photon spectrum emitted by ^{241}Am electroplated onto a stainless steel disk was measured with a Ge(Li) with efficiency characterized using several standards of known activity including ^{55}Fe, ^{57}Co, ^{65}Zn, ^{85}Sr, ^{88}Y, ^{109}Cd, ^{123}I, ^{133}Ba, ^{152}Eu, and ^{201}Tl [4]. These data are presented in Table 2.

Energy	Frequency	+/-
13.93	0.1301	0.001
17.51	0.1899	0.0015
21.01	0.04815	0.00038
26.345	0.02395	0.00019
59.536	0.357	0.0025

Table 2. Energies and frequencies of photons from the decay of ^{241}Am reported by Bland et al. [4].

While the data from these sources have some variation, they do have good agreement for the frequency ratios of the three highest frequency photons near 13.93 keV, 26.345 keV, and 59.5412 keV. These ratios are presented in below in Table 3.

2.3.2 Spectral Measurement of an Unsealed ^{241}Am Source

Along with the 59.54 keV gamma photon, the ^{241}Am foil sources emit a gamma photon at 26.345 keV as well as fluorescence x-rays from gold, silver, palladium, and neptunium since all of these metals are present in the ^{241}Am foils as described in Chapter 1. Due to these fluorescence photons and the attenuation of photons through the layers of metal surrounding the ^{241}Am in these foil sources, the energy spectra from these foils cannot be compared to literature data to determine detector efficiency.

Since 10-30 keV photons are attenuated more than 60 keV photons by the layers of metal surrounding the ^{241}Am, any attempt to correct the ^{241}Am foil spectrum using the literature data for unshielded ^{241}Am would result in an overestimation of the number of photons in the 10-30 keV energy range relative to 60 keV photons. Also, the presence of fluorescence photons in the 10-25 keV range could influence result in an underestimation of the number of photons in this range since these additional photons would not be present in the spectrum of unshielded ^{241}Am.

To avoid these problems, the photon energy spectrum of an unsealed ^{241}Am source with no metal covering was measured. This unsealed ^{241}Am source is shown in Figure 2.

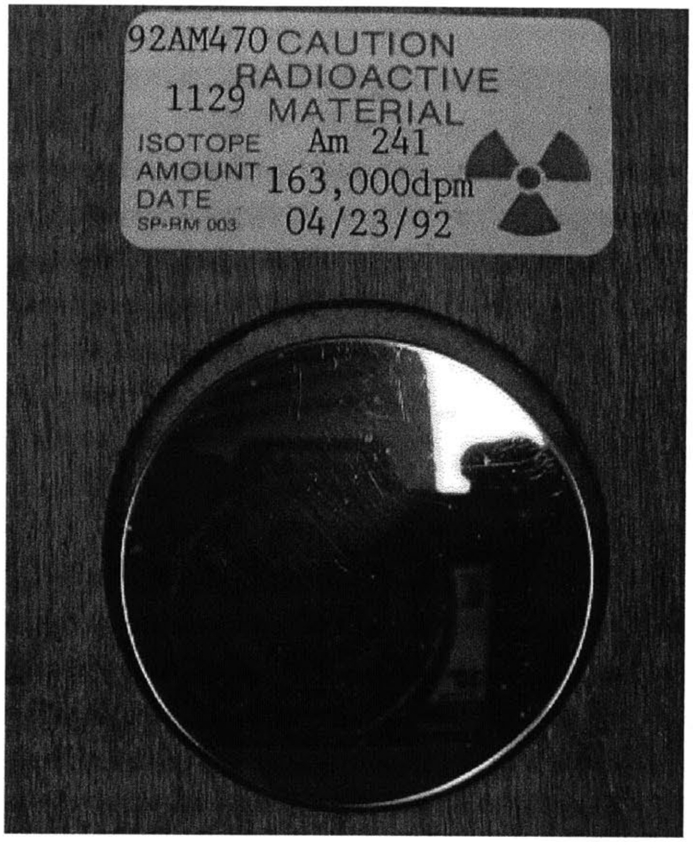

Figure 2. Unsealed ^{241}Am source. ^{241}Am electroplated onto a stainless steel disc.

2.3.2.1 Spectral Measurement of an Unsealed ^{241}Am Source with the Amptek X123 SiPIN Detector

Using the Amptek X123 spectrometer as shown in Figure 3, the energy spectrum of this source was measured. These data along with spectral data from the literature (as described in Section 2.3.1) and a high purity germanium spectrometer (as described in Section 2.3.2.2) were used to make the best estimate of the detector efficiency of the X123 spectrometer.

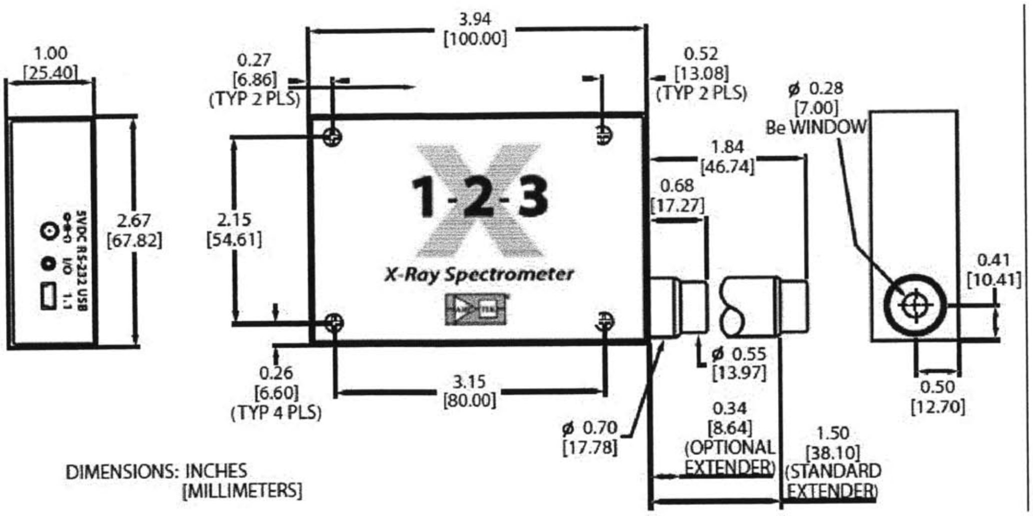

Figure 3. The Amptek X123 SiPIN spectrometer.

The X123 design is described by Redus et al. [5]. A silicon PIN diode is thermoelectrically cooled to 215 K. The silicon PIN diode is constructed from an i-type silicon crystal, which has no excess of positive or negative charge carriers. Dopants, which increase the level of excess charge carriers, are applied to both sides of this silicon crystal. On one side, a dopant which increases the number of positive charge carriers is applied. On the other side, a dopant which increases the number of negative charge carriers is applied. This creates a diode. When reverse-biased (i.e., a positive voltage is connected to the p-type doped side and a negative voltage is connected to the n-type doped side), no current flows through the crystal, unless it is exposed to a radiation field which produces charge pairs within.

When exposed to ionizing radiation, the charge pairs created within the diode move under the influence of the applied bias voltage, creating a pulse of current that is processed with a digital pulse processor. A photon energy spectrum measurement is the compilation of many of these processed pulses.

The X123 SiPIN spectrometer (#X1135, Amptek, Bedford, MA) was used to measure the photon spectrum of an unsealed ^{241}Am source. The standard source was a 9 cm^2 area of ^{241}Am electroplated onto a stainless steel surface (The Source, Inc., Albuquerque, NM). The activity of this source was 7.15 × 10^{-8} Ci.

The source was placed at 1 mm distance from the X123 aperture with a single sheet of paper between to prevent any alpha particle damage to the beryllium window of the detector. The acquisition time was 14 hours.

The X123 spectrometer yielded the photon spectrum provided in Figure 4. These data show 59.5412 keV peaks of lower intensity than the fluorescence peaks of lower energy, although this is not in agreement with the literature data discussed above in Section 2.3.1 .

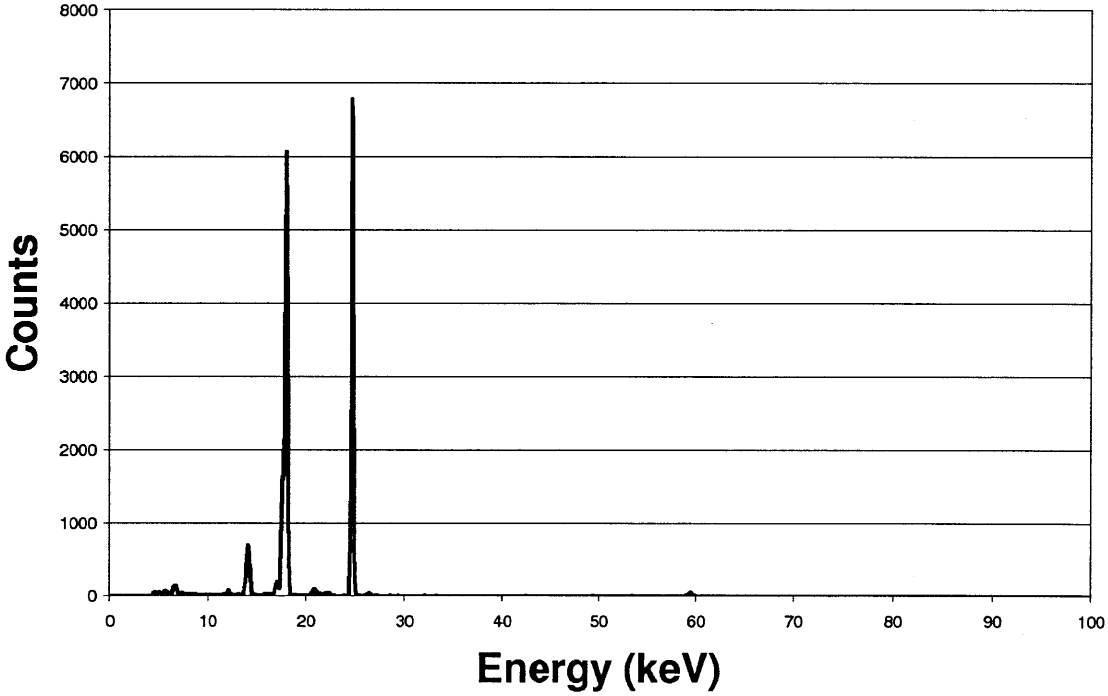

Figure 4. Electroplated ^{241}Am source spectrum from the X123 spectrometer measured over 14 hours. These data have not been modified for energy efficiency of the detector.

The spectrum measured using the X123 spectrometer and reported in Figure 4 is not corrected for the efficiency of the detector. Amptek publishes a theoretical estimate of the efficiency function for this silicon-based detector, although they state that it is only a theoretical estimate based on the x-ray attenuation coefficients for silicon available from the National Institute of Standards and Technology (NIST) [9]. This efficiency function is described by

Equation 1 in which, $\varepsilon(E)$ represents the theoretical efficiency of the detector, $\mu_{\mathrm{window}}(E)$ represents the mass attenuation coefficient for the beryllium window, $\lambda_{\mathrm{window}}$ represents the thickness of the beryllium windows, $\mu_{\mathrm{DL}}(E)$ represents the mass attenuation coefficient of the dead layer of the detector, $\lambda_{\mathrm{window}}$ represents the thickness of the dead layer, $\mu_{\mathrm{DET}}(E)$ represents the mass attenuation coefficient of the detector, and $\lambda_{\mathrm{window}}$ represents the thickness of the detector.

$$\varepsilon(E) = e^{\mu_{window}(E)\lambda_{window}+\mu_{DL}(E)\lambda_{DL}}(1-e^{-\mu_{DET}(E)\lambda_{DET}(E)}) \qquad (1)$$

Effects of scatter within the collimator of the detector, escape of secondary particles from the active detector volume, and variation (1-2%) in the size of the detector volume are not accounted for in this estimate [11].

Since Amptek cannot confirm that this efficiency function accurately describes their silicon detectors, this efficiency correction alone could not provide an accurate representation of the ^{241}Am spectrum. For this reason, the efficiency function was corrected based on comparison with literature data and spectral data measured with a high purity germanium detector as described below. This efficiency correction is described in the Section 2.3.3.2.

2.3.2.2 Spectral Measurement of ^{241}Am Standard Source with Canberra Reverse Electrode High Purity Germanium Spectrometer

The photon energy spectrum of an unsealed ^{241}Am source (described in Section 2.3.2.1) was measured using the Canberra GR3020 spectrometer (12016163, Canberra Industries, Meriden, CT).

This reverse-electrode germanium detector has dopants added to the regions described in Figure 5. This detector is reverse biased as described above. When ionizing radiation enters the crystal, the charge pairs created within the crystal cause a current to flow under the influence of the bias voltage. These pulses of current are amplified by a preamplifier circuit and processed by the DSA1000 amplifier/multi-channel analyzer (12029472, Canberra, Meriden, CT) to produce a photon energy spectrum.

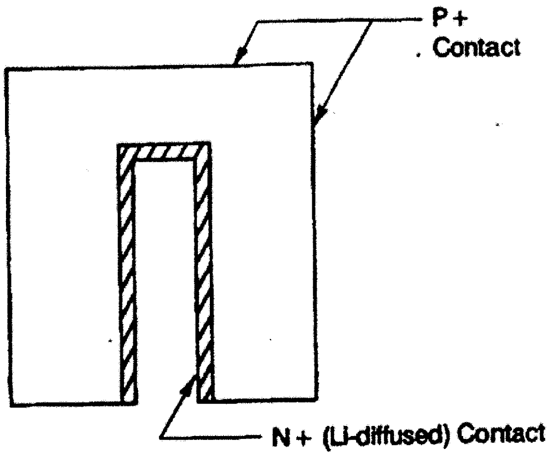

Figure 5. Reverse-electrode germanium crystal configuration.

The source was placed at 1 mm distance from the X123 aperture with a single sheet of paper between to prevent any alpha particle damage to the beryllium window. The acquisition times was 24 hours. The spectrum shown in Figure 6 was measured using the GR3020 spectrometer.

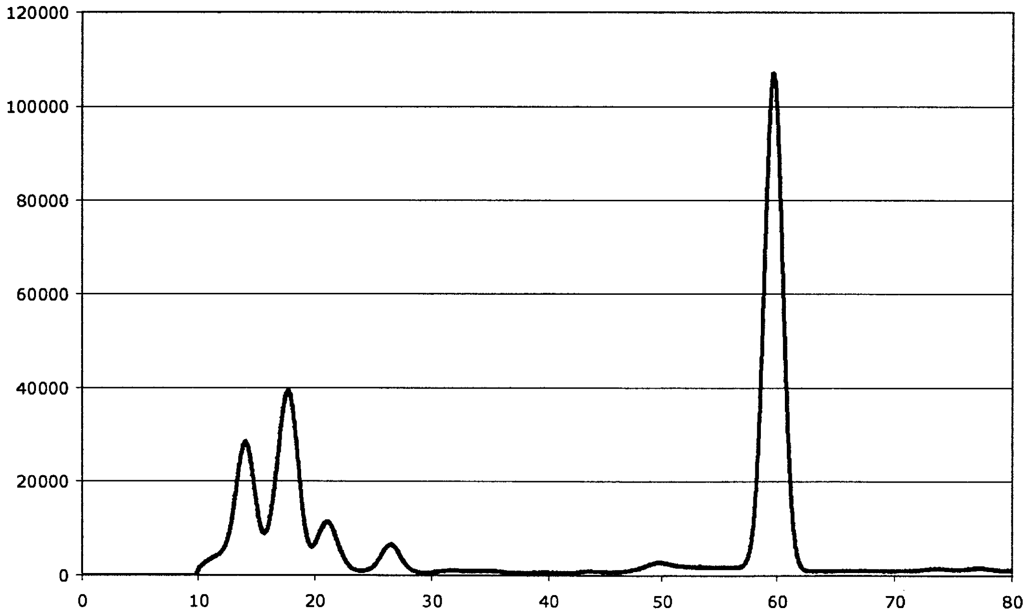

Figure 6. Spectrum obtained from the GR3020 high-purity germanium detector.

The spectrum measured using the GR3020 spectrometer and reported in Figure 2 is not corrected for the efficiency of the detector. Canberra publishes a theoretical efficiency function for this detector with a constant efficiency in the energy range 20-60 keV. This efficiency function is plotted in Figure 7.

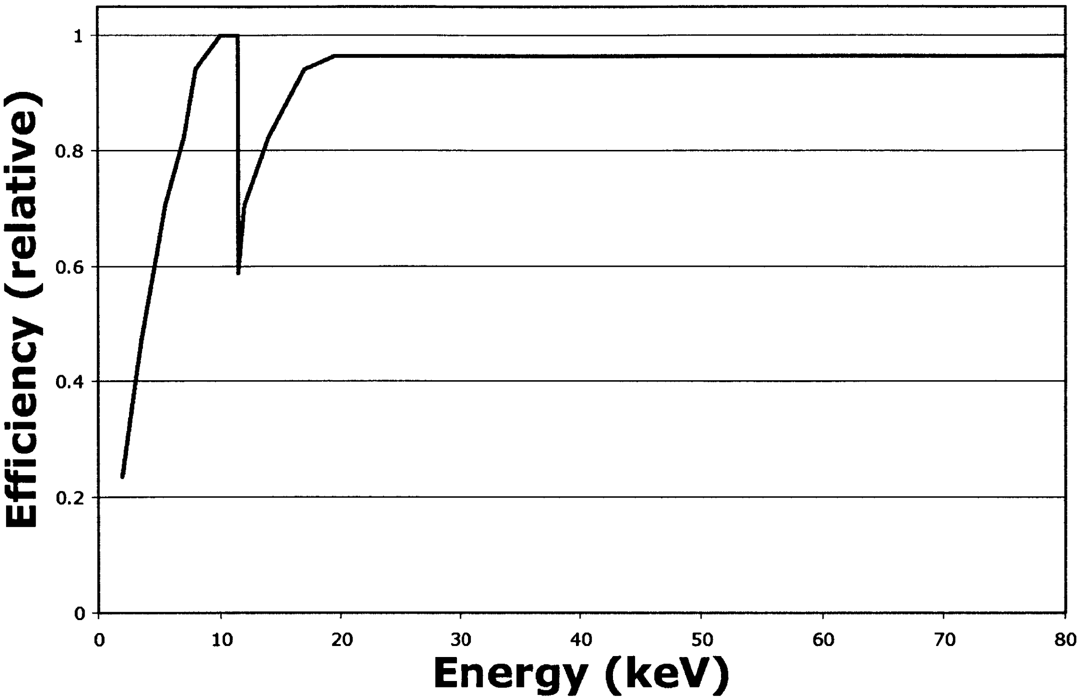

Figure 7. Relative energy efficiency of the GR3020 detector. Between the two gamma peaks at 26.39 keV and 59.54 keV, the efficiency is constant.

An efficiency-corrected spectrum was generated from these data and the efficiency function provided by Canberra [8]. This efficiency corrected spectrum is reported in Figure 8.

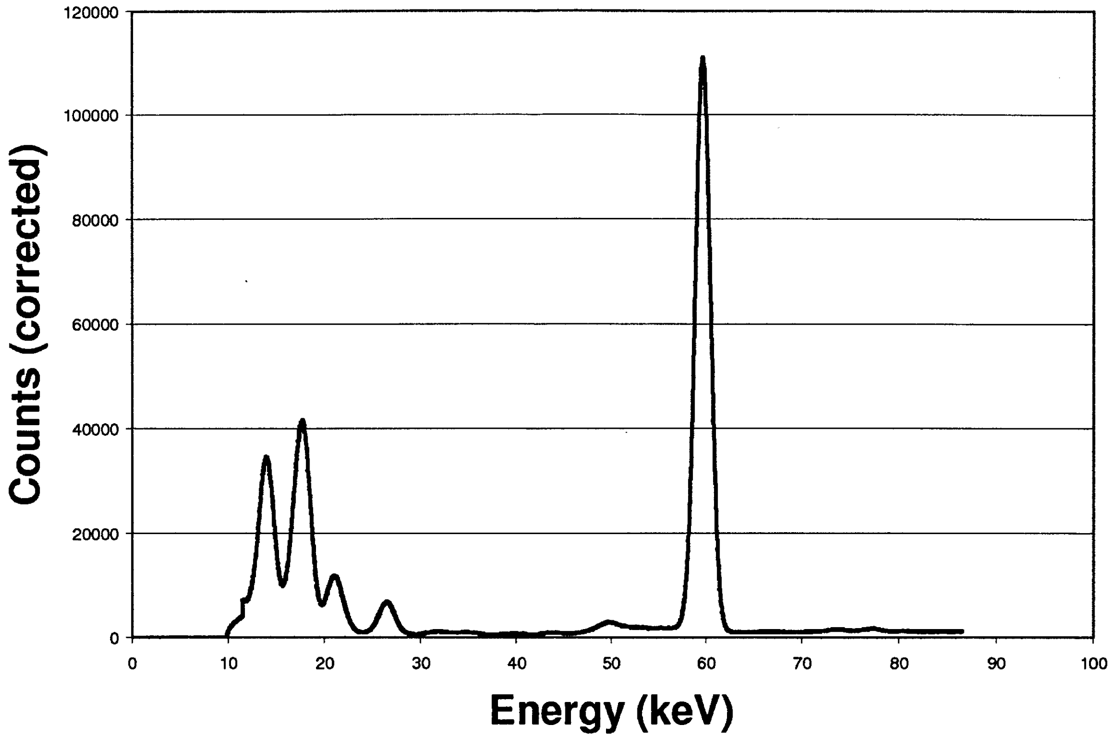

Figure 8. An efficiency-corrected version of the ^{241}Am spectrum gathered with the GR3020 spectrometer.

2.3.3 Comparison and Corrections

The Amptek X123 SiPIN spectrum provides the best energy resolution of the spectrometers considered above. Since this resolution is essential for distinguishing the low-energy photons of ^{241}Am, this spectrometer was used as the basis of the spectral measurement method for the ^{241}Am foil sources.

The manufacturer-provided estimate of the efficiency function of this spectrometer has been applied to the ^{241}Am spectrum measured above. When compared to the literature values for the spectrum and the spectral data gathered using the germanium detector, several important differences are seen. These differences are explained and corrected by the method described below. With these corrections based on multiple data sources, a method was established for measuring the photon spectra emitted by shielded ^{241}Am with greater accuracy than possible with any single source of data.

2.3.3.1 Background Subtraction

When operated at the settings used to gather the spectra from the unsealed ^{241}Am source described above for several hours, the X123 spectrometer shows two background peaks as shown in Figure 9. These peaks were observed with the same count-rate with 1 mm lead shielding the entire detector. For this reason it was determined that their origin is internal to the detector, either due to impurities in the metals within or due to electronic noise. A search of the Table of Isotopes [5] found no single impurity which would result in the photons of 18.1 keV and 25.0 keV. Also no source of photons at 18.1 keV or 25 keV could be identified which did not also produce other photons of similar intensity. Since these other photons are not present in this background spectrum, it is most likely that the origin of these peaks is electronic in nature.

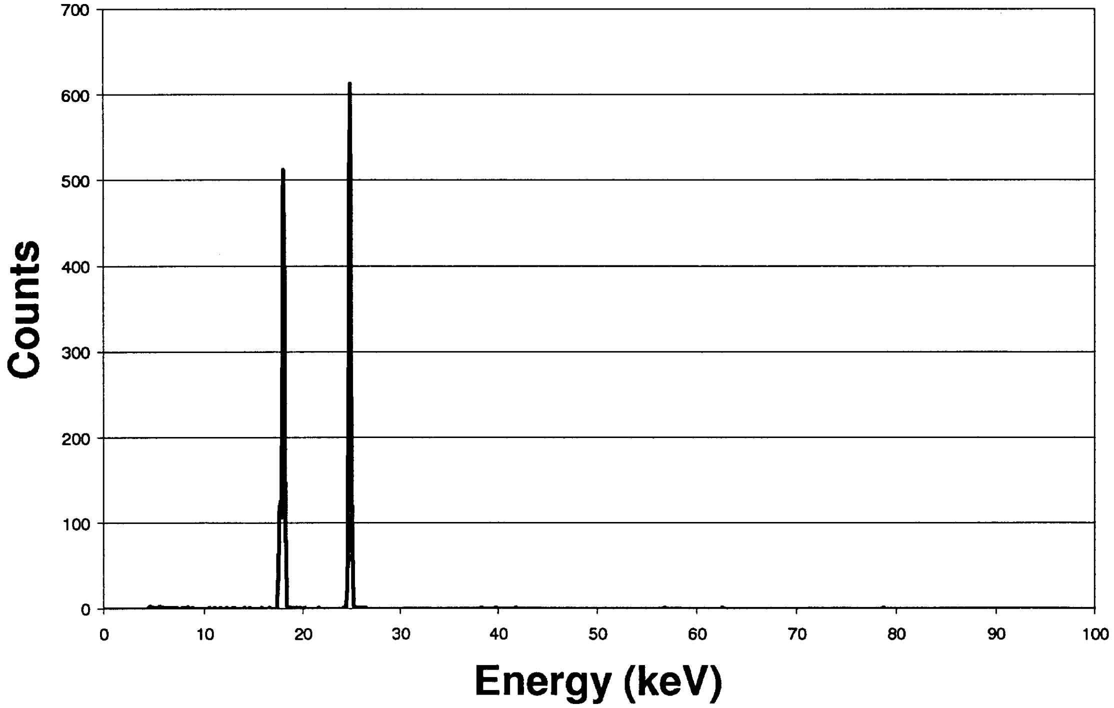

Figure 9. Background spectrum obtained from the X123 detector with an exposure time of 74 minutes.

This background must be subtracted from any spectrum observed over a period of several hours. In order to subtract the background, the following method was used. First, the area under each peak shown in the background spectrum is divided by the acquisition time to yield the background count rate per peak.

This background count rate for each peak is then multiplied by the time of acquisition for a spectrum measured with the Amptek X123 spectrometer. This yields the background counts for this spectrum.

This background count number is then subtracted from the number of counts in the ^{241}Am spectrum to yield the corrected counts in this each region with background counts. This corrected number of counts was divided by the total number of counts in the ^{241}Am spectrum in the region of interest. This factor was multiplied by the counts recorded at 17 ± 0.1 keV and 21 ± 0.1 keV energy ranges to yield a background-corrected spectrum for ^{241}Am.

This background-corrected spectrum is presented below in Figure 10.

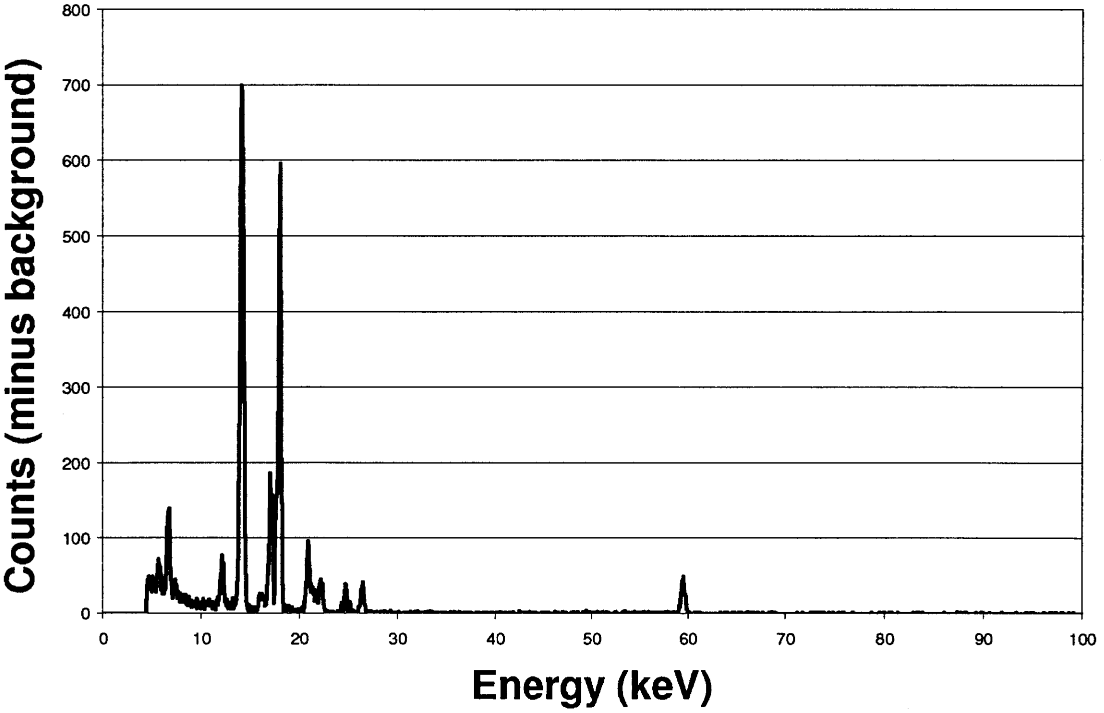

Figure 10. ^{241}Am spectrum with X123 background peaks removed.

2.3.3.2 Amptek Efficiency Function Modification

With the background subtraction applied to the ^{241}Am spectrum and the Amptek-provided estimate of the efficiency function applied, a corrected spectrum is produced which matches the published values for the relative intensities within 13% as shown in Table 3.

	13.93 keV	+/-	26.34 keV	+/-
SiPIN Corrected	0.35	4.66E-03	0.060	1.70E-03
HPGe Corrected	0.36	1.52E-04	0.066	5.77E-05
Bland et al.	0.36	3.74E-03	0.066	7.01E-04

Table 3. Number of 13.93 keV and 26.34 keV photons relative to the number of 59.5412 keV photons for literature and experimental spectra.

In the corrected Amptek spectrum, the ratio of the number of 26.34 keV photons to the number of 59.5412 keV photons is 0.060 ± 0.0017, compared to the literature value of 0.066 ± 0.0007 [4] and 0.066 ± 0.00005 as measured with the germanium detector described above.

In order to adapt the Amptek spectrum to match these values more closely, the Amptek-provided estimate of the efficiency function was adjusted to insure that these ratios match the values from the literature and the high purity germanium detector.

This was done by multiplying the efficiency correction function by another function, which brought the ratios in line with literature data. The Amptek-provided correction function is shown with the modified function in Figure 11.

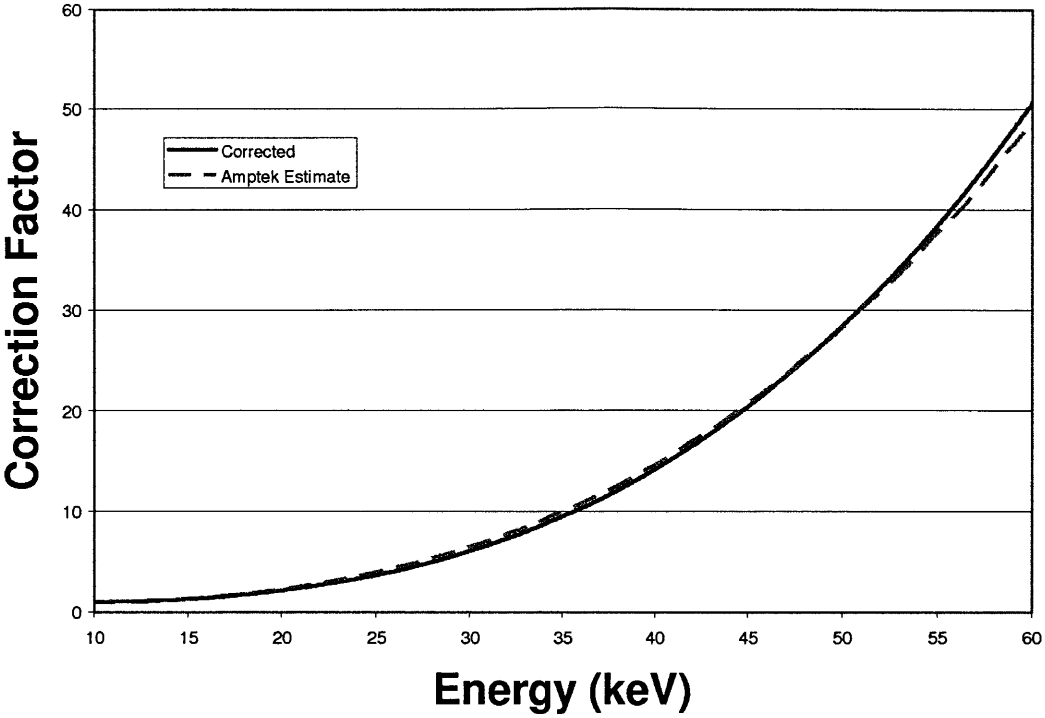

Figure 11. Amptek-provided estimate of efficiency correction factors along with function modified to fit other data sources.

2.3.3.3 Correction for Collimator Fluorescence

Fluorescence in the collimator of Amptek SiPIN detectors has been observed by Ferretti [7]. Ferretti observed photons at 22 ± 0.2 keV and 25 ± 0.2 keV in x-ray fluorescence spectra for compounds which did not contain silver. The conclusion of that study was that fluorescence from silver within the detector was responsible for these photons. Silver fluorescence photons have been measured at 21.99 keV, 22.163 keV, 24.912 keV, and 24.943 keV according to the Table of Isotopes [5].

Silver fluorescence photons of energies 22 ± 0.2 keV and 25 ± 0.2 keV were also observed with the SiPIN detector used in this project. To determine whether these lines were originating from the ^{241}Am source, an experiment was designed to filter these fluorescence photons.

A foil ^{241}Am source with activity 68 mCi was shielded with 3 cm Al and the photon spectrum of this configuration was measured with the X123 spectrometer. Using the mass attenuation tables provided by NIST [9], the filtration ratio between 22 keV and 59.5412 keV for 3 cm of Al was determined to be 3.14×10^9, excluding consideration of buildup. The filtration ratio between the 25 keV peak and the 59.5412 keV peak was found to be 1.15×10^7. From these data, there should be no observable 22 keV or 25 keV photons in the spectrum if these photons were originating from the source.

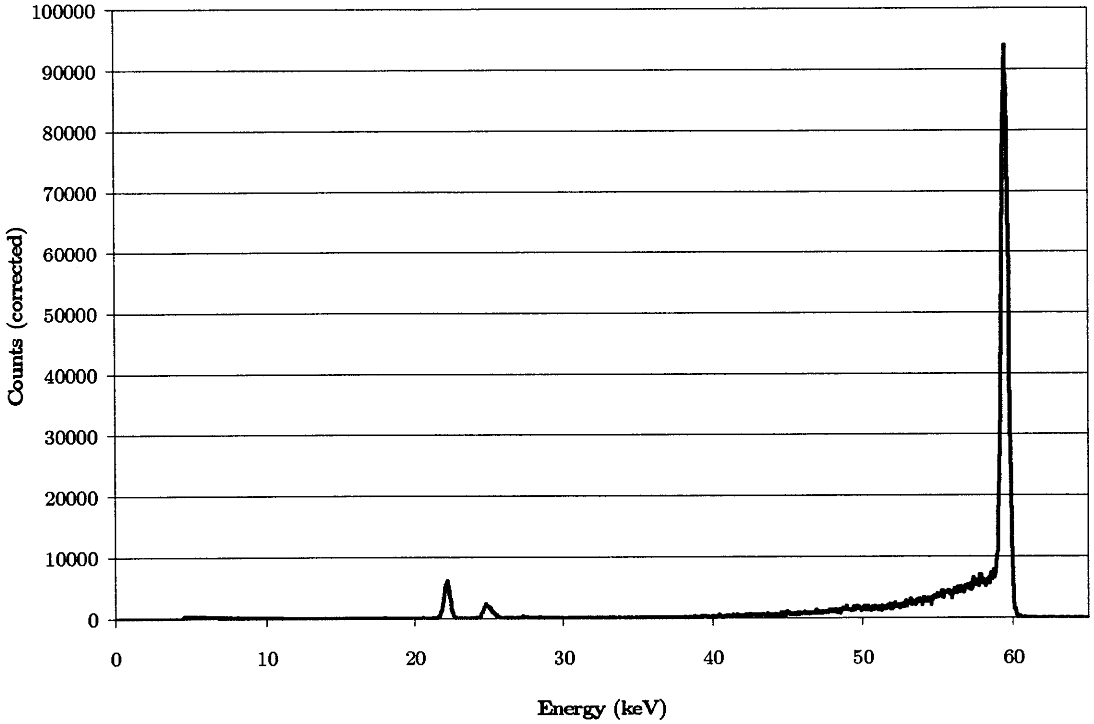

Figure 12. Spectrum observed through 3 cm of Aluminum shielding.

Upon examination of the spectrum shown in Figure 12, photons were counted near 22 and 25 keV. This experiment showed that these photons do not originate within the ^{241}Am sources but instead originate within the detector. The ratios of the number to the counts between 50-60 keV were calculated to determine the number of fluorescence photons produced in the collimator per original incoming photon.

Every spectrum observed with the Amptek spectrometer was then corrected to remove these peaks from the respective energy ranges in a scheme similar to that employed to remove background counts described above.

The ratios of counts in the 22 ± 0.2 keV and 25 ± 0.2 keV regions to the counts in the 50-60 keV region were calculated for the 3 cm shielded source and found to be 0.0328 and 0.0187 respectively. To correct a spectrum, the number of counts in the 50-60 keV region was mulitiplied by 0.0328 to yield the expected number of fluorescence counts in the 22 keV ± 0.2 keV region. This number of counts was subtracted from the number of counts found in the 22 ± 0.2 keV region to yield the fluorescence-corrected counts. This fluorescence-corrected counts figure is divided by the total number of counts in the 22 ± 0.2 keV region to yield the fluorescence correction factor for this region. This fluorescence correction factor was multiplied by the total number of counts in each energy bin across the 22 ± 0.2 keV region to yield a fluorescence-adjusted spectrum. The procedure was repeated for the 25 keV fluorescence peak.

2.3.4 Gold Side of a ^{241}Am Foil Source

When all of these corrections are applied to the spectrum measured from the gold side of a ^{241}Am foil, the result is the spectrum shown in Figure 13. In this figure, the individual peaks have been labeled with their origins as found in the Table of Isotopes [5]. Note the presence of gold, silver, palladium, and neptunium fluorescence x-rays.

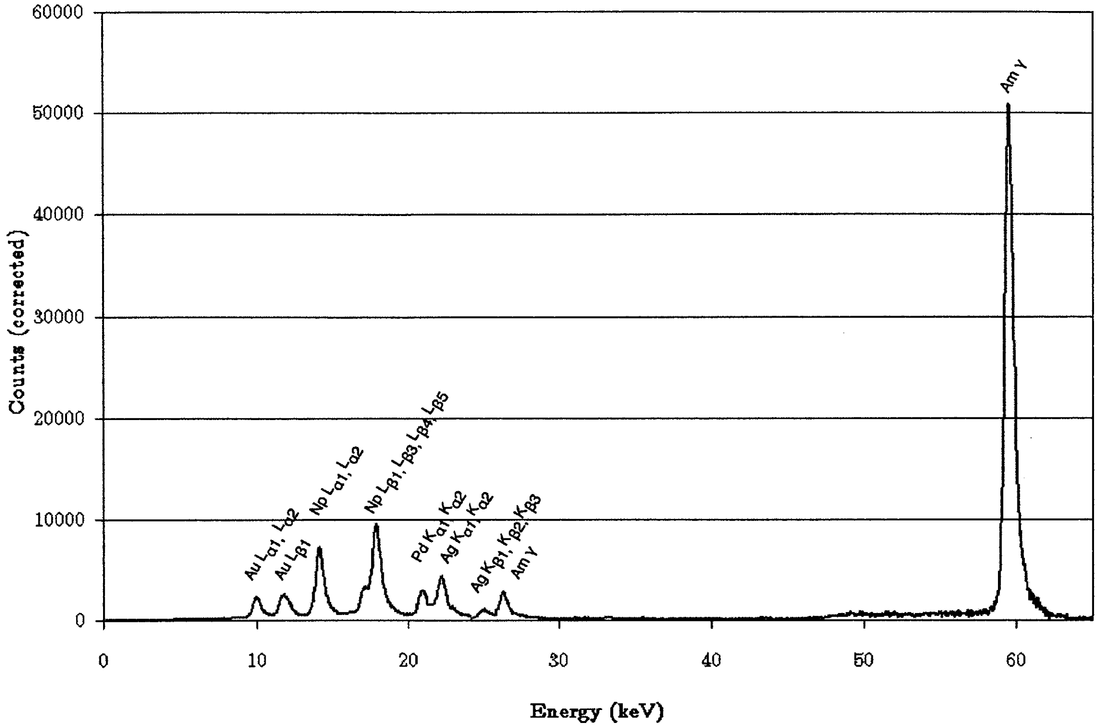

Figure 13. Spectrum emitted through the gold shielding side of the foil source.

2.4 Measuring ^{241}Am Spectra for Various Shielding Configurations

A method has been established above for acquiring a high-resolution energy spectrum across the range of interest for ^{241}Am and correcting this spectrum for background, energy efficiency, and fluorescence effects using data obtained from literature and other detectors to provide the best estimate of the true ^{241}Am spectrum.

With this method of acquiring the ^{241}Am spectrum established, energy spectra have been measured for ^{241}Am foil sources with several shielding configurations of interest for investigation in biological studies which are described in Chapter 4. These energy spectra are described below.

2.4.1 ^{241}Am Foil Shielded with 0.5 cm Aluminum

With 0.5 cm of Al shielding a foil source, the fluorescence x-rays are reduced to background levels and essentially all photons present are from the 59.5412 keV gamma line. This spectrum is of particular interest for investigation of differing biological effects for the 59.5412 keV photons and the lower energy fluorescence photons as described in Chapter 4. This spectrum is shown below in Figure 14.

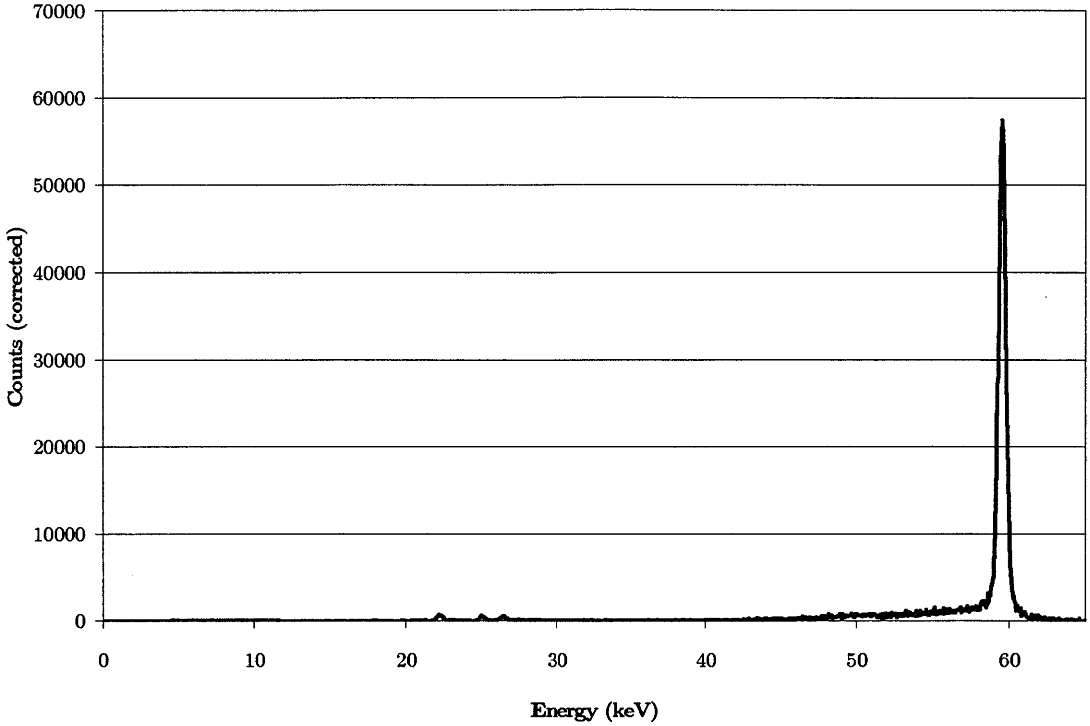

Figure 14. Spectrum of ^{241}Am shielded by 0.5 cm aluminum.

Comparing this spectrum with the spectrum emitted from an unshielded foil (Figure 13), it is evident that the majority of photons in the 10-30 keV range have been removed. More analysis of this spectrum is presented in Chapter 4 discussing relative biological effectiveness.

2.4.2 ^{241}Am Foil Shielded with 29mm Polyethylene

Composed of only carbon and hydrogen, polyethylene has a more constant mass attenuation across the 10-60 keV range than higher Z materials since the photoelectric cross-section varies with Z^4 for this energy range [6]. Because of this effect, lower energy photons are filtered less selectively, allowing for the reduction of total number of photons in the field without greatly changing the energy spectrum. Shown below is a spectrum collected with 29 mm polyethylene shielding applied to a ^{241}Am foil source.

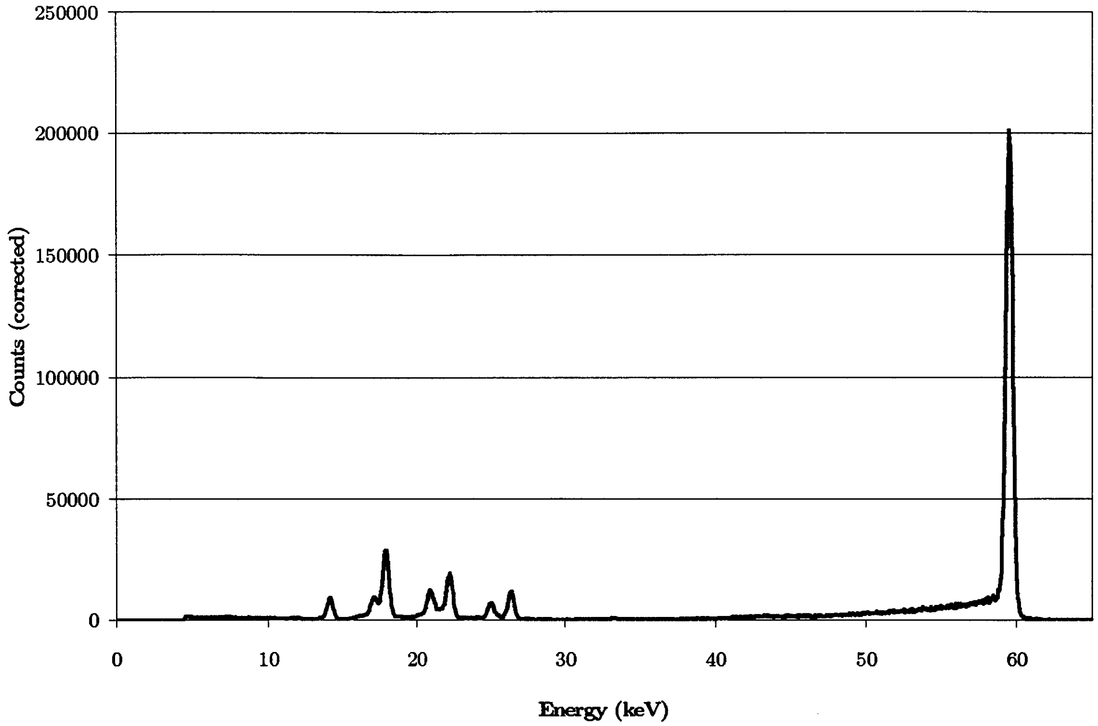

Figure 15. Spectrum of ^{241}Am shielded by 29 mm polyethylene.

Comparing the unshielded foil source spectrum (Figure 13) with this spectrum, it is evident that the fluorescence photons remain through 29 mm of polyethylene. The biological significance of these fluorescence photons will be described in Chapter 4.

2.5 Conclusion

Using two detectors along with literature data, a method has been established for correcting photon energy spectra measured with the X123 spectrometer for energy efficiency, fluorescence, and background. This method has been used to determine the best estimate of the photon energy spectra emitted by the ^{241}Am foils with and without shielding. These energy spectra will be used for dosimetry in Chapter 3 and in the study of the relative biological effectiveness of 10-60 keV photons in Chapter 4.

2.6 References

1. M.A. Hill, Radiation Protection Dosimetry, 112, 2004 471-481.
2. G. Knoll, Radiation Detection and Measurement, (Wiley, New York, 1989).
3. A. Genoux-Lubain, G. Ardisson, Radiochemical and Radioanalytical Letters, 33, 1978, 59.
4. C.J. Bland, J. Morel, E. Techeverry, M.C. Lepy, Nuclear Instruments and Methods A, 312, 1992, 323-333.
5. E. Browne and R.B. Firestone, Table of Radioactive Isotopes, ed. V.S. Shirley (Wiley, New York, 1986).
6. R. Redus, A. Huber, J. Pantazis, T. Pantazis, and D. Sperry, 2006 IEEE Nuclear Science Symposium Record, R15-4.
7. G. Lutz, “Semiconductor Radiation Detectors”, Springer, Berlin, 1999.
8. Canberra Germanium Detectors Users Manual, Canberra Inc., Meriden, CT, 1991.
9. J.H. Hubbell and S.M. Seltzer, Tables of X-Ray Mass Attenuation Coefficients and Mass Energy-Absorption Coefficients, NISTIR 5632, National Institute of Standards and Technology.
10. M. Ferretti, Nuclear Instruments and Methods B226 (2004) 453-460.
11. Detector Efficiency FAQ, Amptek Inc. http://www.amptek.com/.

Chapter 3: Low Energy Photon (10-60 keV) Dosimetry Methods

3.1 Introduction

Dosimetry is the measurement of energy deposited by ionizing radiation per unit mass. Several dosimetry methods have been developed in the history of radiation measurement. These range from fundamental absolute measurements of temperature changes (calorimetry) to other more complex measurements of charge accumulation (ionization chambers), chemical synthesis (chemical dosimetry), or phosphorescence (thermoluminescence) from which a dose measurement can be derived.

Each method has properties that make it more appropriate for certain applications. The physical processes utilized determine the accuracy and precision of the measurements. Accuracy and precision along with size and difficulty of setup help determine the applicability of the method for the dosimetry of low-energy photons.

In the sections below, each method is described in terms of these factors and present dosimetry data collected with multiple methods of dosimetry for several photon fields. Using these data, a method was established for dosimetry of the ^{241}Am foil sources with various shielding configurations.

3.2.1 Calorimetry

Calorimetry methods use the measurement of a change in temperature to determine the amount of energy deposited by a radiation field. Any energy deposited into a medium will manifest the in the form of thermal energy of the particles of the medium. Changes in thermal energy can be observed by measuring the temperature of the medium.

If a temperature change induced by radiation can be accurately measured, an absolute measurement of the dose absorbed can be obtained. The dose, D, can be obtained directly from the specific heat capacity of the medium, c, the mass of the medium, m, and the change in temperature, ΔT, as described by Equation 1.

$$D = c\,m\,\Delta T \quad (\mathrm{J/kg}) \tag{1}$$

Calorimetry has been used to measure high flux x-ray fields for which the total dose is several gray and heating is sufficient for measurement with adequate precision. For low dose-rate sources such as our ^{241}Am foils, this method is not possible using the same experimental setup since the heat imparted to a medium by a ^{241}Am foil is far less than that imparted by a typical x-ray tube with a dose-rate on the order of 1 Gy/min. Instead a more sophisticated microcalorimeter dosimeter has been applied for low dose-rate isotope sources.

Colle and Zimmerman [1] have developed a microcalorimeter capable of measuring the dose-rate of contained isotope sources based on measurement with Peltier devices. As heat imparted to the Peltier device is withdrawn into a surrounding isothermal heat sink, the devices produce an electric current that is measured.

This device has been used to gather dosimetry data from several custom-made isotope standard sources at the National Institute of Standards and Technology (NIST). While this device has been used for the dosimetry of photons as low in energy as 5.9 keV [2], it has limited applicability for sources other than those made for the specific geometry of the calorimeter. The ^{241}Am foils would not fit into the calorimeter chamber at NIST [2], preventing the use of this measurement method without a considerable effort to develop another microcalorimeter design. For these reasons, this method of dosimetry was not pursued with ^{241}Am foil sources.

3.2.2 Chemical and Photographic Dosimetry

Several methods of dosimetry using chemical processes have been developed. These include the Fricke dosimeter, photographic film, and radiochromic film. All of these methods rely on a chemical change caused by ionizing radiation to produce a measurable result. These methods are outlined in the sections below.

3.2.2.1 The Fricke Dosimeter

As ionizing radiation passes through matter, atoms are ionized. These ions and electrons may combine with other molecules or ions in the interaction medium to create new chemical species. The presence of these chemical species may be detected by several methods. A selection of these methods is described here along with their potential for measurement of low-energy photons.

The Fricke dosimeter is the most well known chemical dosimeter. Originally developed by Fricke and Hart [3], the Fricke dosimeter method relies on the oxidation of Fe^{2+} ions to Fe^{3+} in a solution of ferrous sulfate. The presence of these Fe^{3+} ions is detected using a spectrophotometer. This method is valid from 4-400Gy. The average dose absorbed, $\overline{D}$, in the Fricke solution is given by Equation 2 in which M is the change in molar concentration of the product (Fe^{3+}) due to irradiation, ρ is the solution density, and $G(Fe^{3+})$ is a function that describes the production of Fe^{3+} per unit energy delivered to the solution.

$$\overline{D} = \frac{M}{\rho G(Fe^{3+})} \tag{2}$$

Several other methods of chemical dosimetry employ other chemical species that provide different applicable dose ranges [3]. While some of these methods have the ability to measure dose as small as 2 cGy, all of these methods report the average dose delivered to an aqueous solution. Since low-energy photons are readily attenuated by an aqueous solution, the depth of the dosimeter solution is an important concern when attempting to measure the dose delivered to a monolayer of cells in culture. For the purpose of measuring the dose to a monolayer of cells, it is ideal to measure the dose to a thin layer of aqueous solution.

In order to measure dose using the Fricke method, a volume of approximately 10 mL of solution must be exposed in order to perform spectrophotometry. In order to expose 10 mL of solution in layers as thin as a cell monolayer (~10 um), it would be necessary to expose a large surface area of solution (10000 cm^2). This along with the experimental difficulty of maintaining uniform thickness of the solution prevented use of this method for dosimetry of the ^{241}Am foils.

3.2.2.2 Photographic Dosimetry

Just as a photographic film can be used to measure exposure to optical light, it may also function as a dosimeter for ionizing radiation. Silver bromide particles embedded in gelatin and spread in a thin film across a plastic base can indicate exposure to radiation by a change in optical absorption at the site of radiation impact.

The optical absorption of the film is not linear with radiation exposure over a large dose range [4]. This effect is due to the effect of saturation, since once a unit of silver bromide has been exposed, subsequent energy absorption by this unit do not produce additional changes in optical absorption.

Even if the optical absorption is linear with exposure over a certain range which varies with film, the optical absorption is not necessarily linear with dose. This nonlinearity is the result of the scattering of secondary electrons between the regions of gelatin, silver bromide, and plastic in the dosimeter. The energy of the incoming photons will determine the range of the secondary electrons generated and thus determine their range within the film. It is impossible to know if an exposure is generated from a secondary electron emanating from a gelatin molecule or from a silver bromide molecule.

In practice it is difficult to derive a dose measurement for low-energy photons with this method because of this complication along with the difference in atomic number between tissue, silver and bromine. Higher atomic number atoms (Ag=47, Br=35) have greater interaction probabilities with low energy photons than lower atomic number atoms in tissue (H=1,O=8,C=6). Because of this difference in interaction probability, dose is overestimated by silver bromide films for low energy photon fields. This overestimation is displayed in Figure 2 relating the relative sensitivities of several dosimeters. Due to these difficulties, photographic films were not to measure the dose delivered by the ^{241}Am foil sources.

3.2.2.3 Radiochromic Film Dosimetry

Radiochromic film is a modern tool for photographic dosimetry similar to the radiographic films described above, but with a different chemical composition. Of the radiochromic film products available the GafChromic film produced by International Specialty Products of Wayne, NJ, is one of the most widely used, and much analysis of this product has been performed[5]. The GafChromic film consists of diacetylene monomer crystals suspended in a gelatin emulsion. The active layer is 30-40 μm for these films. These films have a varying energy response with photon energy. As shown in Figure 1, these films have reduced response at energies below 40 keV. Figure 2 relates the energy response of the Gafchromic HS, GafChromic MD-55-1, GafChromic MD-55-2 films to X-omat V film radiographic film and lithium fluoride thermoluminescence detectors which are discussed in Section 3.2.4.1

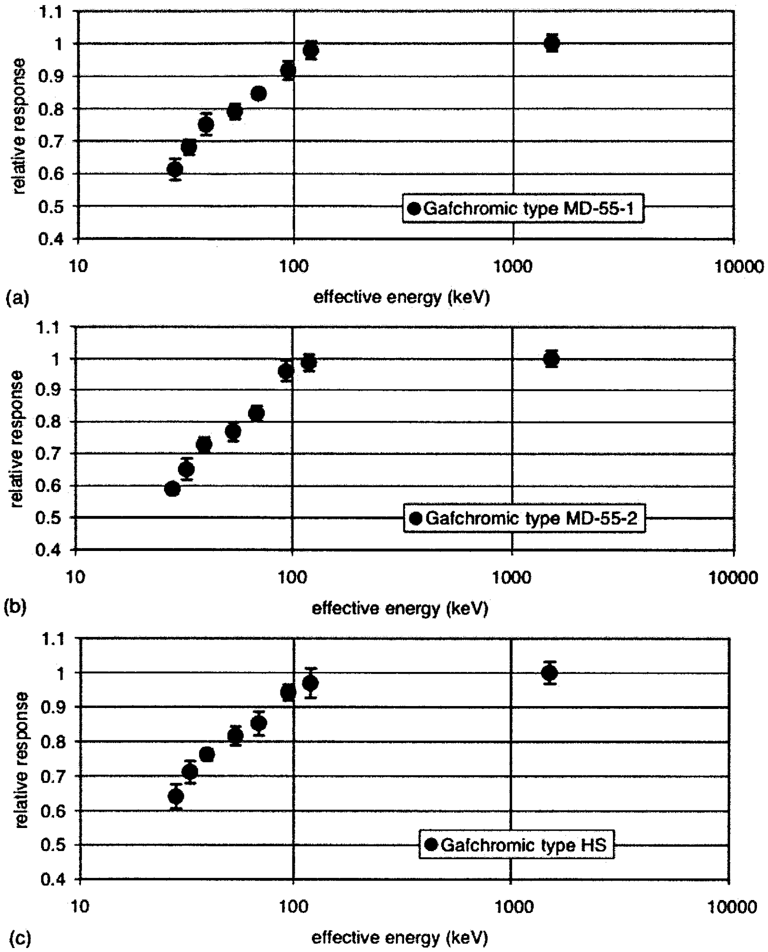

Figure 1. The energy response of GafChromic characterized for three different x-ray fields.

In this figure, note the reduced response for photon energies below 100 keV.

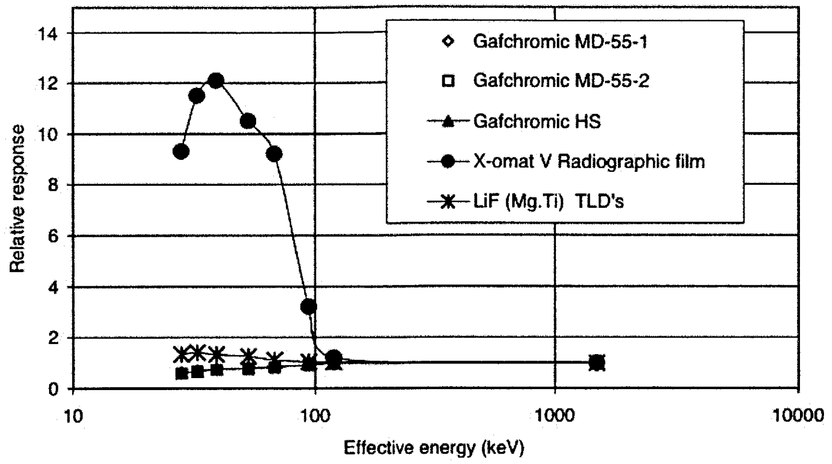

Figure 2. The relative energy response of several dosimetry methods.

In this figure, note the over-repsonse of the X-omat V silver bromide radiographic film and the under-response of the Gafchromic films for photon energies less than 100 keV.

Sayeg et al. suggest that this reduced energy response is due to the higher percentage of carbon in the film relative to tissue [6]. Beyond this under-response at lower energies, these films cannot be annealed and reused, making the cost per measurement much higher than other dosimeters which can be reused. For these reasons, radiochromic film was not used in our work with ^{241}Am.

3.2.3 Ionization Chambers

Ionizing radiation creates ion/electron pairs as it traverses matter. Since the number of charge pairs created corresponds directly with the amount of energy deposited in the medium, a measurement of dose can be obtained by measuring the number of ion pairs created. An ionization chamber is a device that collects the charge pairs created in a volume of gas using electrodes to which a potential difference is applied. As these charge pairs flow into these electrodes, the current they generate is measured using an electrometer, a sensitive current measurement device.

Many ion chamber designs exist. The chamber geometry, electrodes, wall thickness, and fill gas all determine the response of the chamber to ionizing radiation. Ion chambers may be used as either absolute dosimeters or relative dosimeters depending on how the current measurement is translated into a dose measurement [3].

If the mass of the ion-collecting gas within the ion chamber is known without resorting to calibration within a known radiation field, then the ion chamber is an absolute dosimeter. In this case, the relation between dose and charge is then given by the factor N_{gas}

$$N_{gas} = \frac{1}{m_g}\left(\frac{\overline{W}}{e}\right)_g \qquad \text{(Gy/C)} \qquad (3)$$

In this relation the factor $(\overline{W}/e)_g$ is the mean energy necessary to create an ion pair for the gas within the chamber, and m_g is the mass of the gas.

Ion chambers may also be used as relative dosimeters if this mass is not known. In this case the ion chamber is calibrated relative to an absolute dose measurement and the relation between dose and charge is then:

$$N_{gas} = \frac{D_{gas} A_{ion}}{M} \qquad \text{(Gy/C)} \qquad (4)$$

In this equation D_{gas} represents the mean absorbed dose in the cavity gas, A_{ion} is the ion-collection efficiency at calibration, and M is the electrometer reading at calibration.

In practice the ion-collecting gas mass is difficult to measure without a custom-made chamber. Commercially-available ion chambers are not machined with sufficient precision for this purpose, but absolute calibration is used at standards labs. NIST uses absolute open-air ion chambers for the development of radiation standards. Many other ion chamber designs have been designed and calibrated relative to these standards.

For many photon fields, such as a diagnostic radiation field in the 100-200 kVp energy range, attenuation in the chamber wall is not of concern since these fields have a negligible component below 30 keV. However for fields with significant numbers of photons with energy less than 30 keV, attenuation must be taken into account without a chamber specifically designed to avoid this attenuation effect [8]. This attenuation is due to the limited range (<27 μm for 30 keV electrons [9] in polycarbonate) of the electrons created within the chamber wall. Because some photons will be absorbed in the chamber wall without the ions created in the wall being measured, the dose measured will be less than the true dose. If the degree to which the dose is underestimated for low-energy photons is known, this effect can be corrected. By multiplying the dose measured by an ion chamber by an appropriate correction factor, these ion chambers may be used to measure dose delivered by photons with energy less than 30 keV as discussed by Wagner et al. [8].

For the dosimetry of ^{241}Am photons an ion chamber designed for energies 30 keV and above was applied with correction for the presence of photons of energy less than 30 keV using correction factors measured by Wagner et al. [8] and confirmed by MCNP simulation. Details of this application can be found below in Section 3.3.1.2.

3.2.4 Luminescence Dosimeters

When ionizing radiation interacts with a crystalline compound, charge pairs are created just as in any material. Some charge pairs will recombine, but in some crystalline compounds charge pairs will remain separate in an excited energy state. These separated charge pairs can be prompted to move about within the crystal under the influence of heat or optical light. As this movement occurs, the charge pairs recombine, releasing energy in the form of photons in the process. These photon emissions can be observed and used to derive a dose measurement.

This dose measurement must be computed based on knowledge of the radiation field since the luminescence signal does not correlate directly with the dose absorbed for all radiation fields. For a given radiation field, the interaction probability will be dependent on the material being exposed. Since crystalline compounds used in luminescence dosimetry do not have the same elemental composition as tissue, the interaction probabilities and thus the dose absorbed will be different for the crystalline compound and the tissue. Also the efficiency with which ion pairs are created without recombining may vary with the radiation field exposing the material. For these reasons, luminescence dosimeters must be calibrated relative to another dosimeter.

3.2.4.1 Thermoluminescence Dosimeters

Thermoluminescence is the production of photons due to recombination events prompted by heating of a crystalline material. Many thermolumenicent materials have been employed for the dosimetry of different radiation fields. Lithium fluoride crystals are one example of thermoluminescence dosimeters which have been used in a medical setting. The performance of these dosimeters has been evaluated at low energies as reported in Figure 2. These LiF dosimeters over-respond at energies below 100 keV.

For the purposes of measuring the dose from ^{241}Am foils in an experimental setting including inside tissue culture incubators, thermoluminescence dosimeters were not employed since they could be influenced by elevated temperatures. Instead an alternate mechanism of luminescence, optically stimulated luminescence, was investigated.

3.2.4.2 Optically Stimulated Luminescence

In the same way that thermal energy may promote some charge pairs to recombine within crystalline material, optical photons may produce this effect as well. In a dosimeter based on optically stimulated luminescence, the dosimeter crystal is shielded from optical light until readout. To obtain a dose reading, the crystal is exposed to a beam of optical light of a specific frequency. This light promotes the charge pairs to move within the crystal and to recombine at certain lattice sites within the crystal. When a recombination event occurs at one of these sites, a photon of a specific energy is released, as labeled as transitions 3b and 4a in Figure 3. These photons can be counted and used to derive a measurement of dose.

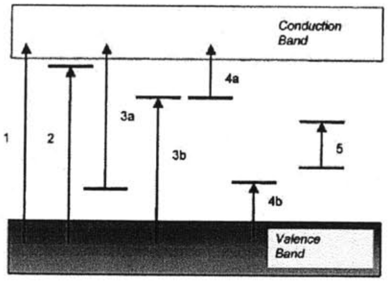

Figure 3. Diagram describing the theoretical model of optically stimulated luminescence [12].

Note the different transitions labeled in Figure 3. Transition 1 describes ionization across the band gap. Transitions 2 and 4b describe ionization to trap energy states which would not lead to optically stimulated luminescence. Transition 3a describes promotion of an electron out of a trap state by means other than optical stimulation. Transition 3b describes ionization to a trap state from which optically stimulated luminescence may be prompted. Transition 4a describes optically stimulated luminescence from a trap state. Transition 5 describes a transition between two trap states.

Optically stimulated luminescence must be calibrated relative to an absolute dosimeter. This calibration is necessary of the complex physical process involved that does not directly represent the energy delivered to the crystal. This process is described by the transitions labeled in Figure 3. Since the probabilities of these transitions depend on the radiation field involved, knowledge of the radiation field delivering the dose must be used to derive a dose from a luminescence measurement.

The relation between these transitions and the dose response of these crystals is not well known, but Gaza et al. have suggested that localized saturation effects may be responsible for reduced response [16]. This study evaluated the response of Al2O3:C crystals to several heavy charged particle fields. The dose response was compared to the linear energy transfer of charged particles. The linear energy transfer is a quantity which describes the density of energy deposition along the particle track as it traverses a medium. Linear energy transfer will be discussed in detail in Chapter 4.

For 4 MeV protons with a linear energy transfer of 9.7 keV/μm, a dose response of 0.693 ± 0.062 relative to the dose delivered was calculated, and this dose response decreased with increased linear energy transfer. This result is of note, since the linear energy transfer is 12 keV/μm for some of the secondary electrons produced by the ^{241}Am photons. The secondary electron spectrum produced by ^{241}Am is discussed extensively in Chapter 4.

For the nanodot OSL dosimeters produced by Landauer Inc. of Glenwood, IL, this energy response has been characterized relative to NIST standard sources for energies 16-662 keV. These nanodot dosimeters measure the dose delivered to a small crystal of Al_2O_3:C. They are 0.2 mm thick, allowing the observation of dose delivered to a thin layer of material. This small size is an important advantage over other methods for the measurement of dose to a thin layer of cells.

The Landauer nanodot dosimeter system offers several advantages for dosimetry in biological applications. The nanodot dosimeters are small (shown in Figure 4) and portable. They maintain a stable dose reading when elevated to biologically relevant temperatures, as described in Section 3.3.3.1.. They have a 0.38 mm window that limits attenuation at lower energies. They can be annealed and reused many times. For these reasons as well as the previous work [17] to characterize the response across a wide range of photon energies, these dosimeters were chosen for dosimetry of the ^{241}Am foils.

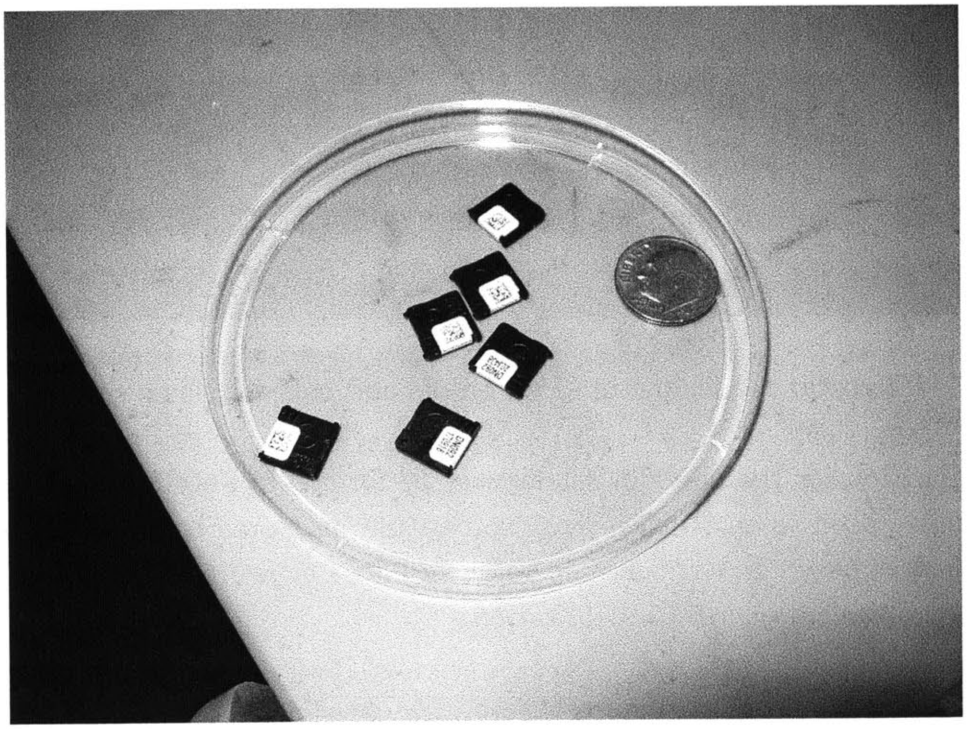

Figure 4. nanodots shown alongside a coin for size comparison.

The nanodot dosimeters measure dose delivered to an Al_2O_3:C semiconductor crystal. This dose measurement is read by exposing the crystal to a beam of monoenergetic light in the Microstar Reader (Number 8120148, Landauer, Glenwood, IL) as described by Akselrod and McKeever [13]. The Microstar

Reader pulses the crystal with a 540 nm photon source. Between pulses of light, a photodetector and photomultiplier circuit read out the number of 420 nm photons produced by luminescence processes within the crystal. This number is then correlated with a calibration factor in units of cGy/photon to yield information about the dose delivered to the crystal.

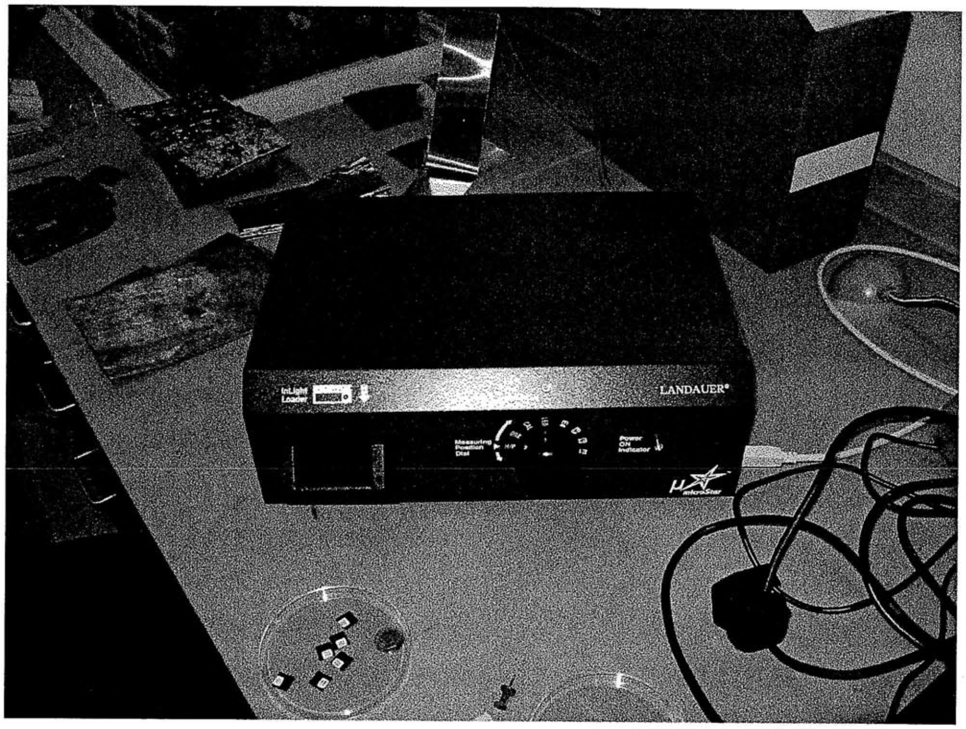

Figure 5. Microstar reader pictured with dots and coin for size comparison.

The calibration for the nanodot reader was performed in February 2010 using nanodots exposed to an 80 kVp x-ray source and measured by a NIST-traceable dosimeter. In the Sections below, all dose measurements reported have been obtained using this calibration.

3.2.5 Monte Carlo Simulation

Monte Carlo methods are a class of algorithms that generate results based on repeated random sampling. These methods have been applied to many problems in science, especially in problems involving particle tracking. In a Monte Carlo simulation of a problem involving particle tracking, a particle history is generated which accounts for the probabilities and consequences of interaction along the path of the particle. All probability distributions for interactions are input as pre-determined functions from which the method samples to generate the particle history.

Monte Carlo N-Particle Transport Code (MCNP) is a software package which implements the Monte Carlo method. MCNP includes a large library of interaction probabilities and particle physics which are used to model ionizing particles as they interact with matter. MCNP has been used to simulate nuclear fission reactors, particle accelerators, x-ray sources, medical imaging devices, and many other devices which make use of ionizing radiation.

MCNP version 5 (MCNP5) includes a full set of physics for low-energy photons including Compton scattering, tracking of secondary photoelectrons, and production of fluorescence photons. This physical model is used by default when MCNP is when photon energies below 10 MeV are considered. These features have been evaluated by Zamburlini et al. [14]. They simulated the fluorescence spectra produced by a ^{109}Cd source and detected by a Si(Li) detector. They found good agreement with experiment for low-energy fluorescence photons at 8.04 and 8.9 keV produced by the ^{109}Cd photons interacting with copper and also the 14.16 keV and 15.8 keV photons produced by the ^{109}Cd photons interacting with strontium. This study confirmed that MCNP5 is capable of accurately modeling photon interactions in energy range of interest for ^{241}Am photons. With this ability established, MCNP5 was to evaluate the dose delivered by ^{241}Am foil sources. The details of this simulation are included below in Sections 3.3.1.

3.3 Dosimetry Implementation

After considering the different technologies available for dosimetry of ionizing photons, ion chambers and optically stimulated luminescence detectors were chosen for the dosimetry of ^{241}Am photons. A Monte Carlo simulation of the sources was also developed in order to derive dose information. The following sections are a description of the methods used in these measurements and simulations. Using the data obtained, conclusions are made about the accuracy of the dosimetry methods used. A method of dosimetry for the various low-energy photon spectra produced by shielding the ^{241}Am foils is also presented.

These methods are dependent on knowledge of the photon spectra in question. In Chapter 2, a method is reported for gathering these spectra along with a selection of spectra. In any case in which dosimetry is based on knowledge of the energy spectrum, these spectra are included either here or above in Chapter 2.

3.3.1 Monte Carlo Simulation

As described in Section 3.2.5 MCNP is a versatile tool for the simulation of charged particle interactions in matter. MCNP5 code is utilized for the purpose of dosimetry of the low-energy photons emitted by the ^{241}Am foil sources in several instances. In one simulation MCNP5 was used to estimate the dose delivered to a monolayer of cells in culture on a foil source. In an attempt to make a comparison with the actual dose measured by an optically stimulated luminescence dosimeter, the dose delivered to such a dosimeter by the ^{241}Am foil was also modeled. Since dose per fluence varies with photon energy, MCNP5 was used to simulate the contribution to the total dose to a monolayer of cells from photons of different energies emitted by ^{241}Am.

3.3.1.1 Cell Monolayer Simulation

In order to use the ^{241}Am foils for tissue culture work, the dose being delivered by the foils must be known. One method of investigating this dose is to model a cell monolayer in a cell dish from a ^{241}Am foil with MCNP.

The source was defined as an isotropic surface source 7.62 cm wide and 35.56 cm long. A polystyrene cell dish of density 1.0 g/cm^3 was directly above the source. The bottom of this dish was 1 mm in thickness. Directly above this cell culture dish bottom was a 10 μm thick layer of tissue of 0.98 g/cm^3 representing a monolayer of cells. Directly above this layer was a 1 cm thick layer of water, representing the cell culture medium. This configuration is shown in Figure 6.

The heating (dose) per starting photon within a cell monolayer was simulated with the F6 tally. The F6 tally reports energy deposition within a specified cell of material per starting photon. The quantity calculated is described in Equation 5 in which ρ_a is the atom density, E is the energy of the photon energy, V is the volume of the cell of interest, Ω is the solid angle of the photon trajectory, $\sigma_t(E)$ is the total microscopic cross section for the photon energy E, .H(E) is the amount of energy deposited per collision for a photon of energy E, and $\psi(\vec{r},\hat{\Omega},E,t)$ is the angular flux of photons at $\vec{r},\hat{\Omega}$ with energy E at time t. In the calculations presented here time was not considered since the flux of photons from the ^{241}Am photons is constant in time.

$$F6 = \frac{\rho_a}{m}\int dE \int dt \int dV \int d\Omega\, \sigma_t(E) H(E) \psi(\vec{r},\hat{\Omega},E,t) \quad (\mathrm{MeV/g}) \qquad (5)$$

As described in Equation 6, the result is multiplied this by a factor corresponding to the number of starting photons per unit time to derive a dose rate. A dose-rate of 2.39 ± 3.76E-04 cGy/h was found.

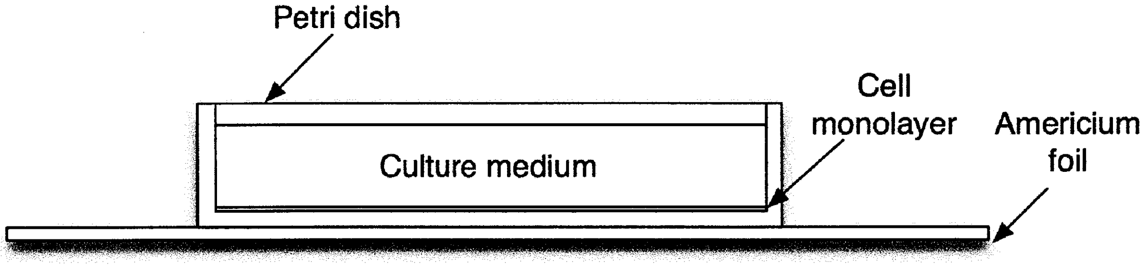

Figure 6. Cross Section of the simulation of the dose to a cell monolayer from a ^{241}Am foil (not to scale).

The number of starting photons per second was calculated as follows with N being the number of photons per second and A being the number of decays per second:

$$N\frac{\text{photons}}{\text{second}} = A\frac{\text{decays}}{\text{second}} \times 0.359\frac{60\,\text{keV gammas}}{\text{decay}} \times 2.73\frac{\text{photons}}{60\,\text{keV gamma}} \qquad (6)$$

The number of photons per 60 keV gamma photon was determined experimentally as described in Chapter 2.

3.3.1.2 Optically Stimulated Luminescence Simulation

In order to compare the dose-rate simulated by MCNP with experimental data, the dose delivered to a nanodot OSL dosimeter was simulated. A diagram of this simulation in shown in Figure 7.

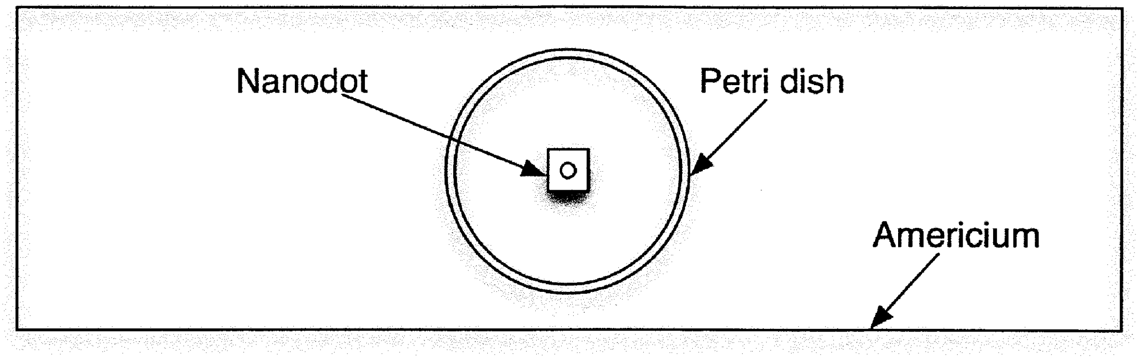

Figure 7. Diagram of the MCNP experiment of the dose to an OSL dosimeter.

The F6 tally within the dosimeter crystal cell varies if the crystal is modeled as Al_2O_3 or if tissue is substituted. Using the same conversion factor from dose per starting photon to dose per second as shown above, dose-rates were found to be 2.65 ± 3.76E-04 cGy/h and 1.03 ± 3.48E-04 cGy/h for the Al_2O_3 material and tissue material respectively.

Although exact correlation between experimental and MCNP5 dosimetry results was not expected, MCNP5 was helpful in determining the relative dose contributions of the different photons emitted by the ^{241}Am foil sources. For this reason, the simulation which most closely correlated with experimental dose measurements was chosen for this effort as described in Section 3.3.1.3.

Of all these MCNP5 results the dose to a cell monolayer correlates most closely with experimental observations of dose from the ^{241}Am foil sources. For this reason, this cell monolayer configuration was used to model the relation between dose and fluence across the ^{241}Am photon energy range.

3.3.1.3 Simulation of Dose/Fluence Relationship for a Cell Monolayer Exposed to Monoenergetic Sources

The probabilities of interaction, energy transfer or absorption vary greatly with photon energy due to large differences in mass attenuation coefficients across the range of low-energy photons. In order to develop an understanding of the relative dose contributions from the different photons in the ^{241}Am spectrum, a dose per unit fluence function was derived using MCNP simulation.

The same simulation setup as described in Section 3.3.1.1 was used modifying only the source definition. The source was defined with the same geometry as described in 3.3.1.1, but with only one photon energy per simulation. Several simulations with different photon source energies were combined in order to provide enough data for the dose per fluence function. This function is shown in Figure 8 in the form of a weighting factor which can be multiplied by an energy spectrum to derive a dose-weighted energy spectrum. These dose-weighted energy spectra are shown in Chapters 2 and 4 in order to convey the relative contributions of the photons of different energies emitted from the ^{241}Am sources.

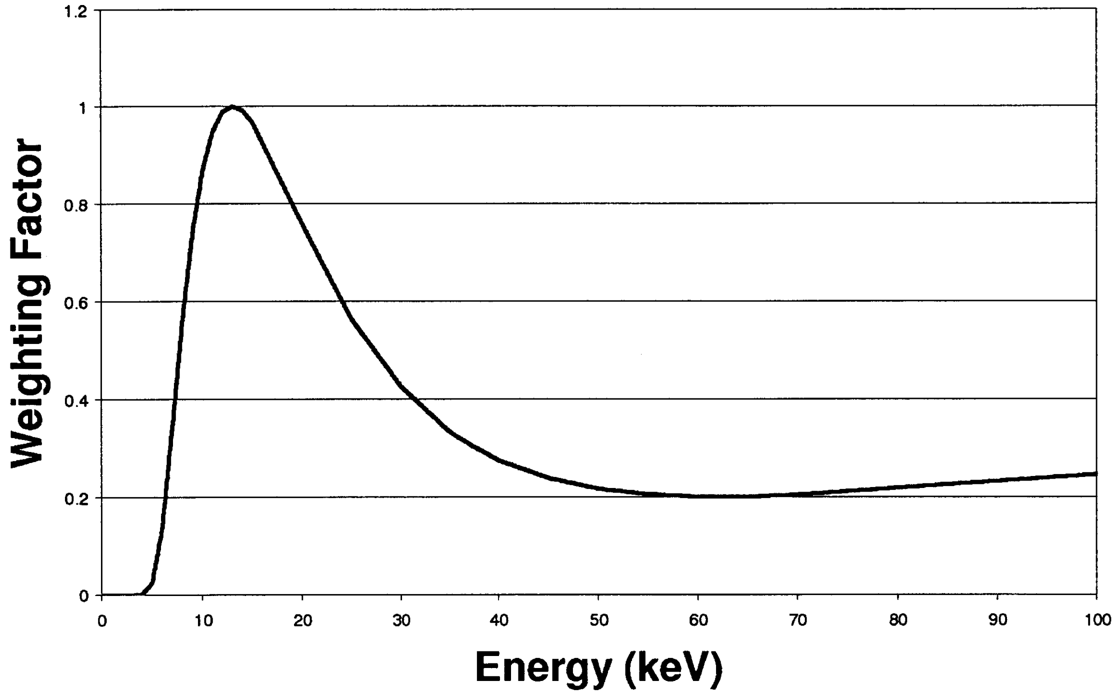

Figure 8. Dose-weighting factors found using MCNP for energies 5-100 keV.

3.3.2 Ion Chamber Measurements

Specialized ion chambers have been designed and employed to perform dosimetry of photons below 40 keV [8]. There are also several ion chambers available commercially with constant energy response in the 30-60 keV range [10]. However, for the purpose of dosimetry of ^{241}Am with its photons ranging from 10-60 keV, there is no published record of an ion chamber with a constant energy response through this entire range. The use of a cavity ion chamber was investigated along with correction factors for the lowest energy photons from the ^{241}Am spectrum since these correction factors have been measured and reported in the literature for mammography spectra [8]. These correction factors are described below in Section 3.3.2.1.

For the measurements below the 10x6-6 6cc ion chamber was used (03-0534, RadCal, Monrovia, CA). Readout was supplied by the Ion Chamber Digitizer (Number 01-2062, RadCal, Monrovia, CA) and AccuPro 9096 (Number 96-0293, RadCal, Monrovia, CA). This electrometer and chamber combination was calibrated with a 60 kVp x-ray source on June 17th, 2009, less than one year before use for these measurements. This dosimeter setup is pictured in Figure 9.

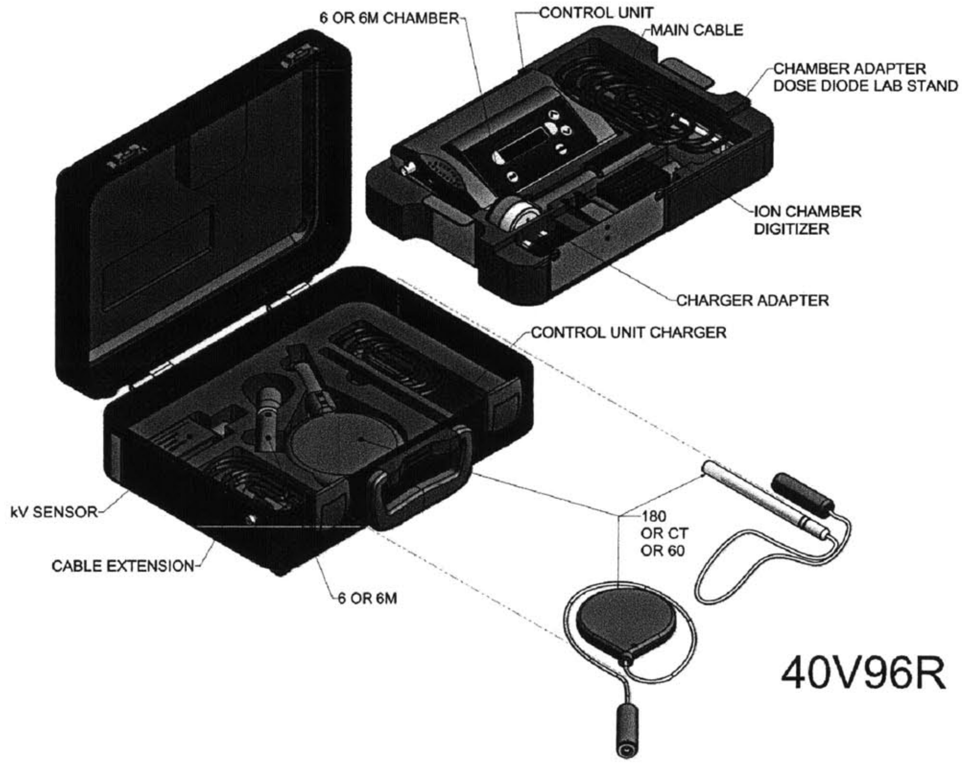

Figure 9. The Radcal dosimetry system including the electrometer, digitizer, and chamber.

3.3.2.1 Correction Factors for Low-Energy Photons with the Radcal Dosimeter

Photon attenuation in matter increases with decreasing photon energy across the lower range of the photon energies produced by the ^{241}Am foils. For example, the mass attenuation coefficient for carbon is 2.37 $\mathrm{cm^{-2}g^{-1}}$ for 10 keV photons and 0.256 $\mathrm{cm^{-2}g^{-1}}$ for 30 keV photons [15]. In order to measure the dose delivered by these lower energy photons with a closed-chamber ion chamber, the dose measured must be corrected for the photons attenuated in the wall and electrode material.

The wall of the Radcal ion chamber is 0.3048 ± 0.0254 mm thick Lexan 1001 polycarbonate, and the electrode is 0.3048 ± 0.0254 mm thick carbon graphite. In this thickness of material, for photons traveling perpendicular to the ion chamber wall, the expected attenuation is 22.0% ± 1.6% for 10 keV photons to 1.8% ± 0.2% for 60 keV photons across the range of photon energies of the ^{241}Am foils [15]. However, all photons will not be impacting the ion chamber wall at right angles due to the angular distribution of photons emitted by the foil source was well as the curvature of the ion chamber wall, which is cylindrical. For this reason attenuation in the wall and electrode was investigated using simulation and literature data. These simulation and literature data and the correction factors they predict are discussed in the sections below.

3.3.2.1.1 Ion Chamber Simulations

Wagner et al. have studied the efficiency of detection of low energy photons with the Radcal 6cc ion chamber [8]. They report that for a 20 kVp spectrum with a half-value layer of 0.15mm aluminum, the chamber requires a correction factor of 1.25 in order to match the dose measured by mammography ion chambers specifically designed and calibrated for these low energy spectra. They also report a correction factor of 1.10 for a 30 kVp spectrum with a half-value layer of 0.2 mm aluminum.

Using the method of Poludniowski et al.[18,19] implemented in the SpecCalc software program, the x-ray spectra used in these measurements were reproduced. This method produces bremsstrahlung energy spectra and half-value layer data based on a theoretical approach which accounts for the depth of penetration of electrons into the anode of the x-ray tube.

For the 20 kVp spectrum, the potential was set to 20 kV. Shielding of 600 mm air (as used by Wagner et al. [8]) and 0.2 mm aluminum was used to adjust the aluminum half-value layer (HVL) to be 0.15. For the 30 kV spectrum, the potential was set to 30 kV. Shielding of 600 mm air and 0.435 mm aluminum was used to attain a HVL of 0.20 mm.

These spectra were tabulated and input as a source definition in MCNP. The source was defined as a point source 600 mm from the ion chamber body. The ion chamber air volume was defined as a cylinder 1 cm in radius, and 1.91 cm in length for a total volume of 6 cm^3. The density of air in this volume was defined as 1.297E-3 g/cm^3. For simulations without the chamber and wall, the energy deposited to this volume of air was calculated with the MCNP F6 tally, which reports energy deposited per starting photon. For simulations with the chamber and wall, surrounding the ion chamber was the graphite electrode. A 0.03048 cm thick layer of graphite bordered the air chamber around the cylinder and on one end. The density of this graphite was entered as 2.3 g/cm^3. A 0.03302 cm layer of lexan polycarbonate wall was positioned immediately beyond the electrode around the cylinder body and on one end. The density of this polycarbonate was entered as 1.2 g/cm^3. On the end without a wall or electrode layer, a 1 mm layer of lead of density 11.35 g/cm^3 was used to shield the chamber. This layer was used because the Radcal chamber has electronic connections at one end which shield the chamber. The energy deposited to the air chamber was calculated with an F6 tally as above. These configurations are shown in Figures 10 and 11.

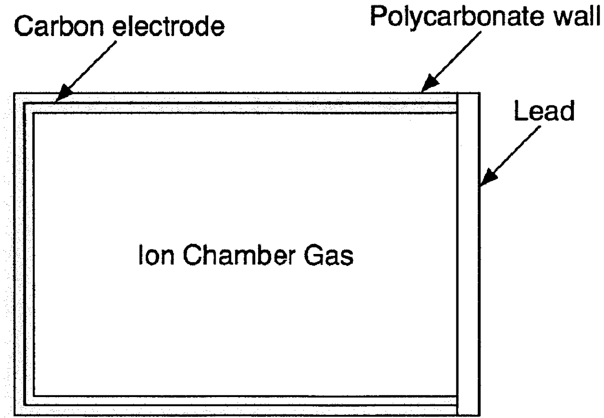

Figure 10. Ion chamber model used in MCNP simulation including wall and electrode (not to scale).

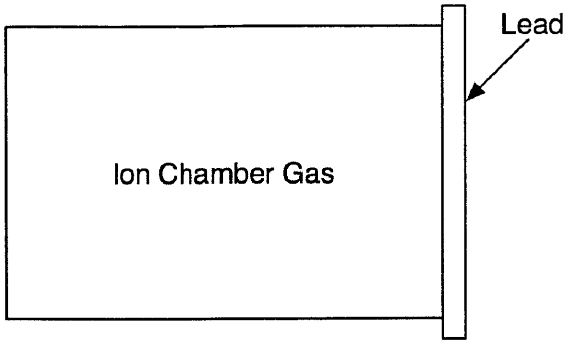

Figure 11. Ion chamber model used in MCNP simulation with no wall or electrode (not to scale).

For both energy spectra, the energy deposited to the air cylinder was compared for the case with and without the surrounding wall/electrode. The results are shown in Table 1. With these data, there is agreement with the experimental results reported by Wagner et al. for this chamber and these energy spectra.

Potential	Energy per photon (wall) (Gy/photon)	+/-	Energy per photon (no wall)	+/-	Correction factor	+/-	Wagner et al.
20 kV	5.45E-17	5.15E-19	6.78E-17	4.72E-19	1.24	0.01	1.25
30 kV	3.53E-17	4.88E-19	3.91E-17	4.68E-19	1.11	0.02	1.10

Table 1. Correction factors due to attenuation in Radcal ion chamber wall and electrode.

3.3.2.1.2 MCNP Model to Determine Ion Chamber Efficiency

Having validated the model of the ion chamber in MCNP with experimental data in Section 3.3.2.1.1, this model was used to develop an energy efficiency function for the ion chamber. The same dimensions as above were used but the source definition was altered. A total of 26 simulations were performed for monoenergetic sources from 5 keV to 30 keV. For each of these configurations, the difference in energy deposition between the shielded and unshielded chamber was calculated. These data are reported in Table 2. From these data, correction factors for the ion chamber were generated. These correction factors can be used to account for the attenuation of photons within the chamber wall.

Energy (keV)	Energy per photon (Gy/photon)	+/-	Energy per photon	+/-	Correction Factor	+/-
5	3.74E-17	1.55E-18	2.01E-18	7.10E-19	18.61	6.62E+00
6	8.10E-17	8.79E-19	1.95E-17	1.82E-18	4.15	3.90E-01
7	1.20E-16	6.18E-18	4.92E-17	9.88E-19	2.45	1.35E-01
8	1.18E-16	5.40E-18	6.62E-17	7.29E-19	1.79	8.39E-02
9	1.14E-16	4.84E-18	7.31E-17	6.09E-19	1.55	6.74E-02
10	1.02E-16	4.57E-18	7.37E-17	5.42E-19	1.38	6.29E-02
11	8.93E-17	4.41E-19	7.20E-17	4.94E-19	1.24	1.05E-02
12	7.84E-17	4.29E-19	6.58E-17	4.75E-19	1.19	1.08E-02
13	6.78E-17	4.22E-19	5.87E-17	4.58E-19	1.15	1.15E-02
14	6.01E-17	4.14E-19	5.27E-17	4.43E-19	1.14	1.24E-02
15	5.27E-17	4.09E-19	4.74E-17	4.33E-19	1.11	1.33E-02
16	4.73E-17	4.04E-19	4.34E-17	4.21E-19	1.09	1.41E-02
17	4.15E-17	4.04E-19	3.89E-17	4.19E-19	1.07	1.55E-02
18	3.71E-17	4.02E-19	3.55E-17	4.15E-19	1.05	1.67E-02
19	3.31E-17	4.02E-19	3.19E-17	4.14E-19	1.04	1.85E-02
20	3.01E-17	4.05E-19	2.91E-17	4.13E-19	1.03	2.02E-02
21	2.71E-17	4.02E-19	2.64E-17	4.10E-19	1.03	2.20E-02
22	2.50E-17	4.00E-19	2.46E-17	4.05E-19	1.01	2.33E-02
23	2.30E-17	3.99E-19	2.25E-17	4.05E-19	1.02	2.56E-02
24	2.08E-17	3.96E-19	2.02E-17	4.02E-19	1.03	2.83E-02
25	1.94E-17	3.95E-19	1.88E-17	4.01E-19	1.03	3.03E-02
26	1.76E-17	3.99E-19	1.73E-17	4.04E-19	1.02	3.31E-02
27	1.64E-17	3.99E-19	1.61E-17	4.04E-19	1.02	3.55E-02
28	1.53E-17	4.00E-19	1.50E-17	4.05E-19	1.01	3.82E-02
29	1.44E-17	4.01E-19	1.42E-17	4.05E-19	1.01	4.05E-02
30	1.34E-17	4.03E-19	1.33E-17	4.06E-19	1.01	4.32E-02

Table 2. MCNP-determined correction factors for the dose measured by the Radcal ion chamber for monoenergetic sources.

These simulation data have been combined with the manufacturer-provided efficiency function for the 6cc ion chamber shown in Figure 7 to yield the calibration factors described in Figure 8. These data were obtained by using the Radcal 6cc ion chamber to measure the dose of the NIST standard sources M60, S60, M100, M150, M200 and ^{60}Co sources [11].

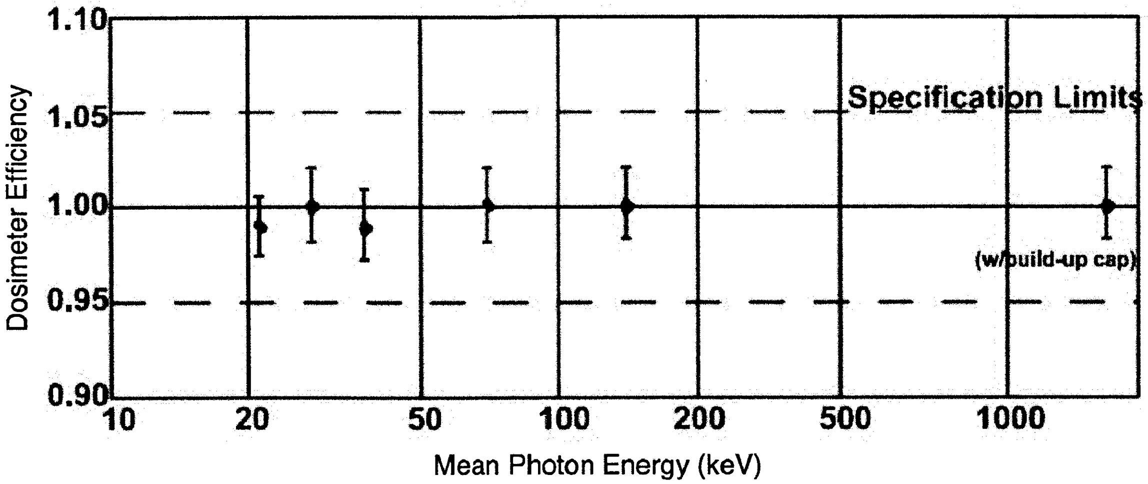

Figure 7. Energy efficiency for the Radcal 6cc ion chamber dosimeter.

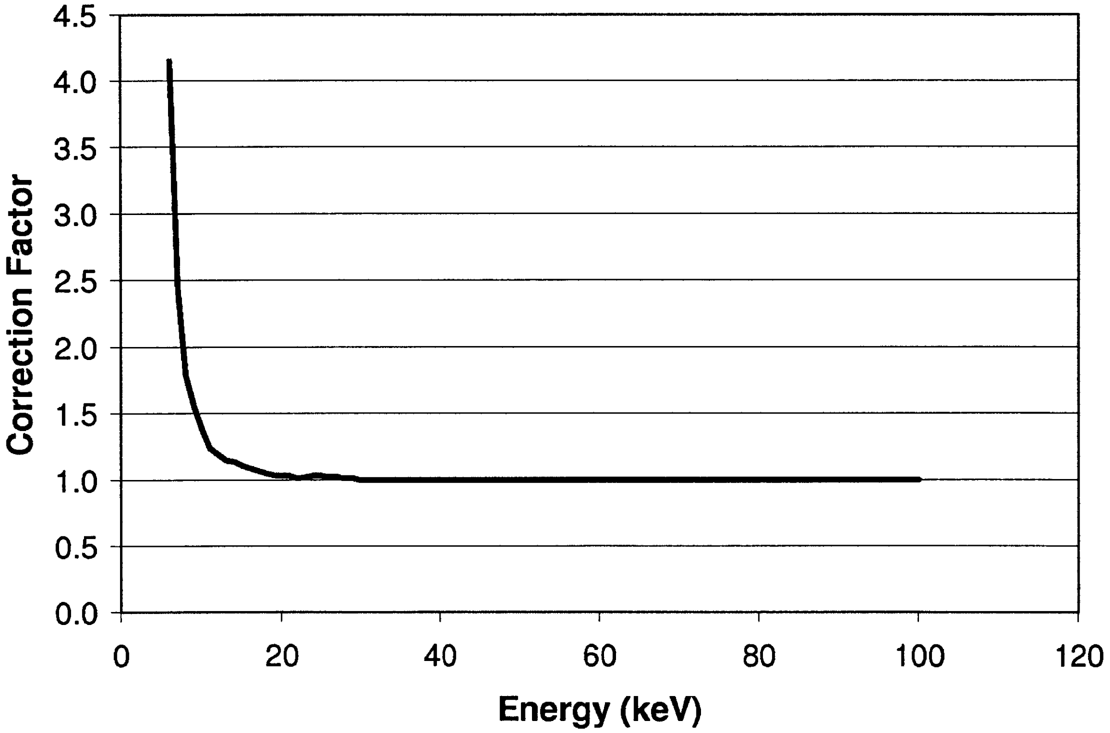

Figure 8. Correction factors for the Radcal 6cc ion chamber based on simulation and experimental data.

Figure 8 shows the correction factors to be applied when measuring radiation fields of low-energy photons. When this function is weighted over the energy spectrum, a dose estimate corrected for attenuation at lower energies is obtained. This method is described in full detail in the dosimetery implementation section below.

3.3.2.2 Uncertainty Analysis

The AccuPro dosimeter system has a manufacturer-determined uncertainty of 5% due to calibration [13]. For instantaneous dose-rate measurements for which three values were gathered, reader uncertainty was taken as the standard deviation of these three values.

The total dose, D, is the product of the calibration correction factor, C, and the dose reading, R:

$$D = C \times R \qquad \text{(cGy)} \qquad (9)$$

For accumulation measurements, the uncertainty is then dependent on the uncertainty of the calibration factor, ΔC:

$$\Delta D = R\Delta C \qquad \text{(cGy)} \qquad (10)$$

For instantaneous measurements, which have larger reading uncertainty ΔR, the uncertainty is then:

$$\Delta D = \sqrt{(C\Delta R)^2 + (R\Delta C)^2} \qquad \text{(cGy)} \qquad (11)$$

3.3.2.3 Measuring Bremsstrahlung Spectra from 75-250 kVp

In order to confirm the accuracy of the dosimeter systems used in this project, dosimetry was performed for several photon fields. Dosimetry was performed for the photon fields produced by the RT250 x-ray tube (Number 923808, Philips Medizin Systeme, Hamburg, Germany) for the tube potentials 75, 100, 150, 250 and 250 kV with filtration of 0.1 mm Cu, 0.2 mm Cu, 0.35 mm Cu, 0.5mm Cu, 1.0 Cu, and a Thoraeus filter consisting of 0.25mm Cu with 0.4mm Sn.

For each voltage and filtration setting, the dose-rate was sampled continuously for 30 seconds. For each measurement, current was applied to the tube for a period of thirty seconds and the dose was allowed to accumulate during this time. The dose-rates for each setting are reported in Table 3 for each energy and filtration setting at a focal spot distance of 36.4 cm.

	0.1 Cu	+/-	0.2 Cu	+/-	0.35 Cu	+/-	0.5 Cu	+/-	1.0 Cu	+/-	0.4 Th	+/-
75 kVp	52.52	2.63	21.80	1.09	10.54	0.53	5.97	0.30	1.81	0.09	0.48	0.02
100 kVp	91.56	4.58	45.44	2.27	26.60	1.33	17.88	0.89	8.01	0.40	3.26	0.16
150 kVp	187.06	9.35	116.00	5.80	81.54	4.08	63.56	3.18	38.04	1.90	22.42	1.12
200 kVp	274.00	13.70	193.96	9.70	150.76	7.54	125.96	6.30	86.74	4.34	61.14	3.06
250 kVp	353.60	17.68	267.20	13.36	219.00	10.95	189.90	9.50	140.36	7.02	106.92	5.35

Table 3. Ion chamber dose readings in cGy/min for various photon spectra produced by the RT250 x-ray tube with the energy and filtration settings shown.

3.3.2.4 Dosimetry for ^{241}Am with Various Shielding Configurations

The energy spectrum emitted by the ^{241}Am foils is unlike any energy spectrum emitted by a bremsstrahlung x-ray source. As described in Chapter 4, the discrete low-energy component contributes approximately half of the total dose delivered by the ^{241}Am foils according to MCNP calculations. Because these low-energy photons are attenuated to a significant degree by the chamber wall and electrodes (as reported in Section 3.3.2.1), the dose measured by an ion chamber will be less than the dose delivered to an amount of tissue at the same location.

The dose-rates delivered by ^{241}Am foils with various degrees of shielding were measured in order to understand the energy dependence of the ion chamber for the 10-30 keV photons of this spectrum. Since shielding the ^{241}Am foils reduces the number of lower energy photons more than the number of 60 keV photons, it was possible to determine the performance of the Radcal Ion Chamber setup for several different energy spectra of interest.

For these experiments, the Radcal AccuPro electrometer was set to continuous readout and allowed to measure the dose-rate directly above the shielding for each of several shielding configurations. After the dose-rate reported had stabilized, three readings were recorded. The data obtained from these measurements are reported below in Section 3.4 along with corrections applied to account for attenuation of low-energy photons.

3.3.3 Optically Stimulated Luminescence Dosimetry Measurements

The following sections contain several sets of data obtained using the Landauser OSL dosimeters. The method for maximizing accuracy and precision of measurements obtained with these dosimeters is presented first.

3.3.3.1 Best Practices for Gathering Data with OSL Dosimeters

There are many possible methods of employing the Landauer OSL dosimeters to measure the radiation fields of concern to us. Several experiments were conducted in order to find the methods which yield the most accurate and precise data. Much of the data measured have been collected with the goal of finding accurate dosimetry information about a radiation field of interest. In addition to this, statistics also yield useful information about the measurement methods. After observing statistics of differing quality with different methods, the differences in methods were analyzed in order to determine a method of data collection which maximizes both accuracy and precision. The determination of this method does not exclude the possibility of other methods which produce equally precise and accurate data. Instead this method is presented as one which was found to provide the best data among the variations which were examined.

3.3.3.1.1 General Methods

In all methods, the basic procedure for acquiring dose data is the same. A dot is first scanned with an optical bar code reader and is then inserted into the Microstar reader. The dial is turned to the read E1 measurement position, and the readout is recorded by the Microstar Reader software program. This process is repeated twice in order to gain a sense of the variance inherent in the measurement of a single dot. This method was used in all instances in which the Landauer OSL dosimeters were used to gather data reported in this report unless otherwise noted.

3.3.3.1.2 Dot Annealing

In order to gather measurements with the highest precision possible, the effect of annealing on the precision of data was investigated. Annealing is the process of pumping electrons out of trap energy states and into conduction band energy states using optical photons. As a nanodot is annealed, the information about the dose absorbed in previous radiation exposures is lost. This reduces the dose reported by the Microstar reader upon reading the dosimeter. Since the measurement of dose is proportional to the photon intensity observed in this reading process, and the variance in this photon intensity is directly proportional to the photon intensity, the variance in the dose reported is directly proportional to the photon intensity and the number of electrons in trap energy states. This means that the variance in any dose reading will increase with the magnitude of the reading.

When a dot is used to gather a dose measurement, it is read before and after the radiation exposure. Two readings are necessary since a residual dose is always present in the nanodot. Thus all measurements of dose have two data points, and each has an associated variance. The effect of the variance of the residual dose on the final measurement was investigated by examining the coefficients of variance of measurements taken with two sets of dots.

Initially both sets of dots were annealed fully by exposing the dots to visible light for 48 hours with the Fujifilm IP Eraser (Fujifilm, Tokyo, Japan). One set of dots was then exposed to the Am foil source in order to achieve a dose reading of approximately 1 cGy. The other set of dots was left annealed. Both sets of dots were then measured with the Microstar reader in order to determine the initial dose measurement and variance. Each measurement of the dots was conducted in triplicate, as are all dot measurements in this report, in order to gain an understanding of the variance in the measurement. Both sets of dots were then exposed to the ^{241}Am foils for a period of 20 seconds in order to deliver an additional dose of approximately 0.01 cGy. Following the exposure, the final dose measurement and variance were recorded.

The dose data for this experiment, including the variance and coefficient of variance for the different set of measurement are reported in Table 4.

	Dose Average (cGy)	Interdot STDEV (cGy)	Dose Coefficient of Variance
Pre-annealed	0.011	0.0011	0.10
Not pre-annealed	-0.010	0.100	-9.79

Table 4. The coefficient of variance of the measurements taken with annealed and non-annealed dots.

These results show that annealing dots before taking measurements does improve the precision of the data. This improvement is most evident from the comparison of the coefficient of variance from each set of measurements. This factor, which is defined as the standard deviation divided by the mean, relates the error in the measurement to the measurement itself. For the unannealed dots, the error in the measurement was greater in magnitude than the average in the measurement.

3.3.3.1.3 Dot Handling Effects

Another factor which could affect the variance of dose measurements is the physical handling history of the dots. In some experiments with mice, the nanodot crystals were removed from their holder using a soft rubber-tipped pencil and placed in various places within dead mice using forceps. In the process some dots were stained by mouse tissue. Other dot crystals were seen to have their thin plastic coating slightly loosened after being exposed to mice tissue. When the dots were placed back into their holders using tweezers and pushed into their locked position with a soft rubber-tipped pencil, some dots were bent in the process.

These handing issues did not compromise the ability of the dots to record and report dose readings. Initially it was unclear whether they affected the accuracy or precision of the data obtained from them, so the effect of these handling methods on the data statistics was investigated. Using a set of 24 nanodots with various handling histories, the dose delivered by an Am foil in a period of 18.5 hours was measured. Dots were first annealed for 48 hours and read to observe any residual dose. The dots were then placed in petri dishes with the same spatial orientation. The dishes were then placed on an ^{241}Am foil, taking care to keep the dots in line in the center of the foil. This allowed the dose delivered to be as uniform as possible for the entire set of nanodots, since the activity of the ^{241}Am foils are uniform over their surfaces. The dots were exposed for a period of 18.5 hours.

Handling procedures showed an impact on both the accuracy and precision of the measurements taken. Data are reported for dots with no evidence of abuse and dots with history of use in mice in Tables 5 and 6. For these tables, the residual column displays the mean residual reading of dose found when the dosimeter was read three times. The intradot STDEV reports the standard deviation of these three readings. The intradot COV reports the coefficient of variance, the STDEV divided by the mean residual measurement. The dose average column reports the dose found after subtracting the residual dose reading from the mean of the three dose readings performed after exposure. The STDEV column reports the standard deviation of these three readings. The dot DOV reading reports the coefficient of variance for this dose measurement, the STDEV divided by the mean final dose. The combined row indicates the mean of the dose reported by each of the dosimeters. The STDEV of the combined reading is the standard deviation of these ten readings. The combined coefficient of variance (COV) is the standard deviation divided by the mean of the combined dose readings.

Dot Number	Residual (cGy)	Intradot STDEV (cGy)	Intradot COV	Dose Average (cGy)	STDEV (cGy)	Dot COV
DA09246387D	7.38E-03	1.90E-04	0.03	24.65	0.14	0.01
DA092568491	2.18E-03	4.80E-04	0.22	23.55	0.37	0.02
DA09257408E	9.23E-03	4.00E-04	0.04	23.97	0.31	0.01
DA09257979V	7.25E-03	3.20E-04	0.04	23.53	0.68	0.03
DA09258344J	4.13E-03	2.20E-04	0.05	24.69	0.17	0.01
DA09263358D	7.34E-03	3.80E-04	0.05	22.79	0.08	0.00
DA09263374J	9.35E-03	7.60E-04	0.08	23.33	0.05	0.00
DA09263520S	1.05E-02	5.90E-04	0.06	23.27	0.60	0.03
DA09263826A	2.12E-02	8.50E-04	0.04	24.49	0.14	0.01
DA092638864	7.26E-03	6.80E-04	0.09	23.00	0.49	0.02
DA092639185	3.80E-03	2.00E-04	0.05	24.06	0.17	0.01
Combined				**23.76**	**0.750**	**0.03**

Table 5. Dose data acquired with nanodots with good handling histories.

Dot Number	Residual (cGy)	Intradot STDEV (cGy)	Intradot COV	Dose Average (cGy)	STDEV (cGy)	Dot COV
DA09246305P	1.22E-02	9.00E-04	0.07	19.21	0.25	0.01
DA09246374K	1.80E-03	2.50E-04	0.14	15.49	0.28	0.02
DA09246380R	3.51E-03	3.50E-04	0.10	17.06	0.08	0.00
DA09246681J	1.51E-03	1.70E-04	0.11	17.51	0.58	0.03
DA09257969W	3.00E-03	5.80E-04	0.19	24.46	0.69	0.03
DA09258575A	1.54E-02	6.60E-04	0.04	22.92	0.18	0.01
DA09258645B	5.61E-03	6.80E-04	0.12	19.77	0.22	0.01
DA09258662F	3.74E-03	5.00E-04	0.13	24.97	0.14	0.01
DA09263309G	2.74E-03	6.00E-05	0.02	20.19	0.37	0.02
DA09263319F	8.94E-03	5.10E-04	0.06	19.24	0.14	0.01
DA09263380Q	1.68E-03	2.80E-04	0.17	19.17	0.89	0.05
DA092638583	7.86E-03	1.60E-04	0.02	21.18	0.16	0.01
DA092639656	7.16E-03	7.50E-04	0.11	22.93	0.20	0.01
Combined				**20.32**	**2.90**	**0.14**

Table 6. Dose data acquired with nanodots which had been inserted into mice in previous experiments.

In Table 6 note that the dose measured by these dots is lower than that measured by dots with good handling histories. Also note that the coefficient of variance is 0.14, which is greater than that observed (0.03) for dots with good handling histories.

The data here show an impact of handling on the accuracy and precision of the measurements. Data taken with dots with no history of abuse show the greatest precision.

At the end of the 18.5 hour period, the dots were read using the Microstar reader. The data was recorded and the handling history of each dot used was investigated.

3.3.3.1.4 Thermal Annealing of Nanodots

In this experiment the effect of heat on the accuracy of nanodot dosimeters was investigated. Biological samples are often grown at 37 ºC, and since the nanodots were designed for use at room temperature, it was necessary to investigate the possibility of thermal annealing of the nanodot dosimeters. Six dots were irradiated on an ^{241}Am foil for 1 hour in order to attain an uncorrected dose reading of approximately 1.5 cGy. Three dots were then read and subsequently incubated at 37 ºC for 3 hours. Three dots were read and kept at room temperature for 3 hours. The dots were read again after incubation in order to gather an understanding of the extent to which thermal annealing had occurred. This process was repeated for another period of 15 hours in order to investigate long term effects of elevated temperatures.

For the nanodot dosimeters used in this experiment, the dose measurements were consistently within experimental uncertainty. This consistency is displayed in Figure 12 showing the average of three relative dose measurements defined as the average of three readings after thermal exposure divided by the average of three readings before thermal exposure. This suggests that the nanodot dosimeters yield consistent dose data at both 20 ºC and 37 ºC.

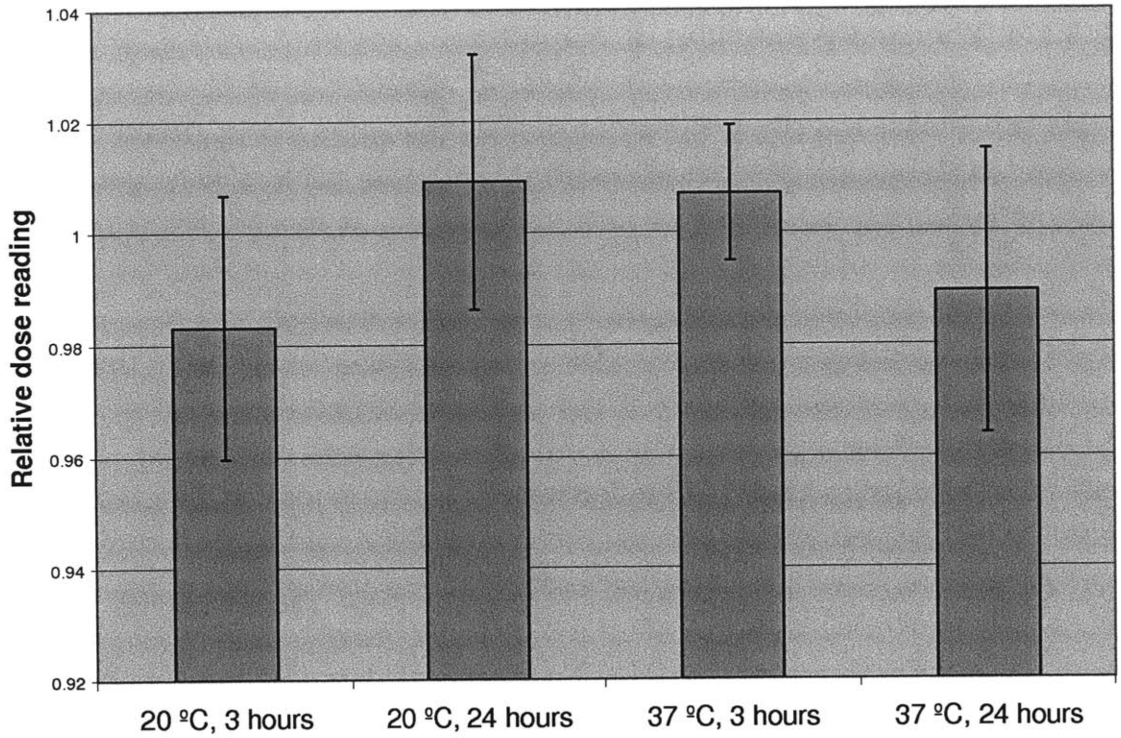

Figure 12. Temperature effects on relative dose measurements.

These experiments have established methods of using nanodot dosimeters which will maximize the precision of the dose data obtained. The method used to maximize precision using the nanodot OSL dosimeters is described in Section 3.3.3.1.5

3.3.3.1.5 Standard Procedure for Measuring Dose with OSL Dosimeters

In order to gather dosimetry data most reliably and consistently with the nanodot dosimeters, a standard procedure was followed. This procedure is not presented as the only method of producing satisfactory results, but instead it is the method which was found to provide the greatest accuracy and precision for the general dose measurement. The procedure is outlined here:

1. Read the required number of properly-handled dots. For a single dose measurement, three dots should be used. If the residual dose registered in this step is below 0.01 cGy, then the dots can be used to absorb dose without first annealing. Skip to step 3.

2. Anneal the dots for 48 hours using the IP Eraser 3 or natural sunlight. Read the dots in triplicate. Observe that the residual dose is less than 0.01 cGy. If the residual is greater, repeat this step.

3. Place the dot in a container similar to the container which will hold the biological specimen to be measured. For example, a Petri dish, a well plate, or a mouse. Do not remove the dot from its protective casing.

4. Read the dots in triplicate with the Microstar reader.

3.3.3.2 Energy Dependence of OSL Dosimeters

The energy dependence of optically stimulated luminescence crystals prohibits the assumption of a constant dose response across the range of low-energy photons important in this study [17]. In order to use these dosimeters for dosimetry of ^{241}Am, literature data and other dosimeters were used in order to establish the accuracy of the Landauer nanodot OSL dosimeters. These data are presented in the following sections.

3.3.3.2.1 Energy Dependence Found Using NIST-standard Measurements

In order to characterize the nanodot dosimeters for use across a wide range of x-ray spectra, Yanhke et al. [17] have measured the response of the nanodot dosimeters to the NIST standard x-ray sources NS20, M30, NS30, M50, NS40, M60, S60, S75, NS80, M150, NS100, NS120, H150, NS150, and NS250 as well as several other sources from the International Electrotechnical Commission (IEC) and Landauer. These sources are described in Table 1.

With the dose delivered to the nanodots known, these dots were then read with a reader calibrated at 80 kVp (3.25 mm Al filtration, 44 keV mean energy). The differences between the true dose and the dose measured by the nanodot are reported in the form of correction factors in Table 6.

Beam Code	Correction Factor	Mean Energy	kVp	Filtration
NS20	1.49	16	20	1 mm Be + 1 mm Al

M30	1.39	20	30	4.5 mm Al
NS30	1.16	24	30	1 mm Be + 4 mm Al
M50	1.12	29	50	1 mm Be+ 1.07 mm Al
NS40	1.09	33	40	1 mm Be + 0.21 mm Cu
M60	1.06	34	60	1 mm Be + 1.56 mm Al
S60	1	38	60	3 mm Be + 4.35 mm Al
S75	1.03	39	75	1 mm Be + 1.5 mm Al
RQR6 (IEC)	1	44	80	2.5 mm Al
NS60	0.97	48	60	4 mm Al + 0.6 mm Cu
M100	1	51	100	3 mm Be + 5 mm Al
RQR9 (IEC)	1.03	54	120	2.5 mm Al
NS80	1.12	65	80	4 mm Al + 2 mm Cu
M150	1.25	70	150	3 mm Be + 5 mm Al + 0.25 mm Cu
NS100	1.37	83	100	4 mm Al + 5 mm Cu
CT120-Al (Landauer)	1.54	90	120	Unknown
NS120	1.75	100	120	4mm Al + 5mm Cu
H150	2.08	117	150	3 mm Be + 4 mm Al + 4 mm Cu + 1.51 mm Sn
NS150	2.08	118	150	4 mm Al + 2.5 mm Sn

Table 7. Description of NIST-standard x-ray sources along with nanodot correction factors supplied from Yahnke et al. [17].

Since these data describe the response of the nanodot dosimeters to specific continuous spectra unlike the spectrum of discrete lines from ^{241}Am, it is not immediately obvious how they can applied to the ^{241}Am spectrum to yield the most accurate dose measurement. Several methods were considered and the data generated using these methods were compared to the data gathered with the ion chamber for many photon fields. The sections below include a description of these methods. The correlation among the dose measurements yielded by these methods and the data gathered with the ion chamber is also discussed.

3.3.3.2.2 Determination of Correction Factors Based on NIST Standards

The data reported in Section 3.3.3.2.1 can be used to determine correction factors for adjusting dose measured by a nanodot dosimeter based on the photon energy spectrum of the radiation field being measured. Since the data provided in Section 3.3.3.2.1 are not for discrete sources, several methods of using these data in order to determine the correction factor for the ^{241}Am sources were considered. These methods are outlined in the sections below.

3.3.3.2.2.1 Mean Energy Method

Every x-ray spectrum described by the NIST standard codes above has a mean energy which is reported by NIST [20]. Since many x-ray spectra have similarly-shaped energy distributions, one method to determine a correction factor for a given energy spectrum is to match its mean energy to the mean energy of a NIST standard x-ray spectrum used to calibrate the Landauer dot dosimeters. The mean energy of the x-ray spectrum in question can be calculated using the method of Poludnioski and Evans [18,19], who use a theoretical approach to produce x-ray spectra which closely match experimental spectra as discussed above in Section 3.3.2.1.1.

In the case that there is no NIST standard with a mean energy that closely matches the spectrum in question, an interpolation was generated for the correction factors based on the mean energies of all of the NIST x-ray spectra. This interpolation was found using with Mathematica. It is shown in Figure 13.

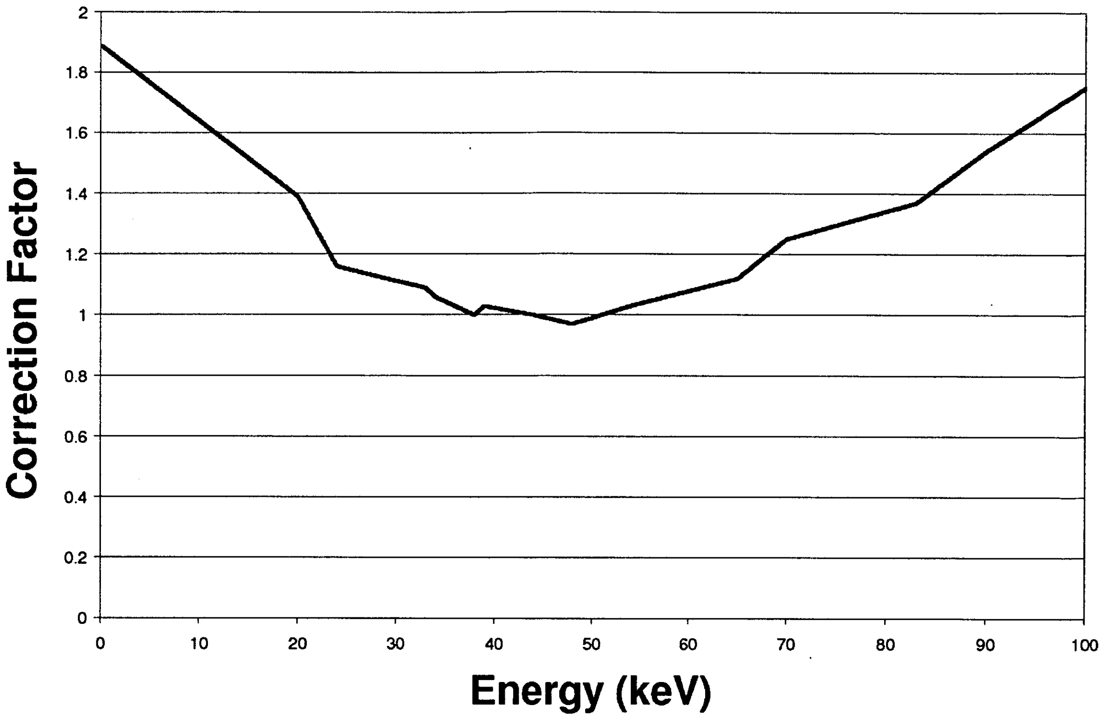

Figure 13. Interpolation of correction factors reported by Yahnke et al. [17] for the mean energies of the standard spectra used to measure the energy response of the nanodots.

In this figure note that the dose response decreases below 40 keV and above 60 keV. For the x-ray machine dosimetry data gathered using the nanodot dosimeters and reported below, the mean energy correction method has been used to calculate correction factors. Using the mean energy of the measured x-ray spectrum calculated with SpecCalc program, the correction factor is calculated from the interpolated function mentioned above. These factors are reported along with the factors calculated by other methods below.

For the ^{241}Am dosimetry data gathered using the nanodot dosimeters, the energy spectrum (as reported in Chapter 2) is different from a continuous x-ray spectrum having large numbers of photons at the lower range of the spectrum (10-26 keV) and large numbers at 60 keV. The mean energy can be calculated for the photon spectrum emitted by an unshielded ^{241}Am foil; however, a bremsstrahlung spectrum with this mean energy has a different energy distribution.

The correction factors for the mean energies of the ^{241}Am spectra reported above have been calculated, however, since much of the information about the ^{241}Am spectrum is lost by only considering the mean energy, this method likely produces inaccurate correction factors. For this reason, a method of calculating the correction factors based on the mean energies of the two groups of photons (10-26 keV and 60 keV) was also considered.

3.3.3.2.2.2 Grouped Mean Energy Method

For the spectrum of ^{241}Am which has an energy distribution more bimodal than the typical x-ray bremsstrahlung spectrum, correction factors were calculated using a fluence weighting of the correction factor for mean energy of the photons in the lower range (10-26 keV) and the correction factor for 60 keV.

The mean photon energy in the lower range (10-26 keV) was first calculated. The correction factor for this energy was then found using the interpolation function shown above in Figure 13. The fraction of photons in the lower range was then found and multiplied by this correction factor. This number was then added with the fraction of photons at 60 keV multiplied by the correction factor for 60 keV photons. These correction factors are reported below in Table 10 for several ^{241}Am shielding configuraitons. These factors are compared with those produced by other methods in Section 3.3.3.6 below.

3.3.3.2.2.3 Total Spectrum Weighting

In order to convey the most information about the spectrum under consideration, an alternate method of calculating correction factors was developed by generating a correction factor weighted by the entire photon energy spectrum. In order to do this, a probability distribution was generated from the spectrum in question, with the sum total of this distribution equal to one. This probability distribution was multiplied by a correction factor function based only on narrow spectrum NIST standards (coded NS in Table 7) over the entire range of the spectrum in question.

By using only the NIST standards with the narrowest spectra due to filtration, it was possible to exclude data for which the presence of outlier photons could influence the correction factor function. For example the NS60 spectrum, with a mean energy of 48 keV, has a narrower spectrum than the M60 spectrum with a mean energy of 34 keV. The narrow spectrum standards were included since they are the closest approximation of the discrete lines of the ^{241}Am spectrum.

These correction factors were also calculated for the x-ray spectra generated by the RT250 recreated by the SpecCalc program. These data are presented in Table 9 and Figure 15 below.

3.3.3.2.2.4 Full Spectrum Weighting with Estimate of the Underlying Energy Dependence of Nanodot Dosimeters

Spectra of the narrow spectrum NIST standards are at best only approximations of monoenergetic sources. There must exist an underlying dose response function for monoenergetic sources, which when weighted over an x-ray spectrum, narrow or otherwise, would yield the correction factors found experimentally by Yahnke et al. [12]. This function cannot be measured, since no standard sources exist with monoenergetic photons in this range. However the experimental data for the continuous spectra may be used to derive such an underlying dose response function with some uncertainty.

Suppose the existence of a dose response function, R(E), which when weighted over the NIST standard spectra data would yield the correction factors measured by Yanhke et al. This function describes the correction factor for a monoenergetic source of energy E. These standard spectra may be represented in matrix M(S,E) form with each spectrum probability distribution populating a row in the matrix. Multiplying this matrix M(S,E) by the dose response function would then yield a vector of the correction factors measured for each spectrum S.

$$M(S,E)\times R(E)=C(S) \tag{12}$$

This system of equations is underdetermined as stated; however, if it is assumed that the dose-response function is a linear interpolation between points corresponding to mean energies of each individual spectrum, this condition is removed and the problem may be solved using a non-linear least squares fitting method using the Levenberg-Marquardt method in MATLAB.

The Levenberg-Marquardt algorithm provides a numerical solution to a problem involving the minimization of a function. The primary application of the Levenberg-Marquardt algorithm is in least squares fitting: given a set n of empirical datum pairs of dependent and independent variables (x_i, y_i), optimize the parameters P of the model curve f(x, P) in order to minimize the sum of the squares of the deviations, S(P), as in Equation 13.

$$S(P)=\sum_{i=1}^{n}[y_i-f(x_i,P)]^2 \tag{13}$$

In each iteration of the algorithm, the parameter vector P is replaced by a new estimate, P + δ. To determine δ, the functions f(x_i, P + δ) are approximated by their linearizations as in Equation 14, in which J_i is the gradient of f(x,P) with respect to P as in Equation 15.

$$f(x_i,P+\delta)\approx f(x_i,P)+J_i\delta \tag{14}$$

$$J_i=\frac{\partial f(x_i,P)}{\partial P} \tag{15}$$

In this case, the parameters P are the correction factors R(E), y_i are the correction factors found by Yanhke et al. [17], and x_i is E, the photon energy.

The function R(E) was found and then multiplied by various energy spectra and used to determine correction factors. The correction factors determined using this method are reported below in Table 9.

3.3.3.3 Uncertainty Analysis

A method of minimizing the uncertainty of dose measurements obtained using the Landauer OSL dosimeters is described in Section 3.2.4. This method was used in gathering dose-rate data except where otherwise noted. Using the data collected with the methods described above, uncertainty due to calibration, and uncertainty due to the nanodot reader the overall measurement uncertainty can be computed.

Landauer reports the dose values reported by the nanodot dosimeters to within ± 6% for energy spectra with a mean energy within 10 keV of the mean energy of the 80 kVp calibration spectrum without the use of a calibration factor. With the use of a correction factor factor, this uncertainty is reduced; however, it is not apparent to what degree this error is reduced, since correction factors are reported by Landauer without uncertainty analysis [9]. Because of this, this ± 6% upper-bound is used as the uncertainty due to calibration.

Reader uncertainty is determined for a three nanodot measurement using the following method. For one nanodot of a three dot reading (R1 of R1, R2, R3) the standard deviation of the three initial readings (R1.1.1, R1.1.2, R1.1.3) is taken as the uncertainty for that reading ΔR1. The standard deviation of the three final readings (R1.2.1, R1.2.2, R1.2.3) is taken as the uncertainty for the final reading, ΔR1.2. The uncertainty for the dose reading reported by a single dosimeter is the uncertainties of these initial and final readings added in quadrature:

$$\Delta R1 = \sqrt{(\Delta R1.1)^2 + (\Delta R1.2)^2} \tag{16}$$

For the total dose, which is the average of the dose readings from three dosimeters, the three dose readings R1, R2, and R3 are averaged, so the final uncertainty in this dose reading due to reader uncertainty is then:

$$\Delta R = \sqrt{\left(\frac{\Delta R1}{3}\right)^2 + \left(\frac{\Delta R2}{3}\right)^2 + \left(\frac{\Delta R3}{3}\right)^2} \tag{17}$$

So for the final dose reading:

$$D = C \times R \tag{18}$$

Where D is the dose, C is the calibration correction factor, and R is the dose reading. The uncertainty for this quantity is then defined as:

$$\Delta D = \sqrt{(C\Delta R)^2 + (R\Delta C)^2} \tag{19}$$

Equation 19 has been used to define the uncertainty of the dose measurements obtained with the Landauer OSL dosimeters unless otherwise noted. In cases where only a single OSL measurement was made, the reading uncertainty is calculated as above for a single reading, R1. This uncertainty is taken as the reading uncertainty to yield:

$$\Delta D = \sqrt{(C\Delta R1)^2 + (R1\Delta C)^2} \tag{20}$$

3.3.3.4 Measuring Bremsstrahlung Spectra from 75-250 kVp

In order to check the consistency of the dose measurements provided by the ion chamber and the OSL dosimeters, dose-rates were measured for the same x-ray fields measured above. Nanodots were placed on a polyethylene platform 2 cm thick and placed at the center of the beam of the RT250 x-ray tube. They were held at 36.4 cm FSD by a level jack stand. Dose-readings along with uncertainty from the reader as well as the calibration are included in Tables 8 and 9.

	0.1 mm Cu	+/-	0.2 mm Cu	+/-	0.35 mm Cu	+/-	0.5 mm Cu	+/-	1.0 mm Cu	+/-	0.4 Th	+/-
75 kVp	54.12	3.44	21.84	1.65	10.18	0.80	5.98	0.36	1.76	0.13	0.52	0.04
100 kVp	102.93	7.72	48.64	2.96	26.48	2.56	16.92	1.05	8.20	0.56	3.22	0.22
150 kVp	207.05	16.33	115.68	7.62	88.00	6.48	58.98	4.39	34.58	2.08	21.39	1.28
200 kVp	322.56	21.15	209.44	15.26	155.26	9.40	129.48	7.81	84.24	7.34	61.44	3.74
250 kVp	367.51	25.70	267.99	21.14	218.47	15.44	192.53	13.56	136.87	9.34	106.75	7.49

Table 8. Dose rate data in cGy/min obtained with the Landauer OSL dosimeters using the mean energy correction method.

	0.1 mm Cu	+/-	0.2 mm Cu	+/-	0.35 mm Cu	+/-	0.5 mm Cu	+/-	1.0 mm Cu	+/-	0.4 Th	+/-
75 kVp	56.54	3.60	23.40	1.77	10.58	0.84	6.15	0.37	1.80	0.13	0.53	0.04
100 kVp	116.31	8.72	53.31	3.25	28.44	2.75	18.15	1.13	8.40	0.57	3.27	0.23
150 kVp	257.88	20.34	139.41	9.19	101.16	7.44	68.06	5.07	39.52	2.38	22.73	1.37
200 kVp	401.92	26.35	263.44	19.19	190.65	11.54	151.81	9.15	96.28	8.39	60.16	3.66
250 kVp	469.74	32.85	332.61	26.23	252.08	17.82	213.41	15.02	138.31	9.44	102.16	7.17

Table 9. Dose rate data in cGy/min obtained with the Landauer OSL dosimeters using the total spectrum weighting correction method.

3.3.3.5 Dosimetry for ^{241}Am with Various Shielding Configurations

Although the dose response of Landauer nanodots has been characterized for fields as low in energy as 20 kV x-ray spectra, they have not been characterized for isotope spectra with discrete photon peaks in the low-energy range. For this reason, there is uncertainty associated with any correction factor applied for low-energy photons.

To characterize any uncertainty involved in this process, the dose-rate delivered by ^{241}Am with several shielding configurations was measured. Each of these shielding configurations yields a different low-energy photon spectrum. It is necessary to arrive at a verifiable method for measuring dose delivered by such different configurations in order to reliably and accurately measure the dose-rate delivered by these configurations for biological applications.

The same shielding configurations described above in the ion chamber dosimetry section were considered with the nanodot dosimeters. Since the size of the nanodots is small compared to the active volume of the ion chamber, the dots were elevated 1 cm above the shielding in question for all data gathered. These data are reported below in Table 11 along with uncertainty due to reader error and calibration accuracy in the section comparing low dose-rate dosimetry.

3.3.3.6 Comparison of Dosimetry Data and Various Correction Methods

In this section all dosimetry data measured with the ion chamber and OSL dosimeters are consolidated and corrected using the various methods proposed above. Consistencies and contradictions are described that aid in the determination of which method of correction provides the most accurate dose data. Conclusions of which methods should be used to provide the most accurate dose data for the dosimetry of ^{241}Am foils are made.

3.3.3.6.1 Comparison of Dose Data for Bremsstrahlung Spectra

For the bremsstrahlung x-ray spectra, there is no need to apply a correction factor for the dose data measured using the Radcal ion chamber, since it has a constant energy response across this energy range which has been measured [13]. For the nanodot OSL dosimeters, the energy response function is not constant over the energy range of the photons produced by the RT250 x-ray tube. The application of correction factors found using the mean energy and total spectrum weighting methods were considered. These data are shown above in Tables 7 and 8.

From these data it is possible generate dose vs. potential curves for all the filtration settings. Two sets of curves are shown in Figures 14 and 15, corresponding to the curves generated with the mean energy correction method and the total spectrum weighting method, respectively.

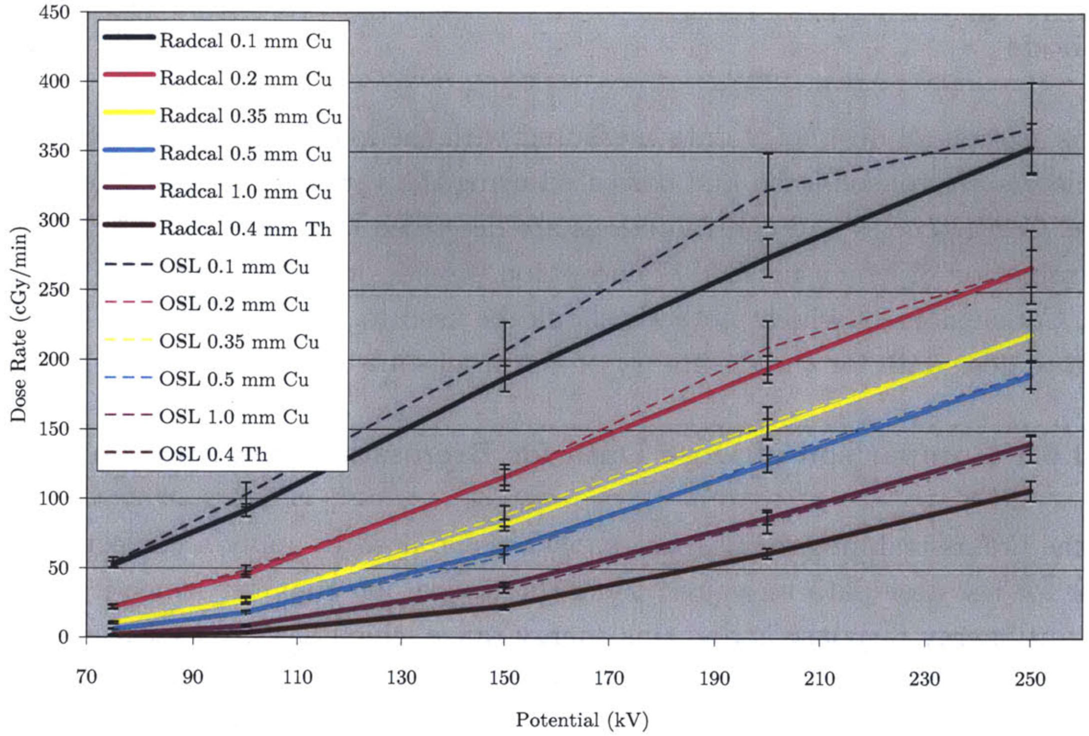

Figure 14. OSL dosimeter measurements corrected with the mean energy method compared with ion chamber data.

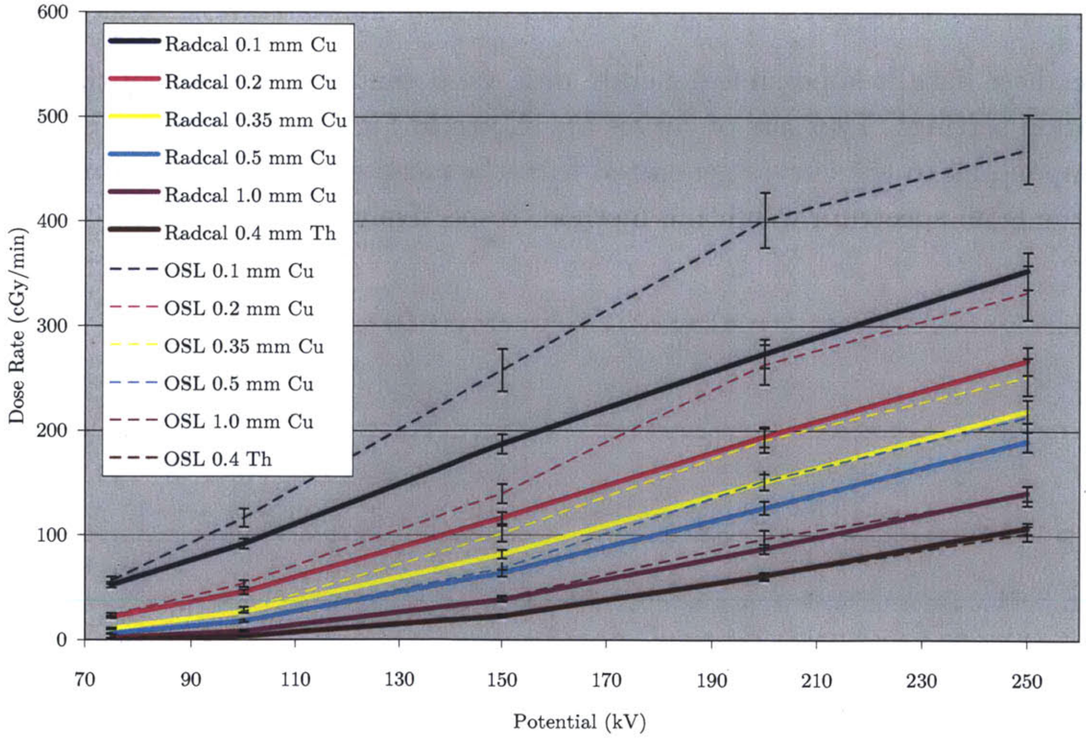

Figure 15. OSL dosimeter measurements corrected with the total spectrum

weighting method compared with ion chamber data.

From these data, note that the mean energy method of correcting the nanodot dose measurements provides better agreement with the ion chamber measurements. In the case of bremsstrahlung spectra for which the overall shape of the energy spectrum is similar for a given mean energy, the mean energy method would logically provide a good correction with some error due differences in the energy distribution between the standard spectrum referenced and the RT250 spectrum delivering the dose.

Good agreement is shown for the ion chamber measurements and the OSL measurements corrected with this mean energy method, which is the method suggested Landauer for use with bremsstrahlung spectra. From these data, it is concluded that the OSL dosimeters are capable of accurately measuring dose across a wide range of tube potentials (75 kV-250 kV) with a variety of filters.

3.3.4 Comparison of Dose Data for ^{241}Am Spectra

Measurements of the dose from ^{241}Am foils must be corrected for the energy dependence of the dosimeter for both the ion chamber and OSL dosimeters described above. The correction methods outlined above in Sections 3.2.2 and 3.3.2 describe these methods in detail. Shown below in Table 9 are the data for four different shielding configurations with each correction method applied. From these data, agreement is shown for the corrected ion chamber data and the OSL data corrected with the total spectrum weighting method and the weighting with the estimate of the underlying energy dependence. It is concluded that the dose data gathered with the OSL dosimeters yields an accurate representation of the dose delivered by the ^{241}Am foils for a variety of shielding configurations when corrected properly. Since the weighting with the estimate of the underlying energy dependence yield very similar results, and the error of the total spectrum weighting method is more easily quantifiable, the total spectrum weighting method was selected for gathering dose data for the ^{241}Am foils in further experiments. The overall method of gathering the most accurate dose data with ^{241}Am foils with various shielding configurations is described in the section below.

	No Shielding			1mm LDPE			0.254 mm Al			0.5 cm Al		
	Correction Factor (CF)	Dose rate	+/-	CF	Dose rate	+/-	CF	Dose rate	+/-	CF	Dose rate	+/-
Ion Chamber Uncorrected		1.96	0.01		1.55	0.04		0.82	0.01		0.11	0.01
Ion Chamber Corrected	1.04	**2.04**	**0.10**	1.06	**1.65**	**0.05**	1.02	**0.83**	**0.04**	1.03	**0.11**	**0.01**
OSL Uncorrected		1.68	0.10		1.40	0.03		0.77	0.02		0.11	0.01
OSL Grouped Mean Energy Correction	1.22	2.05	0.13	1.24	1.73	0.09	1.19	0.91	0.06	1.12	0.12	0.01
OSL Narrow Spectrum Correction	1.20	**2.01**	**0.12**	1.22	**1.71**	**0.09**	1.16	**0.90**	**0.06**	1.06	**0.12**	**0.01**
OSL Underying Efficiency Correction	1.19	2.00	0.12	1.22	1.71	0.09	1.16	0.89	0.06	1.05	0.12	0.01

Table 10. Correction factors and dose data found using several efficiency correction methods (bold face added to highlight agreement between the ion chamber data and the nanodot data obtained using an estimate of the underlying efficiency function described in 3.3.3.2.2.4.)

3.3.5 Method for Dosimetry of Various Low-energy Photon Fields Using OSL Detectors

Using the conclusions presented above, a method was developed for obtaining the best estimate of the dose delivered by low-energy photons using the Landauer OSL dosimeters. Reader uncertainty is minimized using the techniques presented in Section 3.3.3.1 and calibration uncertainty is minimized using the correction method presented in Section 3.3.3.2.2.4. Here this method is recreated in a concise step-by-step procedure.

First nanodots are annealed such that they read a level of dose less than 0.01 cGy when read using the Microstar reader. Three annealed dots are then read three times each and placed on the radiation source in question. The exposure time is timed precisely.

After exposure, the dosimeters are read three times using the Microstar reader. For each dosimeter, an average of the three reads before and after exposure are computed. The average residual dose found before exposure is subtracted from the final dose reading. The standard deviations of these two dose readings are then added to find the error for the single dot measurement. The averages of the three dosimeters are then averaged to yield the uncorrected dose reading. The reader error is also estimated using the error estimates for each dosimeter. This method reduces the reader error to a minimum level as established in Section 3.2.4.

This uncorrected dose reading is then divided by the exposure time to yield the dose rate. The reader uncertainty is also divided by the exposure time to yield the reader undertainty in the dose-rate.

This dose-rate is then multiplied by a correction factor found using the spectrum weighting method established in Section 3.3.3.2.2.4. A probability density function is computed for the spectrum of the field being measured. This PDF is then multiplied by dose response function computed by the optimization method described in Section 3.3.3.2.2.4. The result is a fluence weighted correction factor that is multiplied by the uncorrected dose-rate and reader error to provide the best estimate of the true dose-rate that minimizes the calibration error. The calibration error is then limited to within 6% quoted by Landauer for a field with a mean energy near that of the field used to calibrate the Microstar reader. This 6% is then an upper bound on the calibration error. The total uncertainty can be computed by computing the reader error and this 6% calibration error using the formula established in Section 3.3.3.3.

This method provides the best estimate of the dose-rate and uncertainty of the dose delivered by ^{241}Am foils with any shielding configuration. This method is used in Chapter 4 to compute dose-rate for a series of shielding configurations that have applicability in biological irradiators.

3.4 Dosimetry for Several Shielding Configurations with ^{241}Am Sources

In order to design biological irradiators with various dose-rates and energy spectra, a method was developed for measuring the dose-rate delivered for a variety of photon fields. This method was used to measure the dose-rate for the ^{241}Am foils with several shielding configurations. The table below provides dose-rate data for shielding configurations described by the spectra in Chapter 2. For all these data, three dots were placed in a Petri dish directly above the shielding which was placed directly above an ^{241}Am foil. Dots were read according the data was processed using the procedure outlined above in Section 3.3.5.

Shielding Configuration	Dose-rate (cGy/h)	
Unshielded Am foil	1.97	0.12
0.00254 cm Cu	0.52	0.03
0.00508 cm Cu	0.33	0.02
0.5 cm Al	0.12	0.01
0.0254 cm Al	0.94	0.06
0.3048 cm Al	0.14	0.01
0.05 cm Cu/0.5 cm al	7.37E-03	4.42E-04
3 cm Al	6.63E-03	3.98E-04
1 mm LDPE	1.71	0.10
2 mm LDPE	1.56	0.09
3 mm LDPE	1.40	0.08
4 mm LDPE	1.27	0.08
5 mm LDPE	1.19	0.07
6 mm LDPE	1.12	0.07
7 mm LDPE	0.97	0.06
8 mm LDPE	0.89	0.05
9 mm LDPE	0.82	0.05
10 mm LDPE	0.73	0.04

Table 11. Dose-rate data for the ^{241}Am foils with various shielding configurations.

3.5 Conclusion

Using the methods of spectroscopy described in Chatper 2, a method of dosimetry has been established for the low energy photons emitted by the ^{241}Am foil sources. With knowledge of the photon energy spectrum emitted the Philips RT250 x-ray tube and by several shielding configurations with ^{241}Am foils, a method of correcting dose measurements for dosimeter energy response was presented. This method produced agreement for the dose data measured with two dosimeters. These results will be used in Chapter 4 to analyze the biological effectiveness of the low energy photons emitted by the ^{241}Am foil sources.

3.6 References

1. R. Colle and B.E. Zimmerman, Applied Radiation and Isotopes, 56, 2002, 223-230.
2. R. Colle, P. Volkovitsky, L. Laureano-Perez, "A Primary Standardizatino of ^{55}Fe by Isothermal Microcalorimetry", Presented to the Comparisons and Uncertainties Workshop, Bureau International des Poids et Mesures, Sevres, France Sept. 18, 2008.
3. F.H. Attix, Introduction to Radiological Physics and Radiation Dosimetry (John Wiley, New York, 1986).
4. J. R. Greening, Fundamentals of Radiation Dosimetry, Adam Hilger Ltd., Bristol, England.
5. M. J. Butson, P. K. N. Yu, T. Cheung, P. Metcalfe, Materials Science and Engineering Reports, 41, 2003, 61-120.
6. Sayeg, Coffey, McLaughlin, Med. Phys., 17, 1990, 521.
7. S. Devic, J. Seuntjens, G. Hegyi, E. B. Podgorsak, C. G. Soares, A.S. Kirov, I. Ali, J.F. Williamson, and A Elizondo, Med. Phys. 31, 4, 2004, 2393-2401.
8. L. K. Wagner, B. R. Archer, F. Cerra, Med. Phys. 17, 6, 1990, 989-997
9. M.J. Berger, J.S. Coursey, M.A. Zucker, and J. Chang, "Stopping-power and Range Tables for Electrons, Protons, and Helium Ions", NISTIR 4999, 2005, NIST.
10. Ion chamber specifications, Radcal, Inc., http://www.radcal.com/10x6series.html
11. Ethan MacIntosh, Radcal Technical Support, personal communication, January 12, 2010.
12. S. W. S. McKeever, Nuclear Instruments and Methods in Physics Research B, 184, 2001, 29-54.
13. M.S. Akselrod and S. W. S. McKeever, Radiation Protection Dosimetry, 81,3, 1999, 167-176.
14. Zamburlini, Guyn, Pejovic-Milic, Prestwich, Chettle, X-ray Spectrometry, 36, 2 (2007), 76-81.
15. J.H. Hubbell and S.M. Seltzer, Tables of X-Ray Mass Attenuation Coefficients and Mass Energy-Absorption Coefficients, NISTIR 5632, National Institute of Standards and Technology.

16. R. Gaza, E. G. Yukihara, S. W. S. McKeever, O. Avila, A. Buenfil, I. Gamboa-deBuen, M. Rodriguez-Vallafuerte, C. Ruiz-Trejo, and M. Brandan, Radiation Protection Dosimetry, 2006, 119, 1-4, 375-379.
17. C.J. Yahnke, R.D. Hanify, and Mr. Salasky, "Microstar Calibration Conversion Factors for DOTs", Landauer Inc.
18. G. G. Poludniowski, Med. Phys. 34, 6, 2007 2175-2186.
19. G. G. Poludniowski and P. M. Evans, Calculation of x-ray spectra emerging from an x-ray tube. Part I. Electron penetration characteristics in x-ray targets. Medical Physics, 34, 6, 2007 2164-74.
20. Ionizing Radiation Division, Calibration of X-ray Radiation Detectors, NIST, IRD-P-03.

Chapter 4: Tissue Culture Irradiators for Determination of Relative Biological Effectiveness of Low Dose-rate Low-energy Photon Radiation

4.1 Introduction

The biological impact of ionizing photon radiation has been observed to vary with photon energy. This variation in impact has been quantified in terms of relative biological effectiveness (RBE) defined as the ratio of the doses of two radiation fields which produce the same biological result.

As discussed in Chapter 1, several studies have focused on the RBE of low energy photons in acute delivery of approximately 1 Gy/min. However no experimental studies to date have reported RBE data for low-energy photons at dose-rates in the 0.1-1 cGy/h range. In this chapter, tissue culture irradiators for the measurement of RBE of low-energy photons (10-60 keV) in this dose-rate range are described. Biological data demonstrating differences in biological effectiveness with these irradiators are also presented. These data are compared with the model of RBE reported by Brenner et al. [1].

4.2 Modeling of Relative Biological Effectiveness at Low Dose-rates

Although no experimental data exist to provide an estimate of RBE of low-energy photons (10-60 keV) for chronic exposure at low dose-rates (0.1-10 cGy/h), several studies have reported experimental measurements of RBE for a wide variety of end points and radiation fields [7]. Brenner et al. have developed a model [1] incorporating experimental RBE observations for photons, taking into account the dose-rate, timing, and energy spectrum of the photon field. Kellerer has also proposed a model [2] which predicts RBE based on the secondary electron spectrum produced by a photon field. In the following sections, these models are described and used to estimate RBE differences for different photon spectra produced by ^{241}Am foil sources.

4.2.1 Previous Work in Modeling Relative Biological Effectiveness

In the model presented by Brenner et al. RBE is given as a function of the dose of the radiation field with the greater biological impact D_H. RBE is also dependent on the terms of the linear quadratic model description of the radiation fields considered.

The linear quadratic model is a model of cell survival based on fitting experimental data to an equation with two parameters, a linear term α, which quantifies the degree of irreparable damage, and a quadratic term β, which quantifies the degree of damage which can be repaired. The equation to which experimental data are fitted is given in Equation 1 where SF(D) indicates the surviving fraction for a dose, D:

$$SF(D) = e^{-\alpha D - \beta D^2} \tag{1}$$

This model of RBE is described by Equation 2. In this model, α_H and β_H are the linear and quadratic parameters for the field with the greater biological impact, and α_L and β_L are the linear and quadratic parameters for the field with the lesser biological impact. The G factor incorporates the effects of dose-rate and dose timing and is described in Equation 3.

$$RBE(D_H) = \frac{\alpha_L}{2\beta_L G D_H}\left[\sqrt{1 + \frac{4G\beta_L}{\alpha_L}\left(\frac{\alpha_H}{\alpha_L}D_H + \frac{G\beta_L}{\alpha_L}D_H^2\right)} - 1\right] \tag{2}$$

$$G = \left(\frac{2T_{1/2}^2}{\ln(2)T^2}\right)\left(e^{-\frac{\ln(2)T}{T_{1/2}}} - 1 + \frac{\ln(2)T}{T_{1/2}}\right) \tag{3}$$

In Equation 3, $T_{1/2}$ represents the half-life of reparable DNA damage and T represents the time of exposure. Brenner et al. quote 15 minutes as an approximation for $T_{1/2}$ in their work [1], and it is used in the sections below to calculate RBE.

The α terms for the photon fields represent the probability of irreparable damage, while the β terms represent the probability of damage that is repaired. These factors may be measured experimentally or calculated based on knowledge of the lineal energy transfer due to the photon field in question. The lineal energy transfer is the microscopic equivalent of the more familiar linear energy transfer. Zaider and Brenner [3] show that α can be estimated using Equation 4.

$$\alpha = \int w(y)d(y)dy \tag{4}$$

where w(y) is an endpoint-specific weighting factor which describes the response of a particular endpoint to the lineal energy transfer y and d(y) is the normalized distribution of dose per unit lineal energy transfer. This weighting factor w(y) can be estimated based on the quality factor as a function of lineal energy transfer as reported by the International Commission on Radiation Units and Measurements (ICRU) [4].

This normalized distribution of dose in lineal energy is calculated based on measured values of the distribution of lineal energy for a particular photon energy E, as reported by Kliauga and Dvorak [5]. Because these distributions of lineal energy known for several photon energies, they are used to calculate the normalized total distribution of dose per unit lineal energy transfer using Equation 5 [2].

$$d(y) = \frac{\int E\,N(E)\,d(y;E)\mu_{en}(E)/\rho\,dE}{\int E\,N(E)\,\mu_{en}(E)/\rho\,dE} \tag{5}$$

In this equation, E denotes the photon energy, N(E) denotes the fluence of photons of the energy E, $\mu_{en}(E)/\rho$ denotes the mass-absorption coefficient for energy E, and d(y; E) denotes the distribution of dose per lineal energy transfer for the photon energy E.

By combining Equation 4 with Equation 1, α may be described by Equation 6.

$$\alpha = \frac{\int w(y) \int E\,N(E)\,d(y;E)\mu_{en}(E)/\rho\,dE\,dy}{\int E\,N(E)\,\mu_{en}(E)/\rho\,dE} \tag{6}$$

Kliauga and Dvorak have reported distributions of dose per unit lineal energy transfer for photons of 12, 25, and 60 keV. Although experimental data for all points between do not exist, an interpolation for the estimation of d(y;E) for the energies between can be calculated. Using an interpolation of d(y;E) and integrating over y to yield d(E), dependence on lineal energy transfer can be eliminated, and α can be written in terms of energy only as in Equation 7.

$$\alpha = \frac{\int EN(E)d(E)\mu_{en}(E)/\rho dE}{\int EN(E)\mu_{en}(E)/\rho dE} \tag{7}$$

This α quantity can be calculated for any photon energy spectrum. These α factors may then be combined with timing of the dose in order to determine RBE. For long term irradiation, there is reduced dependence on β terms since these terms represent reparable damage which is likely repaired over a long term irradiation. The dependence on total dose of the highest RBE radiation (D_H) is also reduced. RBE is then most dependent on α for these long-term irradiations. This dependence can be shown by plotting the dependence of RBE with the α, β, and D_H factors for a one-week long irradiation (604800 seconds). Dependence on these various factors is illustrated in Figures 1-5.

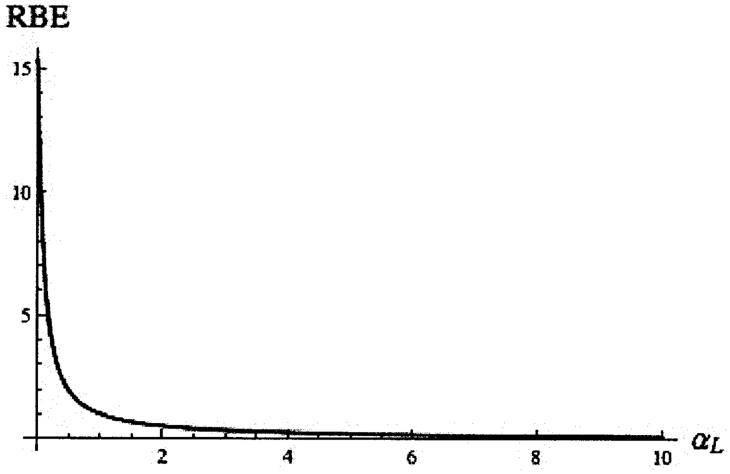

Figure 1. RBE for various values of α_L. All other factors held equal to 1.

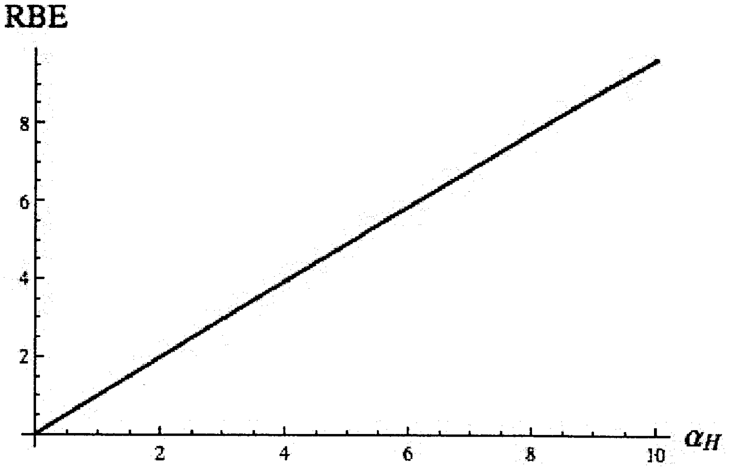

Figure 2. RBE for various values of α_H. All other factors held equal to 1.

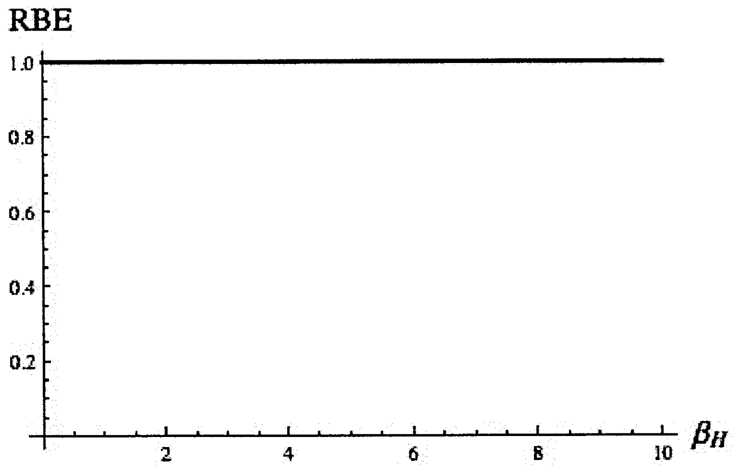

Figure 3. RBE for various values of β_H. All other factors held equal to 1.

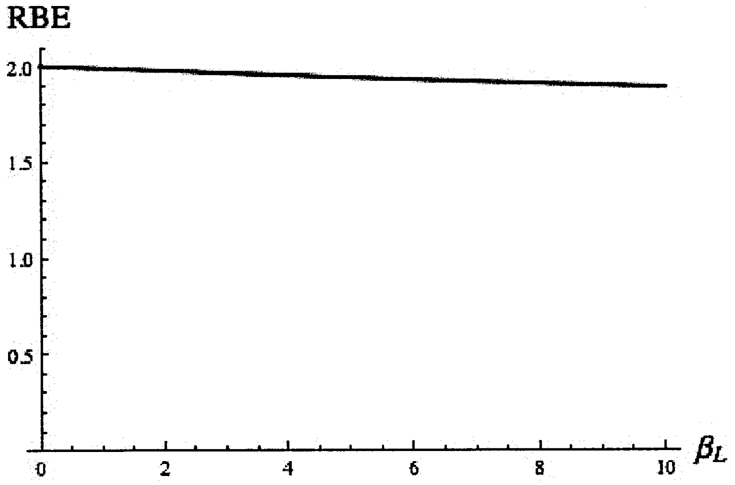

Figure 4. RBE for various values of β_L. All other factors held equal to 1 except, α_H=2.

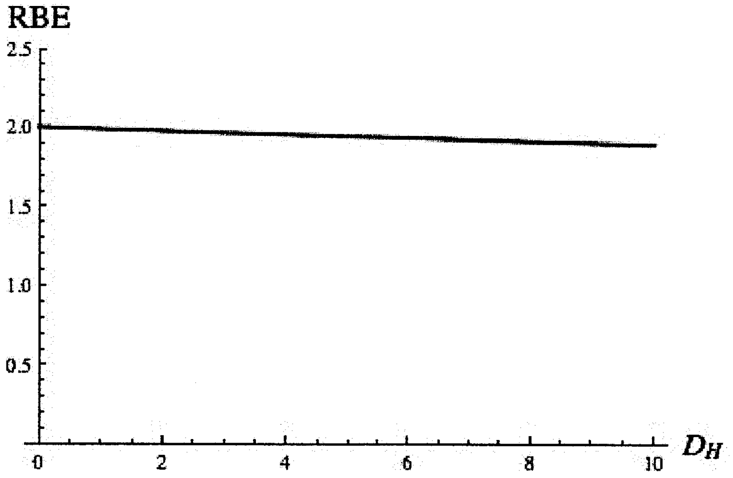

Figure 5. RBE for various values of D_H. All other factors held equal to 1, except α_H=2.

From these figures, note that the linear terms, α_L and β_L, have the most significant impact on RBE in this model. By calculating α values using the method above, it is then possible to estimate the RBE between two photon spectra. RBE is estimated in Section 4.2.2 using this method.

Kellerer discusses the relationship between photon energy and biological effectiveness in terms of the linear energy transfer and range of the secondary electron spectrum produced by these photons [2]. The linear energy transfer quantity determines the proximity of energy deposition events within a cell. Greater linear energy transfer indicates that more energy is deposited per unit length within a cell.

The range of these secondary electrons is also incorporated into the model for the purpose of modeling increased biological impact for secondary electrons with a range great enough to traverse an entire cell nucleus over electrons with lesser range. This range effect was considered based on the possibility that damage to two chromosomes within a single nucleus during a short period of time could potentially have more biological impact than damage to a single chromosome alone or damage to two chromosomes with a long delay between events.

Kellerer defines the biological response to a photon field R based on the biological response r(E) for secondary electrons of energy E and the number of electrons of energy at least equal to E, N(E), as described in Equation 8.

$$R = \int r(E)N(E)dE \tag{8}$$

The biological response, r(E), for a secondary electron of energy E is defined based on the LET of electrons in tissue LET(E) and a factor c which describes the dependence of this response on the range of the secondary electron. In order to consider the possible increase in biological effectiveness of 10-20 keV electrons, with range approximately equal to the diameter of a cell nucleus, an increase in the biological response function is introduced using a Gaussian centered at 15 keV. The reasoning for this range effect is that 10-20 keV may be deposited entirely within the cell nucleus, while electrons with greater energy and greater range will deposit less energy within the confined volume of the cell nucleus. Electrons of lower energy would deposit their energy more locally without the ability to damage multiple chromosomes. For c=0, range does not effect this response function. Kellerer examines values of this c parameter from 0-100 to study a wide range of range dependence. This biological response is described in Equation 9.

$$r(E) = LET(E)\left[1 + ce^{-\frac{(x-15)^2}{8}}\right] \tag{9}$$

Kellerer uses this response function to compare the biological effectiveness of a 30 kVp x-ray spectrum with a 200 kVp photon spectrum. Kellerer calculates the primary electron spectra for the 30 kVp and 220 kVp photon spectra by using the interaction coefficient data available from NIST [3]. For every incoming photon energy, Compton electrons and photoelectrons are added to the primary electron spectrum in proportion to the interaction coefficients.

The Compton electron spectrum for an incoming photon of energy hν can be calculated using the method of Evans [4], which relates the incoming photon frequency ν with the outgoing electron energy T, the difference in direction of the incoming and outgoing photons θ, the difference in direction of the incoming photon and the outgoing electron ϕ, and the quantity $\alpha = h\nu_0/m_e c^2$. For this quantity, h is Planck's constant, m_e is the rest mass of an electron, and c is the speed of light. The relation between the angles θ and ϕ is given by Equation 11.

$$\frac{d\sigma_e}{dT}=\frac{r_o^{\,2}}{2}\left(\frac{\nu'}{\nu_0}\right)^2\left(\frac{\nu_0}{\nu'}+\frac{\nu'}{\nu_0}-\sin^2\theta\right)\frac{2\pi}{h\nu_0}\left(\frac{(1+\alpha)^2-\alpha^2\cos^2\phi}{(1+\alpha)^2-\alpha(2+\alpha)\cos^2\phi}\right) \tag{10}$$

$$\cot\phi=(1+\alpha)\frac{\tan\theta}{2} \tag{11}$$

In order to account for multiple scattering events as these primary electrons traverse a biological sample, Kellerer generates cumulative electron energy spectra, N(E), for the two photon spectra considered. These cumulative energy spectra display the number of electrons n(E) present in the electron spectra with energy greater than or equal to E. Kellerer argues that since an electron track with initial energy E contains an electron track with less energy, E-dE, the cumulative electron spectra should be used to determine RBE. Using these electron spectra, Kellerer finds a minimum RBE for the 30 kVp photons relative to the 200 kVp field of 1.24 for c=0 and a maximum RBE of 1.77 for c=100.

These values show that the model described above predicts RBE values greater than one between for these photon fields even without including the effects of electron range on biological response. Although this model does not incorporate the effects of dose-rate, it can be used be used to provide an estimate of the RBE of the photon fields emitted by ^{241}Am foils with different amounts of shielding. This model is applied to the ^{241}Am spectra in Section 4.2.2 below.

4.2.2 Modeling the Relative Biological Effectiveness for Photons Emitted by ^{241}Am Foil Sources

In this section the two models described above are used to determine RBE values for photon fields emitted by ^{241}Am with different shielding configurations. These RBE estimates are compared with experimental data in Section 4.5.2 below.

4.2.2.1 Estimating RBE Based on Photon Energy and Dose-rate

With a method of calculating α and RBE, and having established that dependence on β is minimal relative to the dependence on α over a range of possible β, RBE can be calculated for the photon spectra emitted by the ^{241}Am foils using the method proposed by Brenner et al. [1]. For several photon spectra, α values have been calculated using Equation 7 and are shown in Table 1.

α	Source
2.6	Am No shielding
2.1	29mm PE on Am
1.2	0.5cm Al on Am
1.2	26.34 keV
1.1	60 keV

Table 1. Values of α for various energy spectra.

These α values may be used for the calculation of RBE of the different ^{241}Am spectra using Equation 2. For example, the RBE for the 29 mm polyethylene shielded ^{241}Am relative to the 0.5 cm Al shielded ^{241}Am is 1.74. The uncertainty associated with this quantity is dependent on the accuracy of the model and its parameters. Uncertainty in the underlying quality factors, lineal energy transfer functions, and damage half-life all add uncertainty to this model.

Some understanding of the uncertainty in the model can be gained by comparing its predictions with experimental data. Brenner et al. predict an RBE of 1.6 for 20 kV photons relative to ^{60}Co photons, and the experimental data obtained by Bistrovic et al. indicate a RBE of 1.4 ± 0.07 for a similar 20 kV x-ray spectrum relative to ^{60}Co gamma photons [6]. However, since no experimental data exist to evaluate the model at low dose-rates, the RBE data calculated for the two ^{241}Am fields are considered to be only estimates.

4.2.2.2 Estimating RBE Based on the LET and Range of Electron Spectra

In order to estimate the RBE for the photon fields emitted by the ^{241}Am foils with different amounts of shielding using the method of Kellerer [2], it was first necessary to calculate the primary electron spectra for these fields. The primary electron spectra were recreated using this method along with the

Compton electron spectra described above by Equation 10. To produce these spectra, Compton electron spectra were generated for each of the peaks of ^{241}Am spectra and added in the appropriate fractions along with photoelectrons of energy equal to the incoming photons. For example, the Compton electron spectrum produced by 60 keV photons calculated using this method is shown in Figure 6.

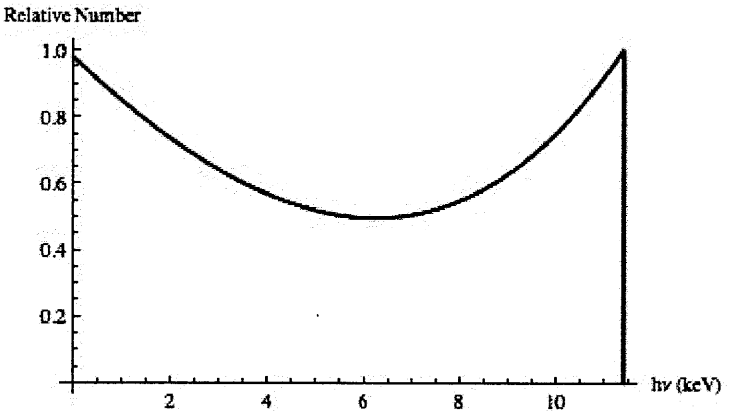

Figure 6. Compton electron spectrum produced by 60 keV photons.

Note from this figure that the maximum energy of these Compton electrons is 11.4 keV. For these Compton electrons, the range within tissue is less than 3.7 μm [5].

Electron spectra calculated for two shielding configurations, 0.5 cm Al and 29 mm polyethylene, are shown in Figure 7.

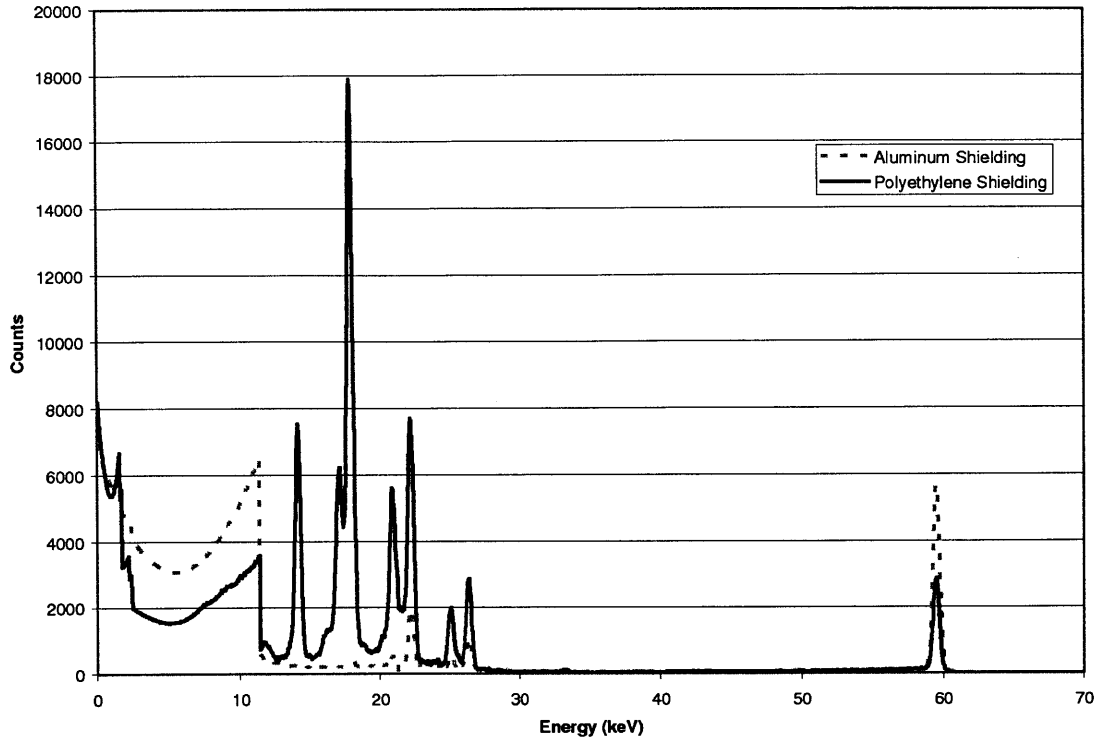

Figure 7. Primary electron spectrum for the ^{241}Am source configurations.

Note the differences between these spectra in the 10-30 keV range. The polyethylene shielding configuration produces significantly more electrons in this energy range than the aluminum shielding configuration.

The cumulative electron spectra, N(E), for these two ^{241}Am configurations are shown in Figure 8.

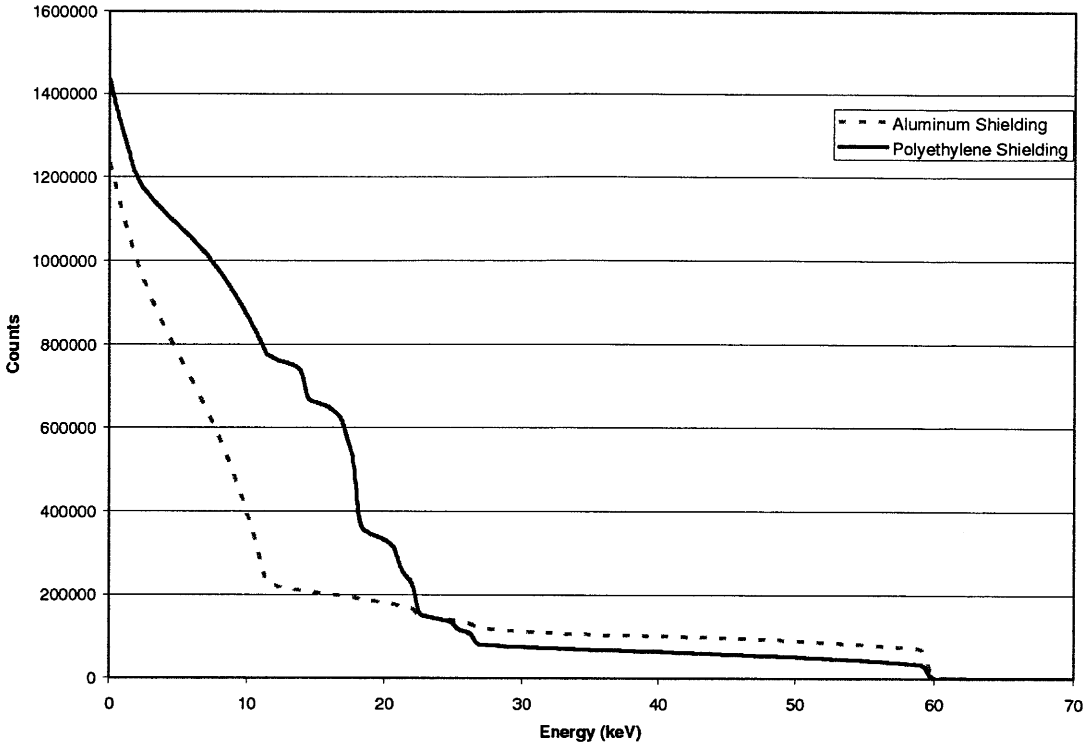

Figure 8. Cumulative electron spectra for two ^{241}Am source configurations.

In this figure, note the differences in these spectra at energies less than 20 keV. The polyethylene shielding configuration produces a greater number of electrons in this range than the aluminum shielding configuration.

For each of the two ^{241}Am photon spectra, biological response was calculated using the cumulative electron energy spectra and Equations 8 and 9. These biological effectiveness data were used to calculate RBE values, and these values are listed, along with the magnitude of the correction due to electron range, c, in Table 1.

c	RBE
0	0.94
5	1.05
10	1.23
20	1.27
100	1.75

Table 1. Average LET values for the electrons at the surface of the cell

monolayer.

Kellerer argues the primary electron spectrum is a good approximation of the electrons to which a biological sample is exposed as long as the sample is near the photon source. However, these electrons are not the only electrons produced when the photons from the ^{241}Am sources interact with the cell culture flask and cell monolayer. Since multiple scattering events occur, extensive computation must be used to determine the electron energy spectrum within a biological sample. An alternative to Kellerer's approximation is the method of simulating electron spectrum to which a cell monolayer is exposed.

These electrons produced by the ^{241}Am photons interacting within a tissue culture flask were modeled using MCNP. In this MCNP model, a cell monolayer 10 μm in thickness was positioned between a cell culture dish (1 mm thick) and a layer of cell culture medium (10 mm thick). This model is described in detail in Chapter 3. The flux of photons into the cell monolayer out of the tissue culture flask was modeled using the F1 tally.

In MCNP, an F1 tally calculates the number of particles crossing a surface as described in Equation 12, in which t represents time, E represents the energy of the particle, Ω represents the solid angle of a surface of area dA and a unit normal vector $\hat{n}$, n is the number of particles, and v is their velocity.

$$\mathrm{F1} = \int_{E_i} dE \int_{t_j} dt \int_{\Omega_{ki}} d\Omega \int dA \left| \hat{\Omega} \bullet \hat{n} \right| v\, n\left(\vec{r}, \hat{\Omega}, E\right) \qquad (12)$$

Tally results can be separated into bins corresponding to different energies, angles, and times. In these calculations, energy bins were 1 keV increments from 1 keV to 65 keV, and only angles with cosines between 0 and 1 were counted in order to calculate the flux of particles entering the monolayer of cells. Time was not binned in these calculations, since the source is not time-dependent.

The electron spectra tallied using MCNP for the two ^{241}Am source configurations are shown in Figure 9.

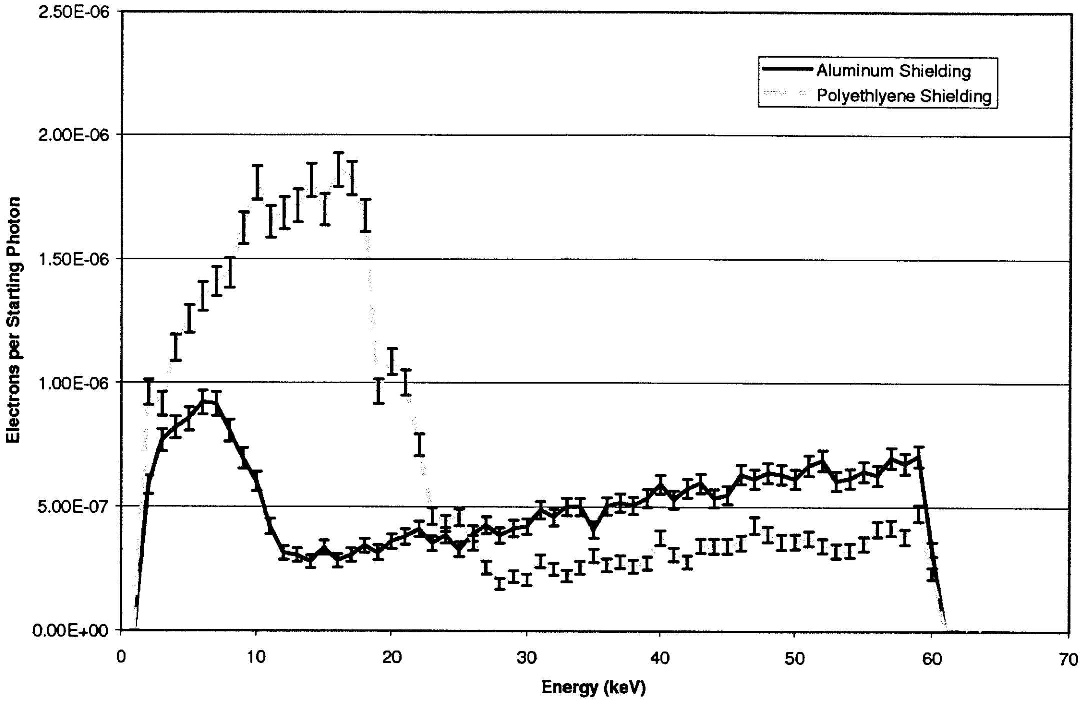

Figure 9. Electrons per starting photon entering the cell monolayer from the cell culture flask.

In this figure, note the greater presence of electrons within the 10-20 keV energy range for the polyethylene shielding configuration.

For these electrons produced by 60 keV electrons, the LET within tissue can be found in NIST data tables [5]. A plot of the LET within tissue for the photon energies in question is shown in Figure 10.

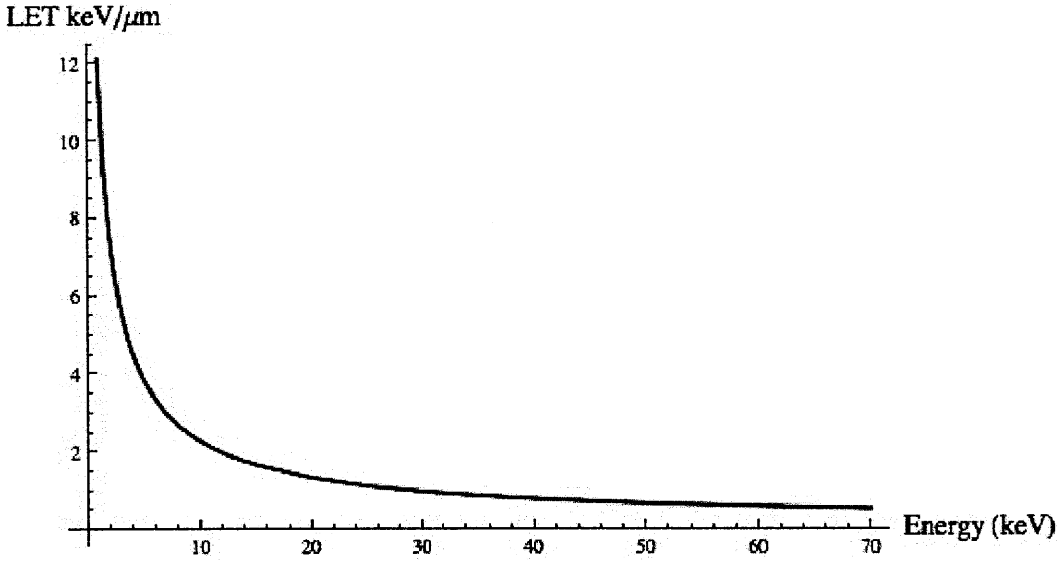

Figure 10. Linear energy transfer in tissue for electron energies 1-70 keV.

Note the non-linearity in LET in tissue. This figure illustrates the large difference in energy deposition density for the lower energy electrons relative to 60 keV electrons.

For each electron spectrum the average LET was found using Equation 13 in which E is the energy bin, F(E) is the frequency of electrons within energy bin E, and LET(E) is the LET for the energy E.

$$\langle LET \rangle = \frac{\sum_{E} LET(E) \times F(E)}{\sum_{E} F(E)} \qquad (13)$$

Uncertainty in this average LET quantity was calculated according Equation 14.

$$\Delta LET = \sqrt{\frac{\sum_{E} \left[LET(E) \times \Delta F(E) \right]^2}{\left(\sum_{E} F(E) \right)^2}} \qquad (14)$$

When these average LET quantities are compared, it can be seen that the average LET for the polyethylene shielding configuration is higher than that of the aluminum shielding configuration: the polyethylene shielding configuration, $\langle LET \rangle = 1.946 \pm 0.018$ keV/μm, and for the aluminum shielding configuration, $\langle LET \rangle = 1.541 \pm 0.019$ keV/μm.

In order to gain more information about the electrons traversing the cell monolayer, three more electron flux tallies were performed: the flux out of the monolayer and into the cell culture dish, the flux out of the monolayer and into the cell medium, and the flux out of the medium and into the monolayer. The electron spectra for these locations were all similar to that shown in Figure 9 and the average LET data are shown in Table 2.

Entering	Exiting	Aluminum		Polyethylene		Al to Polyethylene Ratio	+/-
		<LET> (keV/μm)	+/-	<LET> (keV/μm)	+/-		
Cell monolayer	Dish	1.561	0.019	1.946	0.018	0.802	0.012
Dish	Cell monolayer	1.773	0.024	2.161	0.023	0.820	0.014
Cell monolayer	Medium	1.971	0.034	2.360	0.045	0.835	0.021
Medium	Cell monolayer	1.561	0.019	1.840	0.019	0.848	0.013

Table 2. Average LET values for the electrons at the surface of the cell monolayer.

From these data, we see that the average LET is greater for the polyethylene shielding configuration than for the aluminum shielding configuration for all electron flux calculations. However the extent of the difference in biological effectiveness for the two configurations cannot be immediately inferred from these data alone.

Following Kellerer's model [2], biological effectiveness was calculated by replacing the cumulative electron energy spectra N(E) with the simulated electron flux at the boundary of a cell monolayer, SN(E), as shown above.

$$R = \int r(E) SN(E) dE \tag{15}$$

For each of the flux calculations performed, biological effectiveness values were calculated. These values are listed in Table 3, along with the parameter c which represents the effect of electron range on biological effectiveness.

Entering	Exiting	c	RBE
Cell monolayer	Dish	0	1.18
		5	1.61
		10	2.25
		20	2.39
		100	3.76
Dish	Cell monolayer	0	1.25
		5	1.64
		10	2.24
		20	2.36
		100	3.64
Cell monolayer	Medium	0	1.22
		5	1.62
		10	2.26
		20	2.39
		100	3.85
Medium	Cell monolayer	0	1.20
		5	1.45
		10	1.86
		20	1.95
		100	2.91

Table 3. RBE values calculated for four electron flux simulations and five range effect parameters.

Comparing these data with the values calculated using the cumulative energy spectra, greater RBE values are seen using the simulated electron energy spectra.

In the following sections, methods of experimentally determining differences in biological effectiveness are demonstrated, and data generated with these methods are compared with data predicted by this model.

4.3 Design of ^{241}Am Irradiators for Determination of RBE of Low-energy Photons

In the previous section a method of calculating RBE based on the photon spectrum of a radiation field was demonstrated. In order to experimentally determine RBE values for low dose-rate low-energy photon fields, it was necessary to design irradiators capable of delivering equal dose-rates with different energy spectra.

The ^{241}Am foils provided photons ranging in energy from 10-60 keV. Using these foils, several shielding configurations yielding different energy spectra and dose-rates were considered. The section below describes two of these configurations which deliver approximately equal dose-rates (within 0.02 cGy/h difference).

4.3.1 Shielding Materials

In order to find two shielding configurations with significantly different energy spectra but with approximately equal dose-rates, different types of shielding were used. Aluminum, with no fluorescence photons above 1.6 keV and a ratio of 10 keV and 60 keV attenuation coefficients of 94.25 [8], was ideal for reducing the ratio of low energy photons (10-30 keV) to 60 keV photons. Polyethylene, with a ratio of attenuation coefficients of 13.53 for 10 keV and 60 keV photons, was identified as a material for shielding the photons across the 10-60 keV range more consistently than aluminum.

4.3.2 Aluminum Shielding Configuration

In order to achieve a maximum difference in energy spectra produced by aluminum and polyethylene shielding while maintain equal dose-rates, the energy spectra of ^{241}Am shielded by several thicknesses of aluminum was observed using the Amptek X123 spectrometer and analyzed using the methods discussed in Chapter 2.

The dose-weighted energy spectra, produced as demonstrated in Chapter 2, were analyzed in order to determine the relative contributions to dose from the 10-60 keV photons. It was found that for the spectrum emitted by ^{241}Am shielded with 0.5 cm Al, approximately 90% of the total dose was delivered by the 60 keV gamma photons. The fluence and dose-weighted spectra for this shielding configuration are shown in Figure 6.

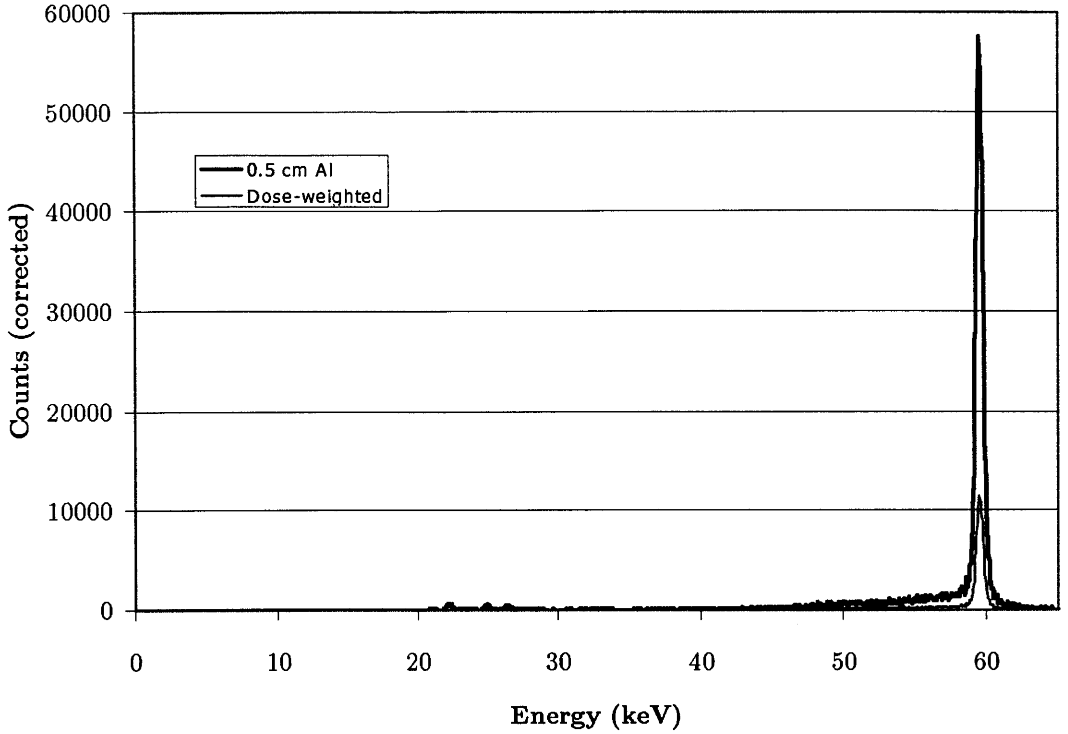

Figure 11. Fluence and dose-weighted spectra for the ^{241}Am foils shielded with 0.5 cm Al.

In this figure, note the large number of 59.54 keV photons relative to the number of photons at lower energies. When the dose-weighted counts are summed, fractions of dose delivered by photons of different energies can be calculated. Table 2 lists the fractions of dose delivered by photons in several energy ranges.

<10 keV	10-20 keV	20-30 keV	50-60 keV
0.01	0.01	0.08	0.90

Table 2. Dose-weighted fraction of counts in the energy ranges <10 keV, 10-20 keV, 20-30 keV, and 50-60 keV for the aluminum shielded ^{241}Am.

In order to maximize the dose-rate delivered by this photon field for biological exposures, two ^{241}Am foils were shielded by 0.5 cm Al, and the dose-rate was measured between these shielded foils. This configuration is illustrated in Figure 14. The dose-rate for this configuration was measured using Landauer nanodots sealed and submerged in 8 mL cell growth medium as shown in

Figure 12. The dose-rate was measured as 0.275 ± 0.016 cGy/h when corrected for the energy dependence of the nanodots using the methods of Chapter 2.

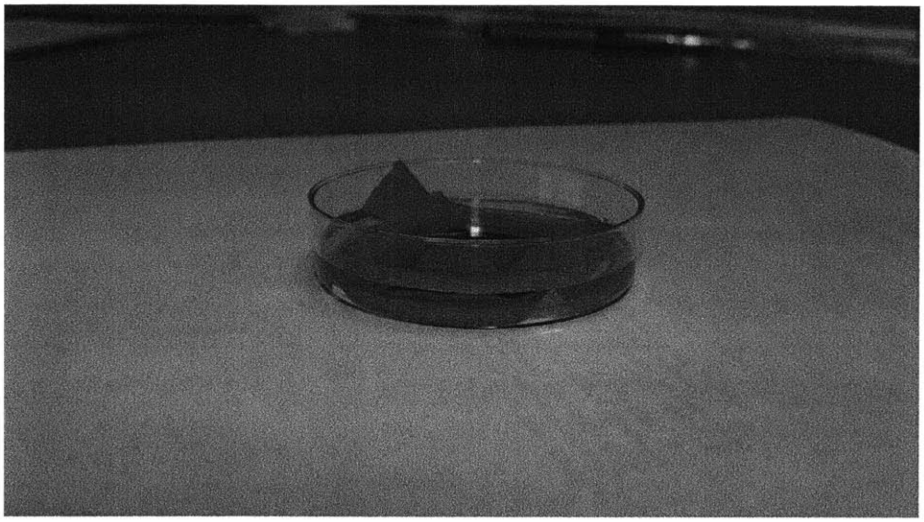

Figure 12. Nanodot sealed beneath a layer of cell medium.

In this figure note that the nandot dosimeter is completely submerged beneath cell culture medium.

4.3.3 Polyethylene Shielding Configuration

The dose-rate delivered by ^{241}Am shielded by several thicknesses of low density polyethylene (0.9 g/cm^3) was also measured. A dose-rate of 0.274 ± 0.011 cGy/h was measured for a ^{241}Am foil shielded by 29 mm of polyethylene using the same submerged dosimeter method as described above. The fluence and dose-weighted spectra for this shielding configuration are shown in Figure 13.

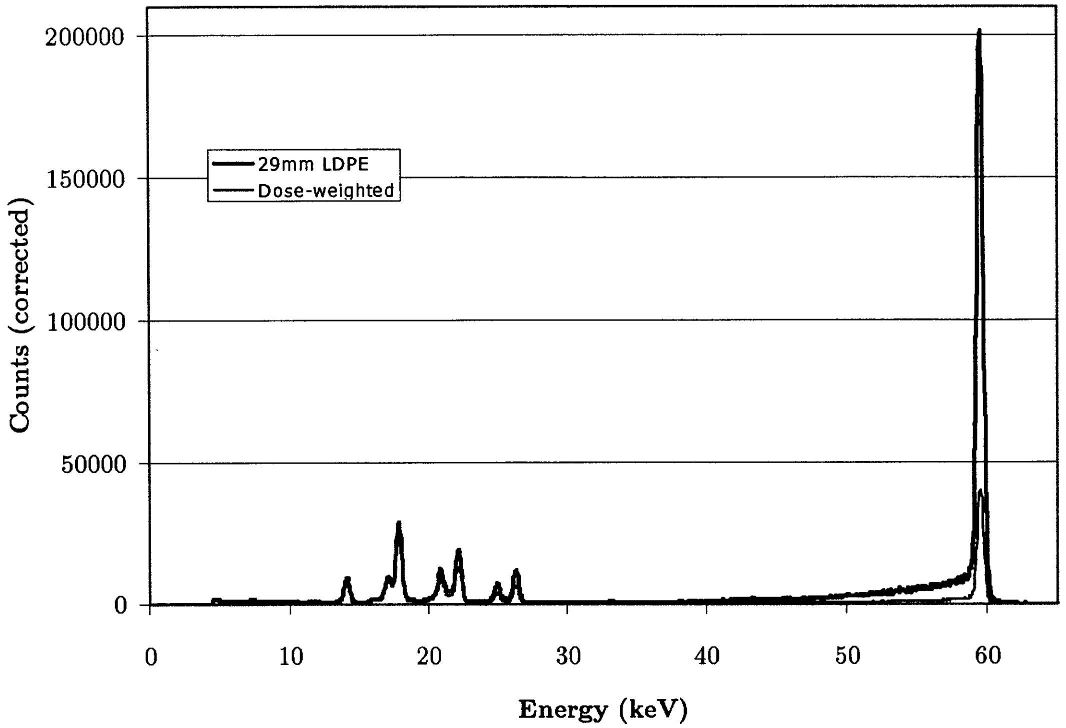

Figure 13. Fluence and dose-weighted spectra for the ^{241}Am foils shielded with 29 mm polyethylene.

In this figure, note the greater fraction of 10-30 keV relative to the aluminum shielding configuration. When the dose-weighted counts are summed, the following fractions of dose were found for the different energy ranges:

<10 keV	10-20 keV	20-30 keV	50-60 keV
0.01	0.37	0.24	0.38

Table 3. Dose-weighted fraction of counts in the energy ranges <10 keV, 10-20 keV, 20-30 keV, and 50-60 keV for the polyethylene shielded ^{241}Am.

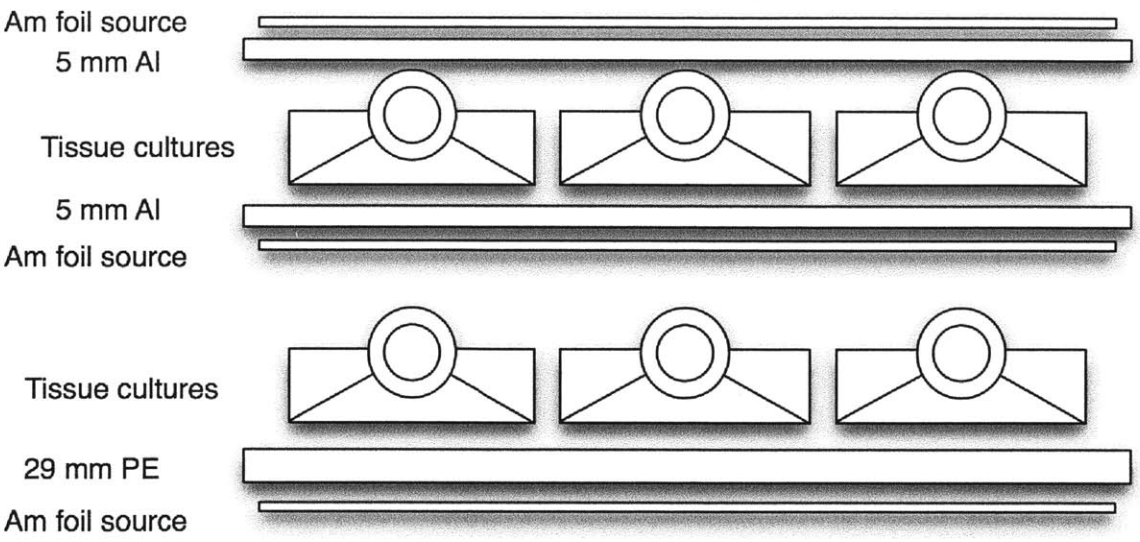

Figure 14. Two irradiator configurations for cell culture using aluminum and polyethylene shielding.

Using the ^{241}Am source configurations presented in this section, it is possible to deliver dose-rates of 0.275 ± 0.02 cGy/h with two different photon spectra. In Section 4.2.2, it was shown that the RBE for these shielding configurations can be estimated using spectral data. The following sections are a description of a method for experimentally determining differences in biological effectiveness for the two spectra discussed above.

4.4 Measuring Differences in Biological Effectiveness at Low Dose-rates

In order to measure biological impact of the low dose-rate low-energy photon field emitted by ^{241}Am, colony forming assays were considered based on previous findings at low dose-rates. Among the literature discussing colony forming assays, there is much variation in the parameters used. The following sections are a description of these parameters and the selection of parameters chosen in determining biological impact of the low dose-rate fields discussed above in Section 4.3.

4.4.1 Colony Forming Assays

Colony forming assays have been used to determine the effects of radiation since Puck and Marcus first reported the survival of HeLa cells irradiated with 230 kVp x-rays [12]. Many researchers have used similar colony forming assays to measure the effects of different types of radiation, drugs, pathogens, and atmospheric conditions on many types of cells in culture. In choosing the exact form of colony forming assay used to measure the RBE of low-energy photons at low dose-rates, published records of these experiments were considered. In the following sections several different reports of colony forming assays, each with different experimental parameters, are reviewed. A selection of experimental parameters for a colony forming assay based on these reports is also discussed.

4.4.1.1 Previous Work with Colony Forming Assays

The formation of colonies of cells in culture has been used to measure the effects of toxic agents on cell survival and reproduction. There are several possible variations of assays which use the formation of colonies as an endpoint. Each of these variations may have an impact on the outcome of the experiment. In designing an experiment to observe any differences in biological effectiveness due to photon energy of low dose-rate radiation, the goal was to use an assay with great enough sensitivity to observe potentially small differences in cell survival.

Of particular concern was the timing of radiation relative to plating. In previous work with acute irradiations, a period of time has sometimes been allowed to elapse in order to allow cells to adhere. Since non-adherent cells may have different cross sectional area and metabolic state than adherent cells, it is possible that an acute exposure to a non-adherent cell will not yield the same result as an acute exposure to an adherent cell. However, this time delay is not universal, and in several instances discussed below, exposure occurs prior to seeding or immediately after seeding, especially for chronic exposures.

In the following sections we outline some of the previous work with colony forming assays. A summary of possible variations of the assays is listed in Table 4. A colony forming assay method for determining differences in biological effectiveness for low-energy photon fields based on this review of earlier work is also presented.

4.4.1.2 Colony Forming Assays with Radiation

Puck and Marcus measured colony formation of HeLa cells exposed to a 230 kVp x-ray spectrum filtered with 1 mm Al and 0.5 mm Cu at dose-rates of 1-2 Gy/min [12]. Some samples were cultured with a feeder layer, a layer of cells irradiated between 5-40 Gy to prevent reproduction but allow metabolic processes to continue. This experiment was performed to analyze the effect of growth factors for cultures of different plating densities. Cultures were allowed to adhere for 5-24 hours before irradiation. Colonies were formed for 9-17 days after irradiation. They found no difference between cultures with and without a feeder layer, so their subsequent investigations did not include this feature.

Later investigations have also used colony forming assays to study the effects of other radiation fields. Of particular interest are those studies observing the effects of low dose-rate radiation on cell clonogenicity.

Werts et al. investigated the survival of two human cervical carcinoma cell lines [13], HTB35 and HTB35-60 after irradiation by both 275 kVp x-rays at 0.74 Gy/min and ^{60}Co gamma photons at 17.76 cGy/h. In these experiments, the cells were irradiated before seeding. They found reduced surviving fractions with increased dose for both radiation fields. They also found that the surviving fraction curve for the low dose-rate case could be approximated closely using only a linear term when fitted to the linear quadratic model, supporting the model of Brenner et al. presented above.

Williams et al. investigated the effects of ^{137}Cs gammas at a dose-rate of 25 cGy/h on a set of 39 human tumor cell lines [14]. Cells were exposed to the radiation source before seeding and allowed to grow into countable colonies. They made comparisons with cultures irradiated before seeding at 0.7 Gy/min with a ^{60}Co source [15]. These radiation and timing conditions produced measurable surviving fraction differences. For example, for the cell lines classified as very sensitive, surviving fractions were found to be approximately 1% with 6 Gy delivered at 25 cGy/h, while cell lines classified as very resistant showed surviving fractions of 30% with the same dose and dose-rate.

Pomp et al. investigated colony formation of the human melanoma cell line IGR39, normal human fibroblast cell lines BAR1 and S33, and the Chinese hamster ovary cells AA8 exposed to 0-4 Gy dose delivered by 5 MeV accelerator photons [16]. For the melanoma cells, a four hour period elapsed between seeding and irradiation. The fibroblast cultures were irradiated before seeding. Colony formation was measured for both irradiated and unirradiated cultures by counting the colonies formed after 2-3 weeks of incubation. Although the assay performed in these experiments was nearly identical to many other experiments documented here, the authors chose to describe their experiments as measurements of plating efficiency rather than clonogenicity. Also of interest for this study was the use of different seeding protocols for the different cell lines used. Both protocols yielded measurable differences in surviving fraction between irradiated and unirradiated cultures.

DeWeese et al. studied the effects of ^{226}Ra photons at 25 cGy/h and ^{137}Cs photons at 1 Gy/min on DU145, PC3, PPC1, TSUPr1, and LNCaP cells. Cells were irradiated in subconfluent flasks before seeding into flasks for the colony forming assay. Their results show that it is possible to measure loss of clonogenicity for doses delivered at rates as low as 25 cGy/h using cells irradiated before seeding. Also shown was the dominance of the linear term in the linear-quadratic fitting of the low dose-rate data, again supporting the model of Brenner et al. presented above.

Mitchell et al. studied colony forming of six different cell lines (HeLa, V79, LP59, CCL33, CCL157, and CCL56) exposed to ^{137}Cs gamma photons at dose-rates of 10-270 cGy/h [18]. Exposures were conducted immediately after plating in order to prevent proliferation before exposure. They also determined the unirradiated plating efficiency for each cell line in separate experiments. They developed surviving fraction curves relative to these unirradiated controls. These are reported in Figures 15, and 16.

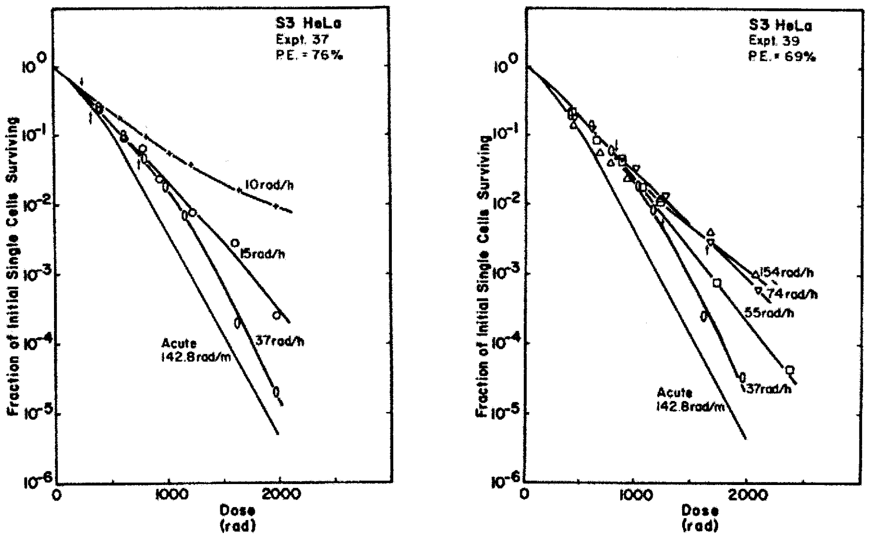

Figure 15. Survival curves for S3 HeLa cells exposed to ^{137}Cs gamma photons at the labeled dose-rates. For the lower dose-rate experiments illustrated in the left panel, irradiation occurred as cells were proliferating.

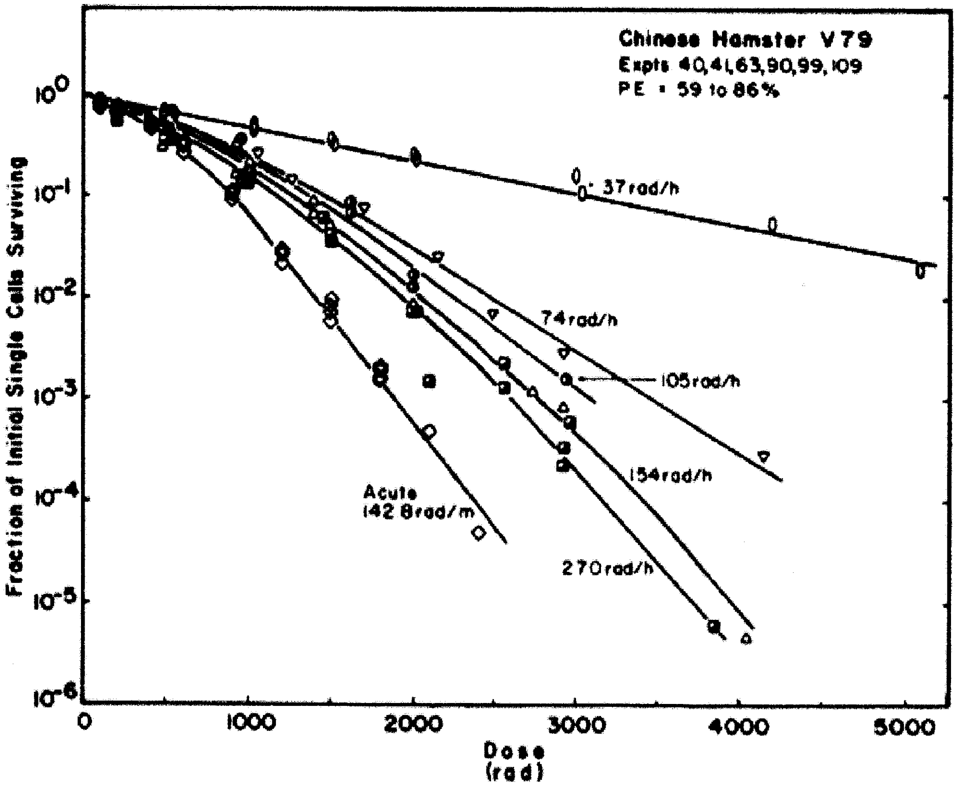

Figure 16. Survival curves for Chinese hamster V79 cells exposed to ^{137}Cs gamma photons at the labeled dose-rates.

The data in these figures show that a dose-rate of 10 cGy/h was sufficient to reduce surviving fraction for some cell lines when irradiation was performed immediately following seeding. Also of note was the greater resistance of V79 cell lines to low dose-rates relative to the other cell lines. The authors suggest that this resistance may be due to the shorter doubling time of V79 cells (8 hours) relative to the other cell lines (20 hours and above).

4.4.1.3 Colony Forming Assays with Chemical Agents

Exposure to low-dose rate radiation occurs over an extended period of time, while much of the work presented above is for acutely delivered doses of radiation. Because of this difference it is helpful to consider measurements of surviving fraction for types of chronic exposures when developing a timing protocol for low dose-rate surviving fraction studies. Here some studies of chronic exposure to chemical agents are discussed with focus on timing of exposure.

Grove and Cheng investigated the effects of the anti cancer compound B-L-(-)-Dioxolane-Cytidine on DU145 cells in exposures of 4-24 hours [19]. Cells were plated and exposed with no delay. After 4-24 hours, the cells were given new medium without the drug and allowed to form colonies for eight generation times. This seeding and exposure timing protocol provided the ability to observe reduced clonogenicity with increased concentrations of the compound and increased radiation exposure.

Saleem et al. investigated the effect of lupeol on clonogenicity of LNCaP prostate cancer cells [20]. Cells were seeded and incubated overnight before exposure to lupeol which was replenished in fresh medium every three days during colony formation. Cells were stained after 21 days of incubation. Reduced colony formation was found with increasing concentrations of lupeol, although this effect was shown over a limited range of magnitude. The minimum surviving fraction was approximately 40%. This study shows that an overnight delay between seeding and chronic exposure to a toxin can produce observable differences in surviving fraction.

4.4.1.4 Colony Forming Assays with Radiation and Other Agents

Roa et al. investigated the combined effects of glucose-capped gold nanoparticles and a 2 Gy dose of ^{137}Cs gamma photons on DU145 human prostate carcinoma cells at a dose-rate of 1.32 Gy/min before seeding into dishes for the colony forming assay [21]. The glucose-capping of these nanoparticles enhanced their uptake into the cytoplasm of cells over neutral nanoparticles. They found evidence that these gold nanoparticles in a 15 nM concentration increased radiosensitivity and reduced surviving fraction to approximately 40% of the non-irradiated control. This study shows that acute exposure to a combined dose of radiation and gold nanoparticles prior to seeding can be used to observe differences in surviving fraction.

Serafin et al. studied the combined impact of a 7 Gy dose of ^{60}Co gamma photons along with either of the anti-cancer drugs cisplatin, etoposide, or vinblastine for the DU145 cell line [22]. In their procedure cells were incubated for 24 hours prior to irradiation and then allowed an additional period of time to yield maximal G2 arrest before drugs were applied. They found decreased percentage survival for the combination of radiation and drugs applied at G2 arrest over drugs applied immediately after irradiation. This study shows that timing of G2 arrest following an acute irradiation can have a significant impact surviving fraction with chronic exposure to drugs.

Wilkins et al. investigated the combined effects of cisplatin and radiation on two glioma cell lines, U373MG^{CP} (cisplatin resistant) and U373MG (cisplatin sensitive) [23]. Cells were exposed to ^{226}Ra gamma photons at 52.8 cGy/h as well as 150 kVp x-rays at a dose-rate of 1.12 Gy/min. These cells were then seeded and exposed to medium containing cisplatin which was replenished every 12 hours by replacing the culture medium. For this chronic exposure to a toxin immediately after seeding, cisplatin was shown to have a greater effect on surviving fraction for the cisplatin sensitive cell line than on the cisplatin resistant cell line. This study shows again that chronic exposures to cisplatin immediately after seeding have an observable impact on surviving fraction.

4.4.1.5 Summary of Previous Relevant Work with Colony Forming Assays

Despite the work of Plumb [24], Federoff and Richardson [25], and Franken [26], who have attempted to codify a standard protocol for colony forming assays, it is evident from the literature there is no prevailing standard method. Many differences exist among the studies detailed above. One of the most important, especially for the consideration of low dose-rate exposures over long periods of time, is the difference in timing of exposures. While neither Plumb or Federoff describe the need for a delay between seeding and exposure to other agents, some studies above have delayed between 4-24 hours between seeding and exposure.

In order to choose a timing protocol for colony forming assays with the ^{241}Am sources, the methods and results reported above were considered. The study by Mitchell et al., describing the effects of several different dose-rates on a range of cell lines, was particularly useful. This study described the effects of low dose-rate radiation (10 cGy/h), which is comparable to the dose-rate of 2 cGy/h delivered by the foil sources. Grove et al. also used no delay between seeding and exposure for continuous exposure to the anti-cancer drug β-L-(-)-dioxolane-cytidine. For these studies, surviving fraction is reported as the number of colonies found after exposure divided by the number of colonies in a control condition.

Others have exposed cells to radiation before seeding, although for these studies, dose-rates were higher than the minimum dose-rates considered by Mitchell et al. Others studying the effects of acute exposures of radiation have used a delay period between seeding and exposure as shown in Table 4.

Author	Cell line(s)	Radiation Field/Toxin	Dose-rate/Concentration	Exposure Timing
Puck et al.	HeLa	230 kVp/1mm Al/0.5mm Cu	1-2 Gy/min	5-24 hours after seeding
Werts et al.	HTB35, HTB35-60	275 kVp/1mm Cu	0.74 Gy/min	Before seeding
Williams et al.	Various human tumor	^{137}Cs (^{60}Co)	25 cGy/h (0.7 Gy/min)	Before seeding
Pomp et al.	IGRneo, IGRmyc, IGRras	4-5 MeV photons	N/A	4 hours after seeding
DeWeese et al.	LNCaP, DU145, PC3, PPC1	^{137}Cs	25 cGy/h or 1 Gy/min	Before seeding
Mitchell et al.	HeLa, V79, LP59, etc.	^{137}Cs	10–270 Gy/h	No delay
Grove et al.	DU145	β-L-(-)-dioxolane-cytidine	0.001-1 μM	No delay
Saleem et al.	LNCaP	Lupeol	20-50 μM	Overnight
Roa et al.	DU145	^{137}Cs/Au nano particles	1.32 Gy/min/15 nM	Before seeding
Serafin et al.	DU145	^{60}Co/cisplatin, etoposide or vinblastine	Acute	24 hours
Wilkins et al.	U373MG and U373MGCP	^{226}Ra (150 kVp)/cisplatin	52.8 cGy/h (1.12 Gy/min)	Before seeding

Table 4. A compliation of data from several colony forming experiments including dose and exposure timing.

Since the ^{241}Am sources provide a maximum dose-rate of 2 cGy/h, the decision was made to pursue the methods described Mitchell et al. in their study of dose-rates 10 cGy/h.

The study by Mitchell et al. was also helpful in guiding the choice of cell lines to consider in colony forming experiments at dose-rates of 2 cGy/h. The authors noted that for V79 Chinese hamster cells, the effect of the low dose-rate radiation was far less than for cell lines with longer doubling times. Due to this observation, cells with longer doubling times were used to study the relative effects of the photons emitted by the ^{241}Am foils in the work presented below.

Serafin et al. report a doubling time of 40 hours for DU145 cells [22]. These human prostate cancer cells are also of practical interest since continuous radiation is used in brachytherapy for prostate cancer, and since these cells were readily available, we chose to use them in our studies. Another cell-line with a long doubling time (20 hours [27]), practical interest, and ease of availability was the AG01522 human skin fibroblast cell line.

4.4.2 Colony Forming Experiment with Low Dose-rate Radiation Using ^{241}Am Foils

In order to measure differences in biological effectiveness for different photon spectra, both DU145 and AG01522 cells were grown to confluence in T25 flasks, trypsinized with 0.25 % trypsin, counted with a Coulter Counter (Number AG02022, Model Z2, Beckman Coulter, Brea, CA), and diluted to levels which would yield 50-200 colonies upon plating in T25 flasks. A single mixture of cells was prepared for plating all flasks of each experiment.

After plating the cells were exposed to radiation without delay. For each experiment, three flasks were incubated without exposure to radiation, three flasks were irradiated by a single ^{241}Am foil shielded by 29 mm of polyethylene, and three flasks were irradiated using two ^{241}Am foils shielded by 0.5 cm Al as described above.

AG01522 cells were exposed during incubation for periods of 4, 11, and 12 days. After the exposures of 4 and 11 days, flasks were moved to shielded areas within the same incubator for 8 and 1 days respectively. This incubation schedule kept the total incubation time at 12 days for all experiments with the AG01522 cell line, allowing colonies of at least 50 cells to be formed. DU145 cells were similarly exposed for 4, 7, and 8 days. For each cell line, these experiments were repeated in triplicate in order to limit experimental error.

Surviving fractions were calculated relative to the controls for each set of experiments. The surviving fractions for each repeat were then averaged. These data are shown in Tables 5 and 6. Uncertainties for these surviving fraction data were determined by averaging the uncertainties of the individual experiments. This method was chosen since it produced greater uncertainty than the standard deviation between repeats for all experiments in all cases.

For both cell lines, statistical significance between surviving fractions for each shielding configuration was determined using the student t-test. The data used for the t-test were the number of colonies observed for each shielding configuration divided by the average number of colonies for the respective control case. All differences were found to be statistically significant with p-value < 0.05. These values are shown in Tables 5 and 6.

		Al		LDPE		Al/LDPE
Days	Dose (Gy)	Survival	Uncertainty	Survival	Uncertainty	p-value
4	0.264	0.96	0.05	0.88	0.07	4.22E-02
7	0.462	0.95	0.04	0.84	0.05	5.41E-04
8	0.528	0.92	0.04	0.84	0.03	6.49E-04

Table 5. Surviving fraction data for the DU145 cell line.

		Al		LDPE		Al/LDPE
Days	Dose (Gy)	Survival	Uncertainty	Survival	Uncertainty	p-value
4	0.264	0.95	0.05	0.89	0.04	2.52E-03
11	0.726	0.91	0.04	0.74	0.03	2.22E-05
12	0.792	0.89	0.02	0.70	0.03	5.01E-08

Table 6. Surviving fraction data for the AG01522 cell line.

For these data, note the statistical significance of the difference in survival for the aluminum and polyethylene shielding configurations. In every case, surviving fractions were statistically significant as determined by Student's t-test.

By fitting the data presented above with the linear quadratic model, an estimate of the survival curves for each radiation field and cell line can be derived. These survival curves can be used to calculate RBE.

For both cell lines the data above was fit to the linear quadratic model for surviving fraction SF(D), with only a linear term, α, since it was demonstrated above that the quadratic term has a negligible contribution to the surviving fraction for low dose-rate radiation.

$$SF(D) = e^{-\alpha D} \tag{16}$$

The data shown above in Tables 5 and 6 are plotted along with fitted curves in Figures 17 and 18, and the α terms found are displayed in Table 7 along with doses required to reduce the surviving fraction to 0.5. For these α terms, the square-root of the mean of the squares of the residuals of the fit are included in the error column.

From these doses required to reduce survival to 0.5 according to Equation 16, RBE was calculated for the polyethylene-shielded field relative to the aluminum-shielding field for each cell line. These RBE values were found to be 2.65 for the DU145 cell line and 3.03 for the AG01522 cell line. With the error calculated based on the fit reported above, minimum and maximum RBE values were calculated using Equations 17 and 18 with α_{LDPE} and α_{Al} being the linear terms for the polyethylene shielding configuration and aluminum shielding configuration respectively.

$$RBE_{\max} = \frac{\alpha_{LDPE} + \Delta\alpha_{LDPE}}{\alpha_{Al} - \Delta\alpha_{Al}} \qquad (17)$$

$$RBE_{\min} = \frac{\alpha_{LDPE} - \Delta\alpha_{LDPE}}{\alpha_{Al} + \Delta\alpha_{Al}} \qquad (18)$$

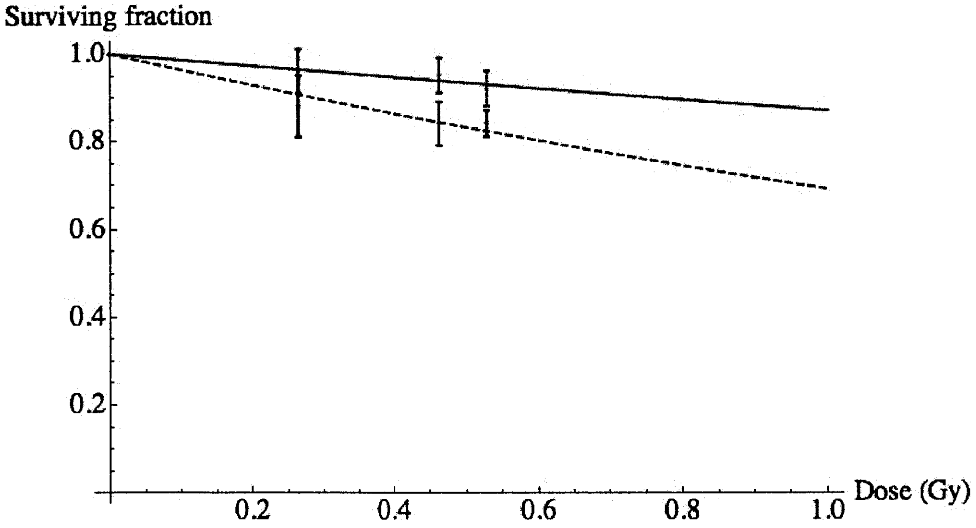

Figure 17. Surviving fractions for the DU145 cell line irradiated with aluminum (solid) and polyethylene shielding configurations (dashed).

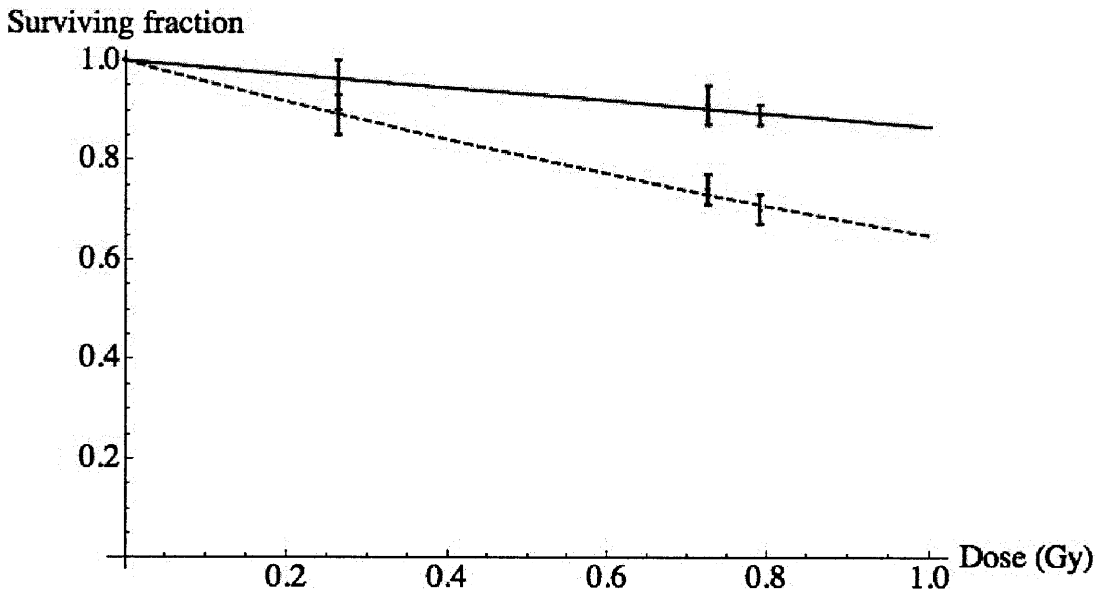

Figure 18. Surviving fractions for the AG01522 cell line irradiated with aluminum (solid) and polyethylene (dashed) shielding configurations.

In these figures note the reduced surviving fraction of the polyethylene shielding configuration relative to the aluminum shielding configuration.

	α_P	Error	α_A	Error	$RBE_{0.5}$	RBE Lower Bound	RBE Upper Bound
DU145	0.37	0.01	0.14	0.03	2.65	2.11	3.45
AG01522	0.43	0.01	0.14	0.02	3.03	2.63	3.66

Table 7. Fitting parameters and RBE calculated for the data in Figure 17. RBE data calculated with aluminum-shielded ^{241}Am field as reference.

In these data note that the lower bound for the RBE exceeds 2.0 for both cell lines.

4.5 Comparison of Experimental and Model Data

In the sections above, two ^{241}Am foil shielding configurations were identified which delivered approximately equal dose-rates with significantly different photon spectra. Two models for calculating RBE for two different photon fields were presented, and these models were used to calculate the RBE for the photon fields produced by two ^{241}Am foil configurations. Biological experiments were also conducted in order to determine RBE for these two photon fields.

For all methods, RBE values for these two photon fields were calculated with the reference field as the field produced by the aluminum shielding configuration. The best correlation between experimental observations and model predictions are for the model described above in Section 4.2.2.2.

For this model biological response is calculated based on the electron flux in a cell monolayer simulated with MCNP. This model also incorporates the range of these electrons, providing for greater biological response for 10-20 keV electrons which could impact more than one chromosome within a single cell nucleus due to their range and greater linear energy transfer than electrons with greater energy.

This model predicts RBE values of 1.21-3.54 depending on the magnitude of this range effect, while the model based on theoretical electron spectra described by Kellerer [2] predicts RBE values of 0.94-1.75 depending on the same magnitudes of range effect considered. For these ranges the lower values correspond to a range effect of magnitude zero. The model described by Brenner et al., which does not account for electron range, predicts an RBE of 1.74.

The experimental data predict RBE values of 3.03 for the AG01522 cell line and 2.65 for the DU145 cell line. It should be noted that models without consideration of electron range predict RBE values less than 2.0 for these photon fields in all cases. Models which consider the effect of range predict greater RBE values which agree more closely with biological data.

4.6 Conclusion

Using the spectroscopy and dosimetry methods presented in Chapters 2 and 3, the RBE of the low energy photons emitted by ^{241}Am foils have been analyzed using modeling and experiment. The biological data presented show that biological response to 10-30 keV photons is greater than that due to 60 keV photons. The model incorporating MCNP-simulated electron spectra and the effect of electron range provide the best agreement with this experimental data.

However, the magnitude of an electron range effect, if any, cannot be determined from the limited data presented here.

Since the number of chromosomes and size of the cell nucleus differs with cell type, it is likely that any electron range effect would differ with cell type. It may be possible to design experiments to investigate differences in this range effect by investigating multiple cell types.

The determination of RBE values for these ^{241}Am photon fields have implications beyond the modeling of biological response due to ionizing photons, since risk estimates for ionizing photons are based on exposures to photons with energies greater than 1 MeV. Several studies described in Chapter 1 have suggested that biological response is greater for lower energy photons, and the results of this study also support this trend of increased biological response with decreased photon energy.

A reassessment of risk estimates taking these findings into account could encourage the use of photons of greater energies for mammography, for which 10-30 keV photons are currently used. These findings could also encourage the investigation of alternate sources for brachytherapy, for which 27-31 keV (^{125}I) and 20-22 keV (^{103}Pd) photons are also currently used.

4.7 References

1. D. J. Brenner, C. S. Leu, J. F. Beatty, R.E. Shefer, Phys. Med. Biol. 44 ,1999, 323-333.
2. A. M. Kellerer, Radiation Research, 158, 2002, 13-22.
3. M.J. Berger, J.H. Hubbell, S.M. Seltzer, J. Chang, J.S. Coursey, R. Sukumar, and D.S. Zucker, Photon Crhoss Sections Database, NBSIR 87-3597, NIST.
4. R. D. Evans, The Atomic Nucleus, (McGraw-Hill, London, 1955).
5. M.J. Berger, J.S. Coursey, M.A Zucker, and J. Chang, Stopping-Power and Range Tables for Electrons, Protons, and Helium Ions, NISTIR 4999, NIST.
6. M. Bistrovic, M. Biscan, T. Viculin, Radiotherapy and Oncology, 7, 1986, 175-180.
7. M. A. Hill, Radiation Protection Dosimetry, 112, 4, 2004, 471-481.

8. J.H. Hubbell and S.M. Seltzer, Tables of X-Ray Mass Attenuation Coefficients and Mass Energy-Absorption Coefficients, NISTIR 5632, National Institute of Standards and Technology.
9. M. Zaider, D. J. Brenner, Radiation Research, 103, 1985, 302-316.
10. ICRU, "The quality factor in radiation protection", ICRU Report 40, Bethesda, MA.
11. P. Kliauga, R. Dvorak. Radiation Research, 73, 1978, 1-20.
12. T. T. Puck, P. L. Marcus, Journal of Experimental Medicine, 103, 1956, 653-666.
13. E. D. Werts, D. R. Burholt, W. R. Paljug, S. L. Polizotto, V. M. Yann, International Journal of Oncology Biology Physics, 35, 5, 1996, 941-950.
14. J. R. Williams, Y. Zhang, H. Zhou, D. S. Gridley, C. J. Koch, J. M. Slater, J. B. Little, International Journal of radiation Oncology Biology Physics, 72, 3, 2008, 909-917.
15. J. R. Williams, Y. Zhang, J. Russell, International Journal of Radiation Biology, 84, 2008, 253-264.
16. J. Pomp, J. L. Wike, I. J. M. Ouwerker, C. Hoogstraten, J. Davelaar, P.I. Schrier, J.W.H. Leer, H D. Thames, and W. A. Brock, Radiotherapy and Oncology, 40, 1996, 121-125.
17. T. L. DeWeese, J. M. Shipman, L. E. Dillehay, W. G. Nelson, Journal of Urology, 159, 1998, 591-598.
18. J.B Mitchell, J.S. Beford, and S. M. Bailey, Radiation Research, 54, 1973, 316-327.
19. K. L. Grove, and Y. Cheng, Cancer Research, 56, 1996, 4187.
20. M. Saleem, I. Murtaza, R. S. Tarapore, Y. Suh, V. M. Adhami, J. J. Johnson, I. A. Siddiqui, N. Khan, M. Asim, B. B. Hafeez, M. T. Shekhani, B. Li, and H. Mukhtar, Carcinogenesis, 30, 5, 2009, 808-817.
21. W. Roa, X. Zhang, L, Guo, A. Shaw, X. Hu, Y. Xiong, S. Gulavita, S. Patel, X. Sun, J. Chen, R. Moore, and J.Z. Xing, Nanotechnology, 20, 2009, 375101.
22. A. M. Serafin, A. B. Binder, and L. Bohm, Urology Research, 29, 2001, 221-227.
23. D. E. Wilkins, C. E. Ng, and G. P. Raaphorst, International Journal of Radiation Oncology Biology Physics, 36, 1, 1996, 105-111.
24. J. A. Plumb, Methods in Molecular Medicine, 28, 1999, 17-23.
25. S. Federoff, A. Richardson, Protocols for Neural Cell Culture (Humana, Totowa, NJ), 2001, 307-315.
26. N.A.P. Franken, H. M. R., J. S., J. Haveman, and C. van Bree, Nature

Protocols, 1, 2006, 2315-2319.
27. N. Hamada, T. Funayama, S. Wada, T. Sakashita, T. Kakizaki, M. Ni, and Y. Kobayashi, Radiation Research, 166, 2006, 24-30.

Chapter 5: ^{241}Am Animal Irradiator

5.1 Background and Previous Work

As discussed in Chapter 1, several investigators have studied the effects of low dose-rate radiation on mice. The experimental difficulty of radiation delivery is approached differently in different studies. In some studies tritiated water has been delivered internally to mice. In other studies, radioisotopes were positioned external to the mice in order to deliver photon radiation.

Both of these approaches have logistical and safety issues that complicate their implementation. Tritiated water administered internally is released into the animal habitat since it does not decay fully within the animal. Since the half-life of tritium is 4500 ± 8 days, it is necessary to gather the animal bedding and dispose of it as radioactive waste in order to prevent its release into the environment.

In studies in which radiation is delivered from sources external to the mice, safety is also a concern. Some studies have been conducted using ^{137}Cs or ^{60}Co sources which emit photons of 667 keV, 1.17 MeV, and 1.33 MeV. These photons are difficult to shield, requiring lead greater than 1 cm thickness to attenuate by a factor of 10 [3]. Shielding a 1 m^3 volume with 1 cm of lead on all sides would require 681 kg of lead. In order to conduct large scale experiments with these sources, dedicated facilities are required to accommodate the large amounts of shielding necessary.

Some studies have used x-ray generators to irradiate animals continually at low dose-rates. These devices require constant electric power and cooling in order to function continually. This requirement complicates their use since any failure in electric power supply, cooling system or x-ray tube would halt irradiation. During a long low dose-rate exposure, such a failure could ruin months of work.

In order to avoid the use of large amounts of shielding or continually operating x-ray generators, Olipitz, et al. describe an animal irradiator for low dose-rate mouse studies utilizing ^{125}I as a radiation source [2]. A phantom containing ^{125}I dissolved in an aqueous solution of sodium hydroxide is positioned directly below a platform on which mice cages are located. This design delivers photon radiation to mice at dose-rates of 0.0126-0.126 cGy/h, depending on the concentration of ^{125}I.

Because of the relatively low energy photons emitted by ^{125}I (32 keV maximum), this design offers the advantage of requiring limited shielding to protect the surrounding environment. However these low energy photons are readily attenuated in the water within the phantom, limiting the dose-rate to the animals above. Also the relatively short half-life of ^{125}I (59.41 days) necessitates refilling the source phantom every week and introduces a 10% variation in dose-rate during exposure [2].

This design served as the basis for the ^{241}Am animal irradiators described in this chapter. By replacing the ^{125}I liquid with ^{241}Am foil sources, the dose-rate can be increased (0.8 cGy/h for ^{241}Am vs. 0.12 cGy/h for ^{125}I) and stabilized over a period of years. With a half-life of 432.2 years, ^{241}Am decays only 0.32% over a period of two years.

Figure 1 shows the ^{125}I irradiator design adapted to include the ^{241}Am foil sources. With the foil configurations described in Section 5.3 and additional shielding described in Section 5.2.5, this irradiator design provides increased dose-rate over the ^{125}I irradiator while maintaining a safe environment.

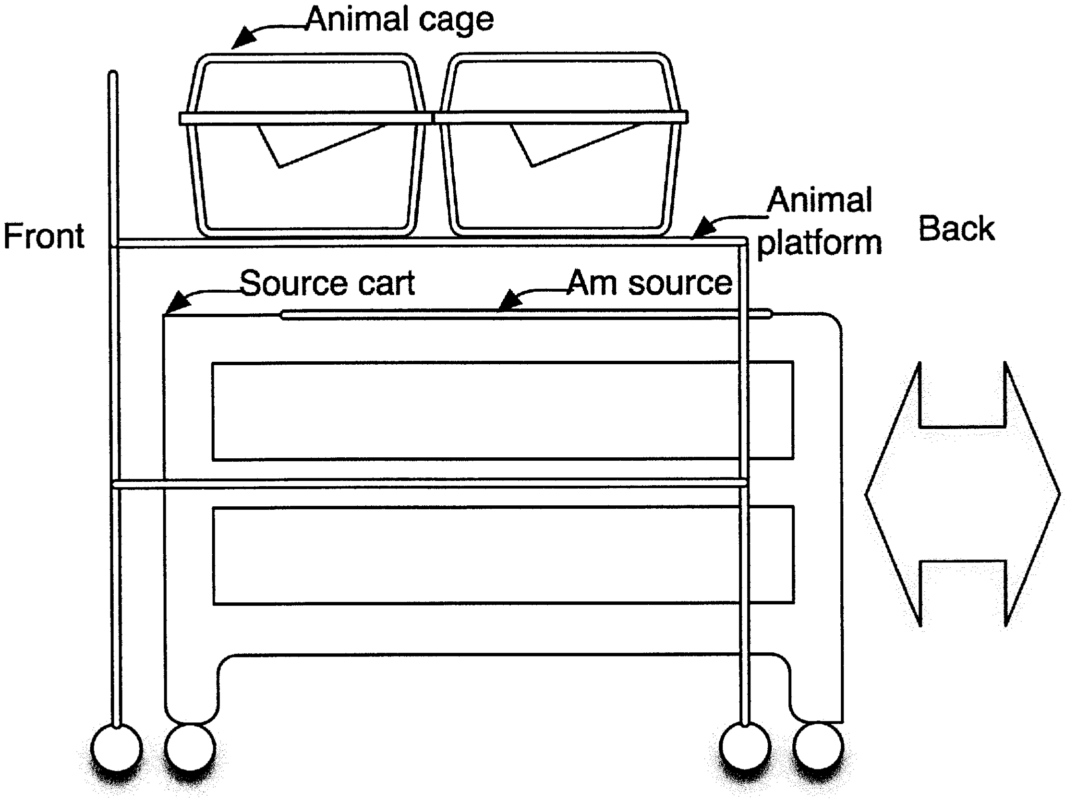

Figure 1. Sketch of ^{241}Am irradiator design based on Olipitz et al. [2] without shielding.

5.2 Design goals for the Animal Irradiator

Several objectives were considered when designing the ^{241}Am animal irradiator. Safety concerns, experimental flexibility, and dose-rate consistency were among the factors in guiding the final design. In the following section these goals are discussed. An animal irradiator design meeting these goals is also described.

5.2.1 Maximizing Dose-rate

In order to conduct experiments across a large range of dose-rates, it was necessary to devise a ^{241}Am source configuration which was capable of delivering the maximum possible dose-rate to the animals in the irradiator. In order to achieve this goal, the nine and twelve foil source configurations were developed and are presented below in Section 5.3.3.

5.2.2 Maintaining Consistent Dose and Dose-rate Throughout an Experiment

In any experiment consistent control over the experimental parameters is necessary for consistent results. In the case of animal irradiations, the important experimental parameters are dose and dose-rate. According to the design presented below, dose is kept consistent between animals on the same irradiator platform by rotating cages periodically during an experiment. This rotation protocol has been discussed in detail by Olipitz et al. [2]. With this rotation of cages, an animal walking randomly within a cage will spend approximately the same amount of time in each spot on the platform. With this approximation the dose delivered to the animal is approximately equal to the mean of dose across the entire animal platform.

As discussed below in Section 5.3.1.4, the standard deviation of the dose-rate across the platform will determine the variation in the dose-rate for an animal on the platform. For this reason, four different source configurations were developed which have different standard deviations of dose-rate across the platform.

Since multiple animal irradiators may be located in close proximity in an experimental environment, it was necessary to limit the dose delivered from neighboring irradiators in order to insure consistent dose delivery. This limiting of dose was achieved with the shielding configuration presented in Section 5.2.5.

5.2.3 Maintaining Consistent Dose and Dose-rate within the Body of an Animal

As a photon field emitted by ^{241}Am enters the body of an animal, some photons are absorbed by the tissue of the animal. Because of this absorption, fewer photons reach the points of the animal farther from the source. This effect results in a variation in dose within the animal. In designing the animal irradiator, it was necessary to understand this variation and to minimize it.

In order to measure this attenuation within an animal on the irradiation, dose delivered through 1-20 mm of polyethylene plastic in an animal cage was measured. Polyethylene was chosen because of its similarity to tissue, having a density of 0.9 g/cm^3 and having a maximum atomic number of 6. For this experiment, nine ^{241}Am foils were placed on the source platform 4.5 cm below the animal platform. A single mouse cage with wood chip bedding 1 ± 0.1 cm thick was placed on the center of the animal platform. Several nanodot dosimeters were annealed with sunlight and read with the Microstar reader. Dots with residual dose readings of less than 0.01 cGy were used to measure the dose delivered to the center of the platform through 1-20 mm thicknesses of polyethylene plastic. The data from this experiment were corrected for the energy spectrum measured at the center of the platform, reported in Section 5.3.1.3. The corrected dose data are shown in Figure 2.

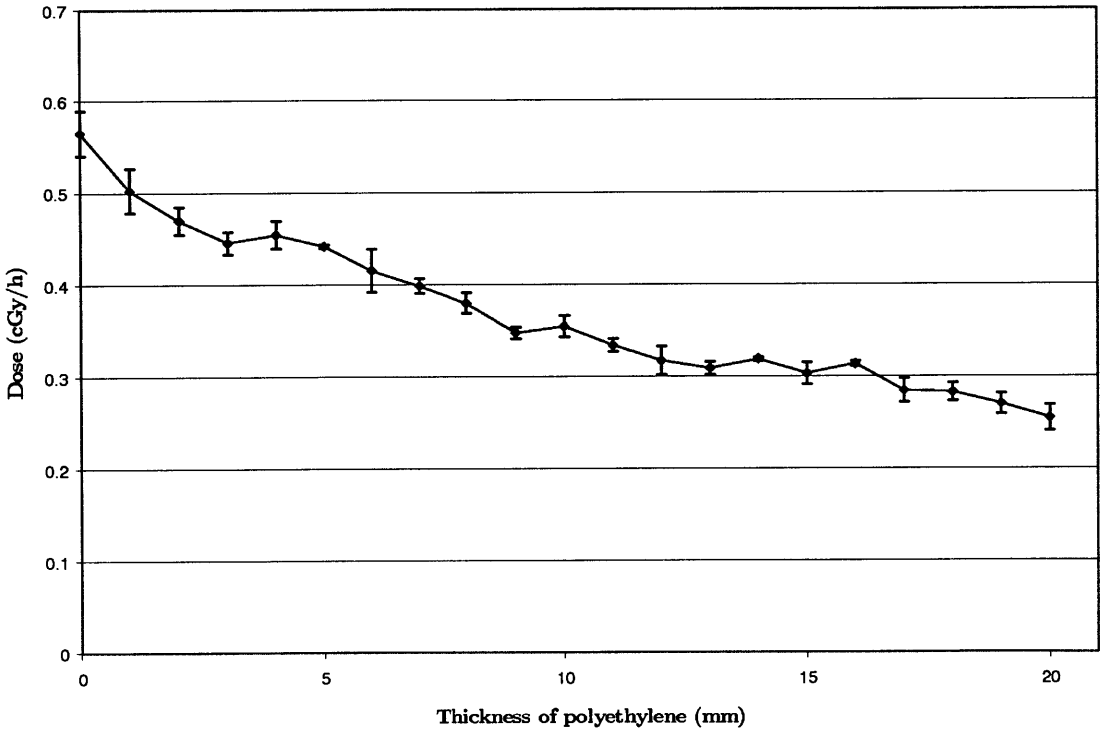

Figure 2. Dose vs. depth of polyethylene plastic as measured with the Landauer nanodot dosimeters.

5.2.4 Maximizing the Number of Experiments Conducted Concurrently

Since there are thirty one ^{241}Am foils available, it was necessary to consider the number of experiments which could be performed concurrently with this limited number. Four foil configurations were considered which allow for 8, 12, 28, or 124 cages to be irradiated concurrently. These configurations are discussed below in Sections 5.3.3

5.2.5 Maintaining Experimental Safety

In order to comply with Nuclear Regulatory Commission (NRC) dose limits, it was necessary to construct a layer of shielding around the animal irradiator. Several designs were considered in order to provide a safe environment for laboratory workers and to insure consistent irradiations. A shielding design which meets these requirements is presented in this section.

NRC regulations require that no more than 2 mrem may delivered in any one hour to an unrestricted area [1]. Since the ^{241}Am irradiator delivers a stable dose-rate, the dose-rate limit for any unrestricted area around the irradiator is 2 mrem/h. The front of the ^{241}Am irradiators must remain unrestricted in order to allow animal care workers to monitor the animals, so the dose-rate to the area occupied by these workers must be limited to 2 mrem/h.

In order to limit the dose-rate in this area to below this 2 mrem/h level, lead metal shielding and leaded polyethylene plastic were used. For the area through which animal care workers would view the mice during an experiment, leaded polyethylene plastic 2.5 cm thick was hung from a support beam above the animal irradiator. This leaded polyethylene extended 31 cm above the animal platform and is pictured in Figure 4.

Lead metal shielding was used along the front of the animal platform around the edges of the leaded polyethylene plastic. Lead was attached to layers of polyethylene plastic 2.5 cm thick in order to provide rigidity. A layer of polyethylene plastic 1 mm thick was used to cover the lead, and these layers of polyethylene were sealed with plastic tape to insure a smooth surface for ease of cleaning. This lead metal and polyethylene plastic assembly is shown in Figure 3 and pictured in place on the irradiator in Figure 4.

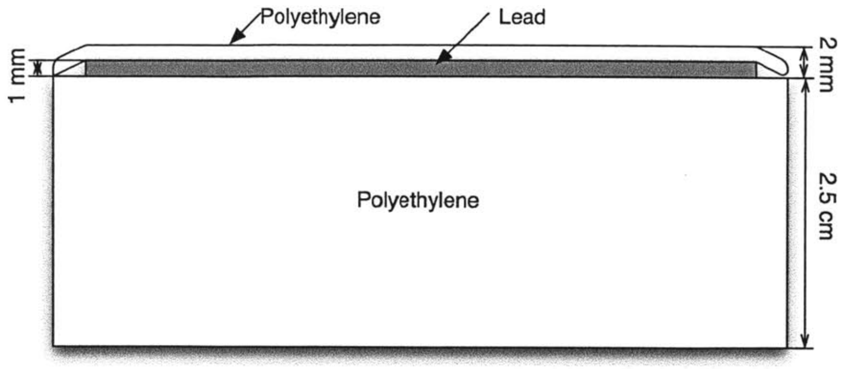

Figure 3. Cross section view of the lead and polyethylene plastic used for shielding.

In order to shield animals in an experiment from radiation emitted by neighboring irradiators, this same lead metal and polyethylene plastic shielding configuration was used to surround the animal platform. Slabs of polyethylene plastic/lead metal extending 9 cm below the animal platform and 20.5 cm above the platform were fixed to the platform on both sides. A slab of polyethylene plastic/lead metal shielding extending 31 cm above the animal platform was fixed to the platform on the back side in order. This allowed the source cart to slide beneath the animal cart through this side.

With this shielding in place dose-rates in the area immediately surrounding the irradiator were measured using a Model 3 Survey Meter (#PR249321, Ludlum Instruments, Sweetwater, TX), which was calibrated on 12/2/2009. Dose-rates for the source configuration with 12 foils are reported in Table 1. These dose-rates are the maximum dose-rates at these locations for any of the configurations, since the 12 foil configuration has the most activity as discussed in Section 5.3.

Location	Dose-rate
1 cm from leaded polyethylene window	0.3 mrad/h
1 cm from lead shielding surrounding sides	0.3 mrad/h
1 cm beneath source cart surface	0.5 mrad/h

Table 1. Dose-rates measured at various locations around the animal irradiation.

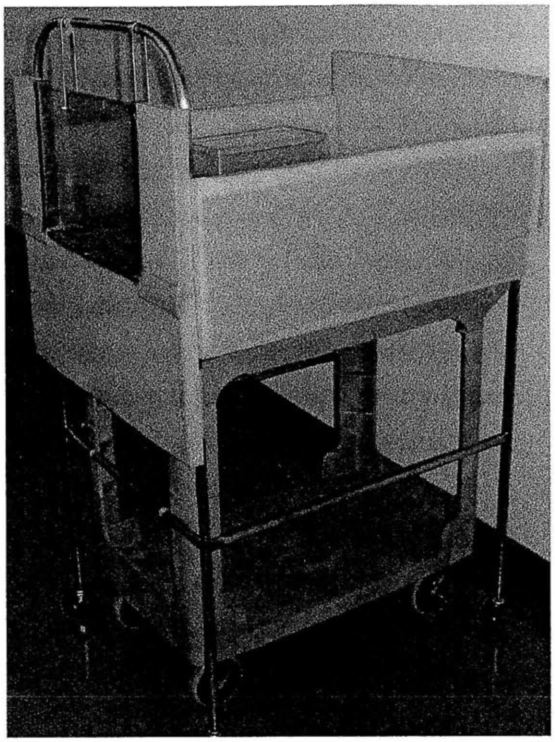

Figure 4. The animal irradiator and with shielding.

5.3 ^{241}Am Foil Configurations

With an adequate shielding apparatus constructed, it was possible to focus on the configuration of the foil sources. Several foil configurations were considered in light of the design goals presented in Section 5.2. In the following sections, four foil configurations are described along with their advantages and disadvantages relative to these goals.

5.3.1 Method of Measuring Animal Irradiator Dose-rates

In order to determine the best estimate of the dose delivered to animals by the animal irradiator, a method of measuring dose across the area of the animal platform was devised. This method utilizes 35 dose measurements across the platform to provide an estimate of the dose delivered across the platform. A similar method of measuring dose-rate inside animal cages utilizing 24 dose measurements was also devised. These methods are reported in the sections below.

5.3.1.1 Dose measurements at the surface of the animal platform

Dose-rates at the surface of the animal platform were measured using the Landauer nanodot dosimetry system discussed in detail in Chapter 3. Thirty-five nanodot dosimeters were annealed in sunlight so that the residual doses read from these dosimeters was less than 0.02 cGy. Each dosimeter was read three times in order to measure the uncertainty in the residual dose.

These dosimeters were then attached to strips of color-coded tape and taped to the surface of the animal platform at several points of interest. These points are shown in Figure 5.

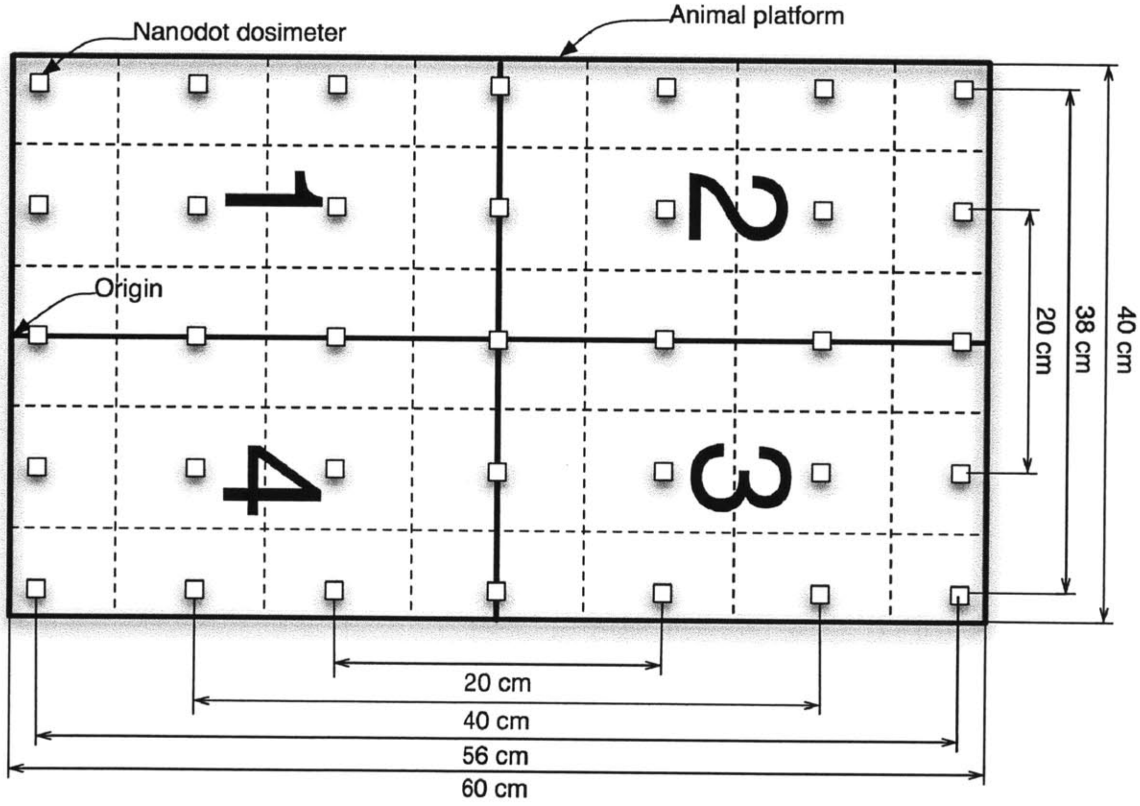

Figure 5. Placement of dosimeters for measurements on the the animal platform.

Since all source configurations are symmetrical about the center of the platform in both directions, the use of dosimeters across the entire platform provides redundancy which reduces uncertainty when calculating the mean dose delivered across the platform. These uncertainty calculations are presented in Section 5.3.1.4.

These dosimeter locations were chosen based on the dimensions of the standard animal cages to be used with the animal irradiator. With four animal cages aligned in the pattern shown above, the extent of the base of the cages is 56 cm. In the other dimension, the extent of the base of the cages is 36 cm. These measurements are described in Figure 5. Since the animals being irradiated will be limited to these ranges, dosimeters were placed only within the area defined by these distance measurements as shown in Figure 6.

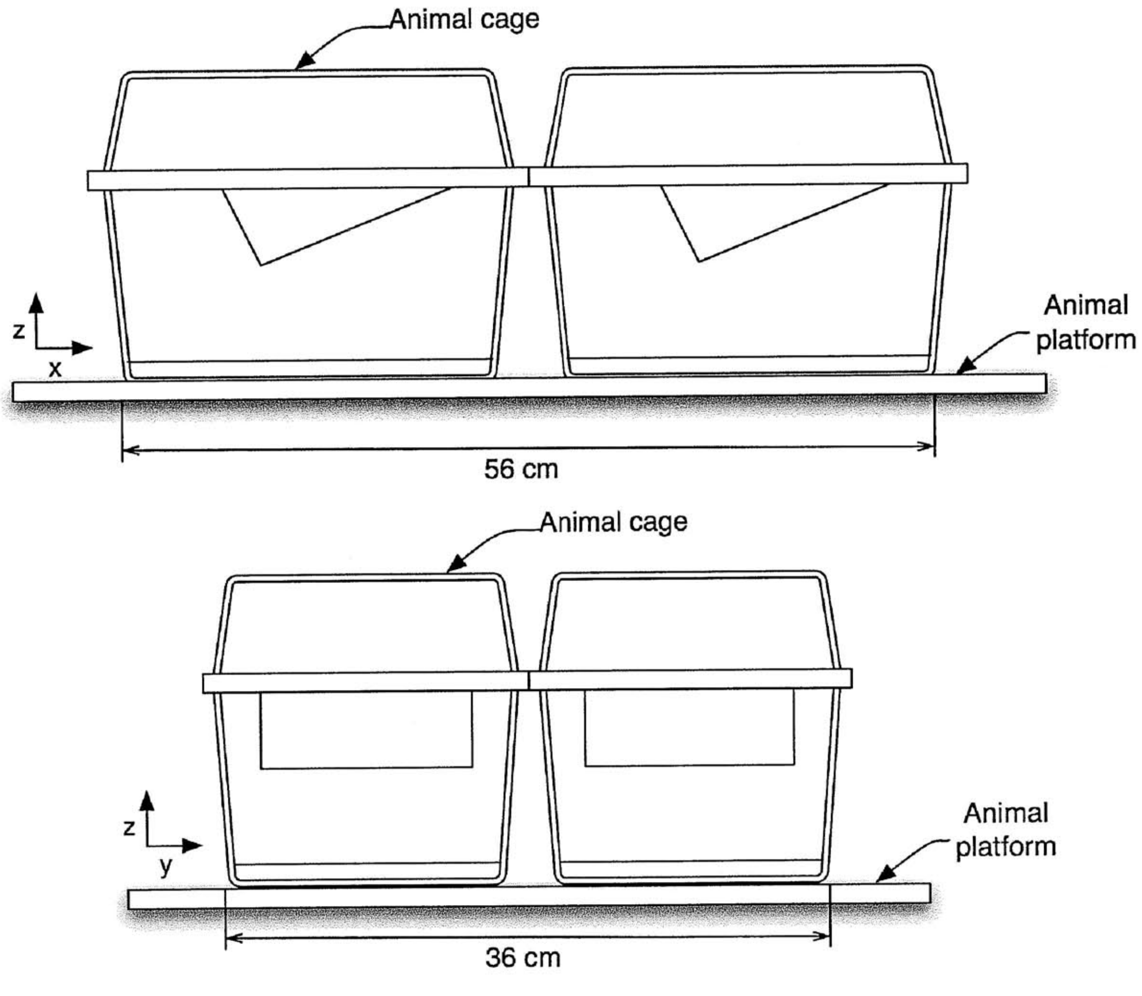

Figure 6. Dimensions of standard animal cages to be used with the animal irradiator.

After dosimeters were in place, ^{241}Am foils were placed on the source platform in one of several configurations described below in Section 5.3.3. The source platform was then rolled beneath the animal platform and aligned to insure centered placement.

After exposure the source platform was rolled away and the sources were stored in a lead storage container. The dosimeters were then read three times using the Microstar reader. These data were corrected for photon energy spectrum using the method of Section 5.3.1.3. The data were processed and analyzed using the methods presented in Section 5.3.2.

5.3.1.2 Dose measurements inside animal cages on the animal platform

Dose delivered inside animal cages were measured by a method similar to that described in Section 5.3.1.1. Nanodot dosimeters were annealed in sunlight and read with the Microstar reader. Animal cages were filled with wood chip bedding material which was 1 ± 0.1 cm thick and placed on the animal platform. Twenty-four nanodot dosimeters with residual dose measurements less than 0.02 cGy were placed inside four animal cages at six locations in each cage as described in Figure 7.

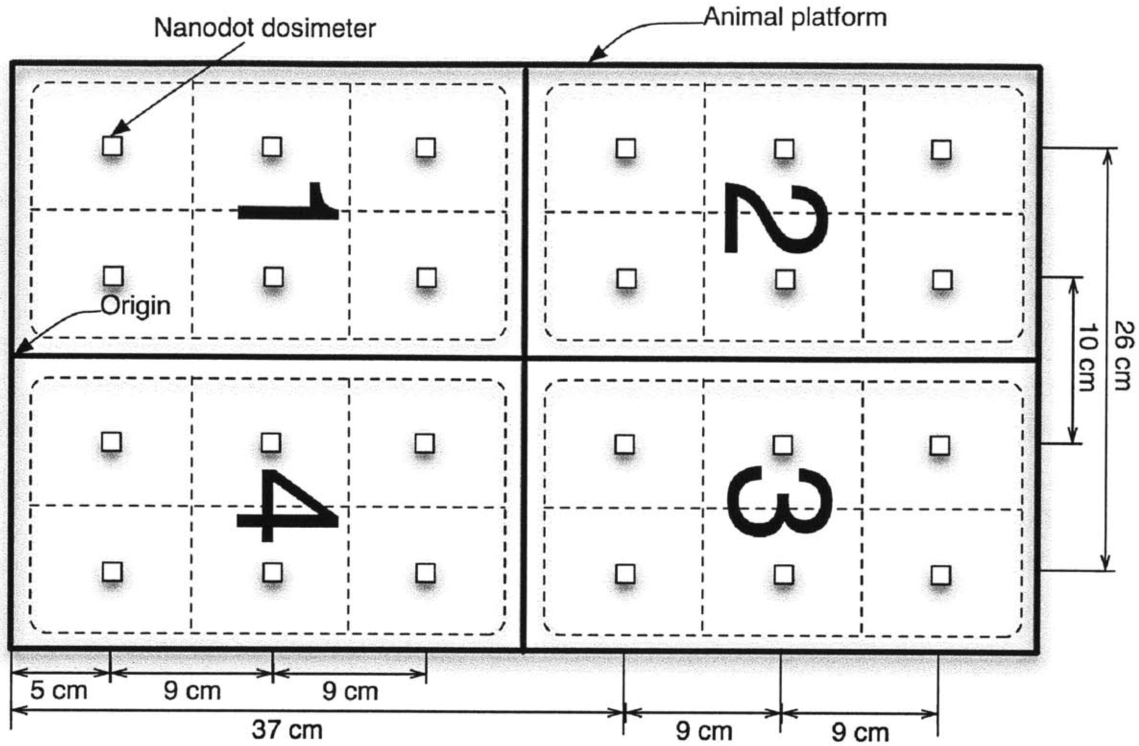

Figure 7. Placement of dosimeters for measurement of dose inside animal cages.

After exposure the accumulated dose was read from each dosimeter with the Microstar reader three times. These dose data were then corrected for photon energy spectrum using the methods of Section 5.3.1.3. These data are presented below in Section 5.3.3.

5.3.1.3 Measurement of the photon spectrum for correction of dose measurements

As discussed in Chapter 3, the nanodot dosimetry system underreports dose delivered by photons of energy less than 60 keV. In order to determine the best estimate of the dose delivered by the animal irradiator using the Landauer nanodot dosimetry system, correction factors were determined for dose measurements using measurements of the photon spectrum above the animal irradiator.

Measurements were performed using the Amptek X123 spectrometer described in Chapter 2. For each foil configuration described below in Section 5.3.3 the photon energy spectrum was measured at the center of the animal platform.

Energy spectra were measured above the animal platform surface without an animal cage and also with an animal cage with bedding inside. These measurements were used to generate correction factors using the method presented in Chapter 3, Section 3.3.5. These correction factors were 1.15 for measurements on the animal platform and 1.13 for measurements within the animal cages.

5.3.1.4 Determination of uncertainty of animal irradiator dose measurements

In Chapter 3 Section 3.3.3.3, the uncertainty of a measurement of the dose delivered by the ^{241}Am foils is discussed. The measurements discussed in that section were performed with three nanodot dosimeters measuring the dose at the same point in space. For the animal irradiator, 24 or 35 dosimeters were placed over a wider area in order to determine dose.

In order to discuss the uncertainty in these measurements it is important to consider the impact of the uncertainty on experimental parameters of interest. One important quantity for any experiment with the animal irradiator is the total dose delivered to an animal during an experiment. Since an animal is assumed to travel about randomly during the period of an irradiation and cages will be rotated clockwise on the platform weekly, the total dose delivered during the course of an experiment is then the mean dose over the area of the animal cages. The uncertainty in this mean dose is determined by combining the uncertainties of all the individual measurements across the animal platform according to the Law of Error Propagation. In this case, the uncertainty in the mean dose Δ_D is related to the mean dose, $\overline{D}$, and uncertainties of the individual dose measurements, ΔD_i as in Equation 1.

$$\Delta_D = \frac{\overline{D}}{n}\sqrt{\sum_{i=1}^{n}\left(\frac{1}{\Delta D_i}\right)^2} \qquad (1)$$

Another important quantity for any experiment with the animal irradiator is the dose-rate at which radiation is delivered to the animal. If dose-rates across the platform are not consistent, then an animal will receive radiation dose at varying dose-rates as it travels around a cage. For this reason, the dispersion in the dose data across the animal platform are also of interest. The uncertainty in the dose-rate is then calculated using the standard deviation of the dose measurements made across the platform.

In the sections below, mean dose data are reported with an uncertainty calculated as in Equation 1 and mean dose-rate data are reported with an uncertainty equal to the standard deviation of those measurements used to calculate the mean.

These uncertainties are combined with the uncertainty due to dosimeter calibration, ΔC, as described in Chapter 3, Section 3.3.3.3. The total uncertainties reported for dose data are calculated as in Equation 2 with C equal to the calibration correction factor:

$$\Delta D = \sqrt{(D\Delta C)^2 + (C\Delta_D)^2} \qquad (2)$$

For dose-rate data the total uncertainties reported are calculated as in Equation 3 with σ_D the standard deviation of those measurements divided by the time of exposure, R being the mean dose-rate calculated, and ΔR the uncertainty in this mean dose-rate of those measurements:

$$\Delta R = \sqrt{(R\Delta C)^2 + (C\sigma_D)^2} \qquad (3)$$

5.3.2 Quantities for Comparison of Source Configurations

In order to compare the different ^{241}Am foil configurations designed and presented below, it was useful to define some quantitative properties of these designs which would impact animal experiments conducted using these configurations.

The goal of these dose and dose-rate comparisons is to provide an estimation of the source of the uncertainty in dose-rate based on variation of the dose-rate across the surface of the platform. For this purpose, several quantities were calculated for each ^{241}Am configuration.

Since some variation in the dose-rate across the animal platform was observed for every configuration as described below in Section 5.3.3, it was necessary to implement a method of diminishing the effects of these variations. A cage rotation protocol has been designed by Olipitz et al. [2] in order to insure that any variations in dose-rates between cages would be corrected over a long-term experiment. According to this protocol, cages are to be rotated clockwise around the animal platform once a week.

Under this cage rotation protocol, an animal walking randomly within a cage will spend an equal amount of time in every location of the platform for a long experiment (3 months or more as in previous work [2]). With this approximation, the total dose delivered to an individual animal is the mean dose delivered over the entire animal platform. For each foil configuration, the mean dose data for one hour of exposure are reported in Section 5.3.4 below. This approximation also yields the mean dose-rate during the experiment, which is the total dose divided by the time of the experiment. Mean dose-rate data are reported in units of cGy/h in Section 5.3.3 and 5.3.4 below.

Comparing the dose data between different regions of the animal platform is useful in determining the source of uncertainty in dose-rate. For each axis, calculations were performed comparing the dose along the edges of the platform compared to the dose in the center of the platform. For the animal platform surface dose measurements, these comparisons are the ratio of the mean edge dose to center dose along each axis. These ratios are defined in Equations 4 and 5 where $D_{y=-18,18}$ represents the set of dose data measured at points on the animal platform with y=-18 or y=18, $D_{y=0}$ represents the set of dose data measured at points with y=0, with the coordinate system described in Figure 5.

$$R_y = \frac{\langle D_{y=-18,18} \rangle}{\langle D_{y=0} \rangle} \tag{4}$$

$$R_x = \frac{\langle D_{x=2,58} \rangle}{\langle D_{x=30} \rangle} \tag{5}$$

The mean of all set dose data quantities presented here was area-weighted such that the area of the animal platform and animal cages was divided and only the area closest to any dose measurement was used during weighting. This division of the area of the animal platform and animal cages is described by the dashed lines in Figures 5 and 7. For the dose data from the corners of the animal platform, the area weighting was 36 cm^2, and the area weighting for dose data from the center of the animal platform was 100 cm^2. The full table of area weighting factors for all dose data is described in Appendix 1. For the animal cage dose data, the dose data from the cage corners had an area weighting of 71.5 cm^2. All other dose data had an area weighting of 72 cm^2.

5.3.3 Comparison of Four ^{241}Am Foil Configurations

In order to meet the design goals for the ^{241}Am animal irradiators, several foil configurations were considered. Mean dose, dose consistency, and utilization of materials were different for each foil configuration. The following sections describe these differences and their impact on potential experiments.

5.3.3.1 Single ^{241}Am Foil Configuration

While some animal irradiation experiments may require dose-rates of 0.5 cGy/h, some experiments may require lower dose-rates. For example, Olipitz [2] discusses the effects of dose-rates of 0.0126-0.126 cGy/h on mice. In order to minimize the use of ^{241}Am foils and maximize the number of cages of animals that could be simultaneously irradiated in such experiments at lower dose-rates, a single foil configuration was designed and measured. This configuration allows for 124 animal cages to be irradiated simultaneously with the number of foils currently available.

One ^{241}Am foil source was positioned on the source platform with its center 13 cm below the animal platform as pictured in Figure 8. This dose-rate was measured at 35 points across the top of the animal platform according to the method presented in Section 5.3.1.1. The dose-rate measurements are shown in Figure 9. Dose-rates were also measured within animal cages on the animal platform using the method discussed in Section 5.3.1.2. These dose-rate measurements are shown in Figure 10.

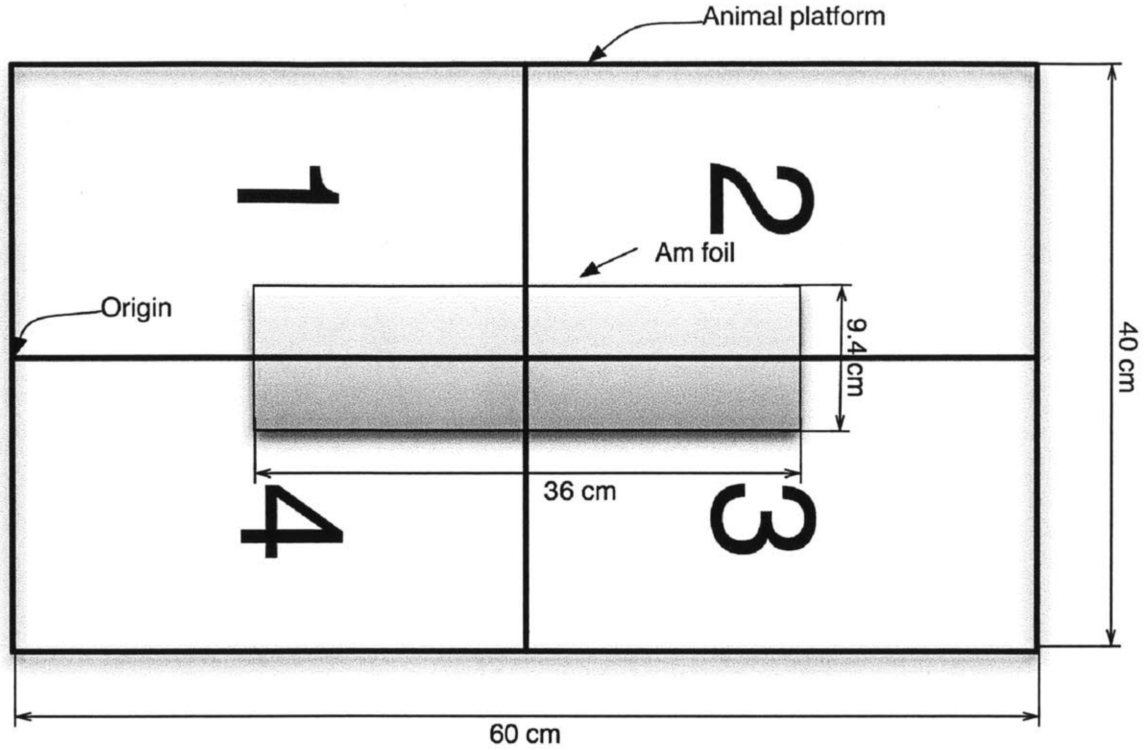

Figure 8. Irradiator configuration using a single ^{241}Am foil.

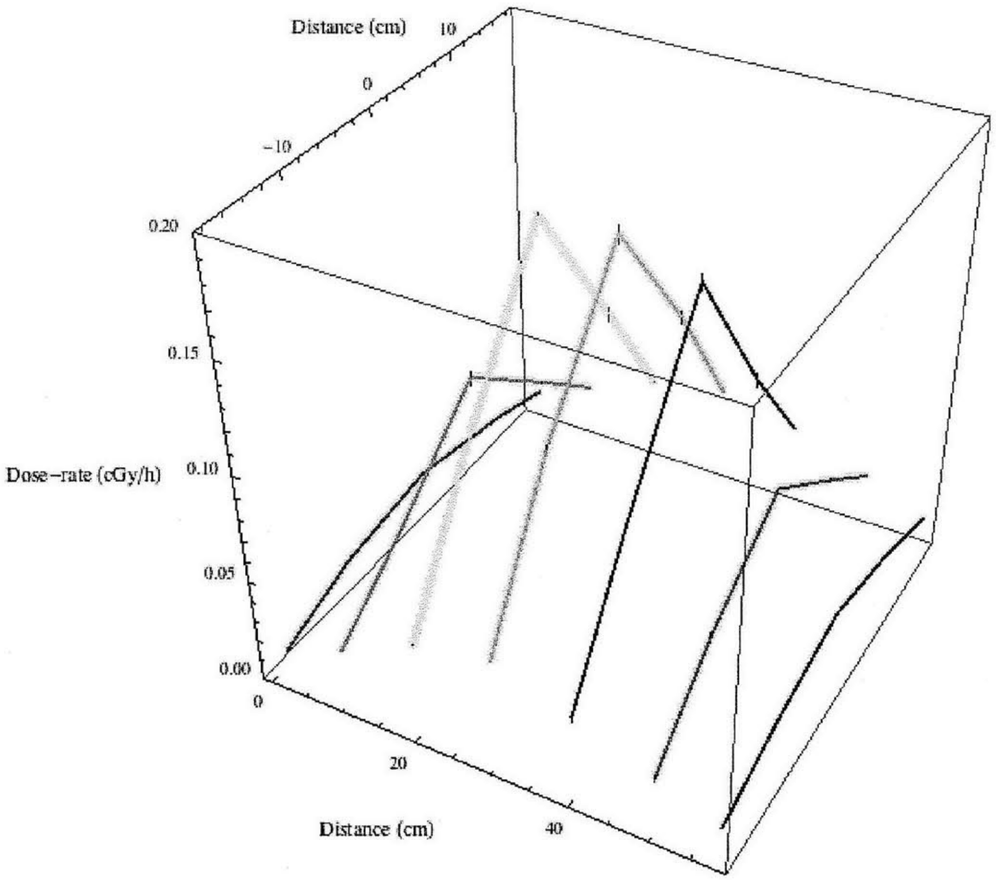

Figure 9. Dose-rate profile at the platform surface for the single ^{241}Am foil configuration.

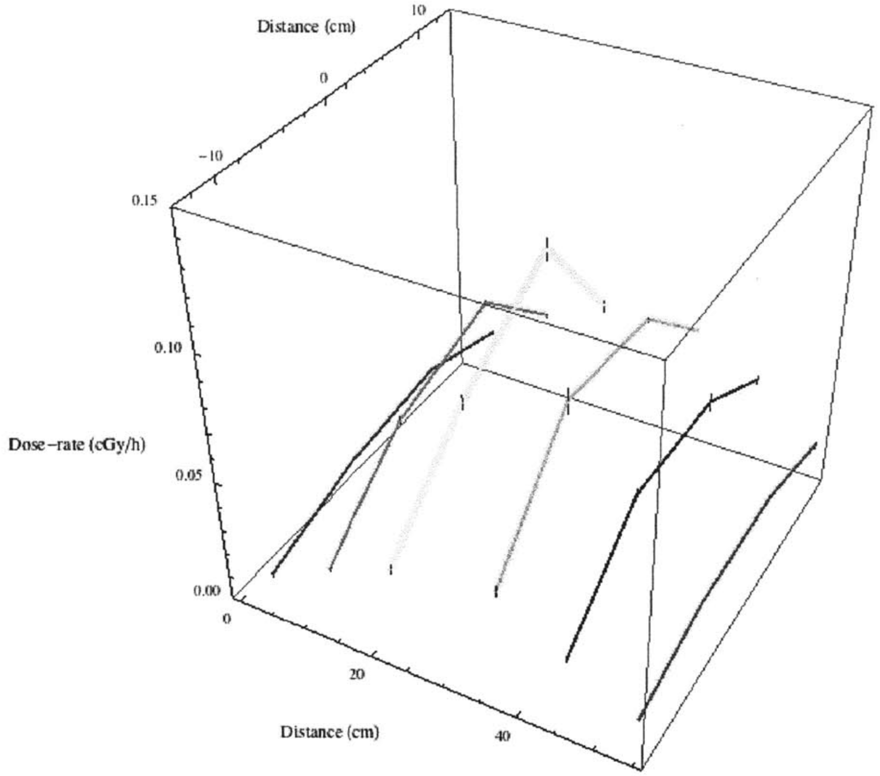

Figure 10. Dose-rate profile inside animal cages for the single ^{241}Am foil configuration.

This foil configuration results in a R_x and R_y values of 0.24 ± 0.01 and 0.28 ± 0.01 respectively, which are smaller than all other configurations considered described below in Section 5.3.3. This disadvantage of a relatively large variation in dose-rate across the platform is balanced by the advantage of minimizing the required number of foils and thus allowing more studies to be performed simultaneously with a finite number of foils available.

5.3.3.2 Configuration with Four ^{241}Am Foils

In order to achieve a more consistent dose profile than possible with a single foil configuration described in Section 5.3.3.1 while also minimizing the number of foils required, a four foil configuration was designed. For this configuration, four ^{241}Am foils were placed 13 cm below the animal platform in the pattern described by Figure 11.

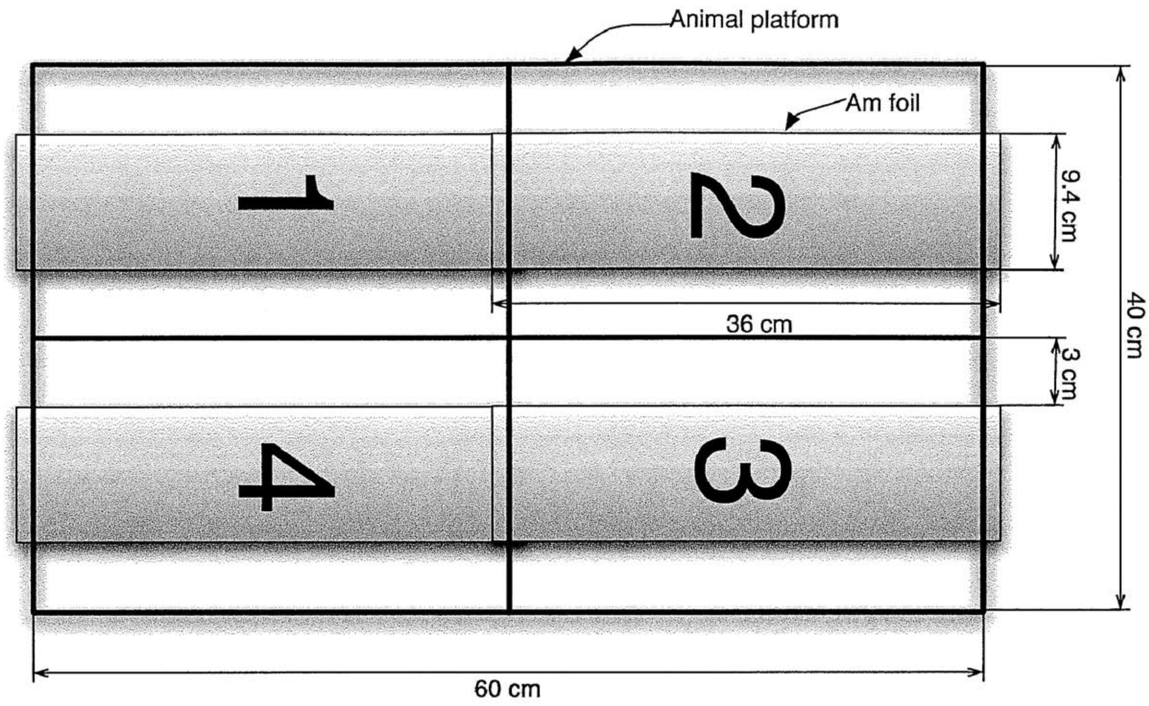

Figure 11. Irradiator configuration using four ^{241}Am foils.

For this configuration there is greater consistency in dose-rate between the center of the animal platform and the edges than with the single foil configuration. This consistency can be seen most clearly by comparing the ratio of dose-rates between the center and edge of the platform along longest axis of the platform. These comparisons are presented below in Section 5.3.4. The dose profile for this configuration is shown in Figure 12. The dose profile was also measured within animal cages on the animal platform. These dose data are shown in Figure 13.

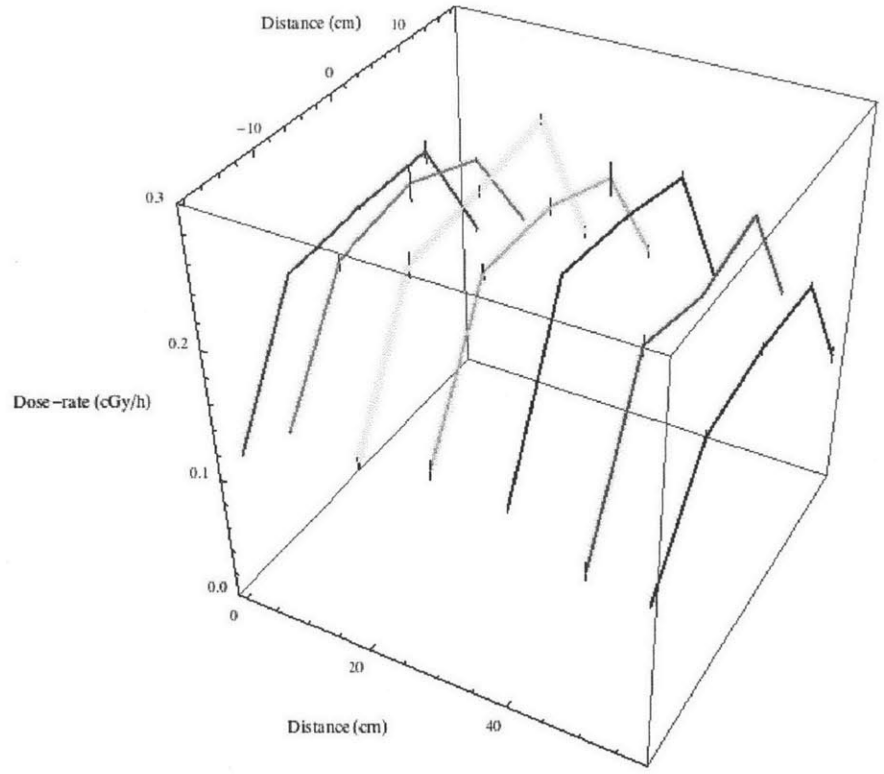

Figure 12. Dose-rate profile at the platform surface for the four ^{241}Am foil configuration.

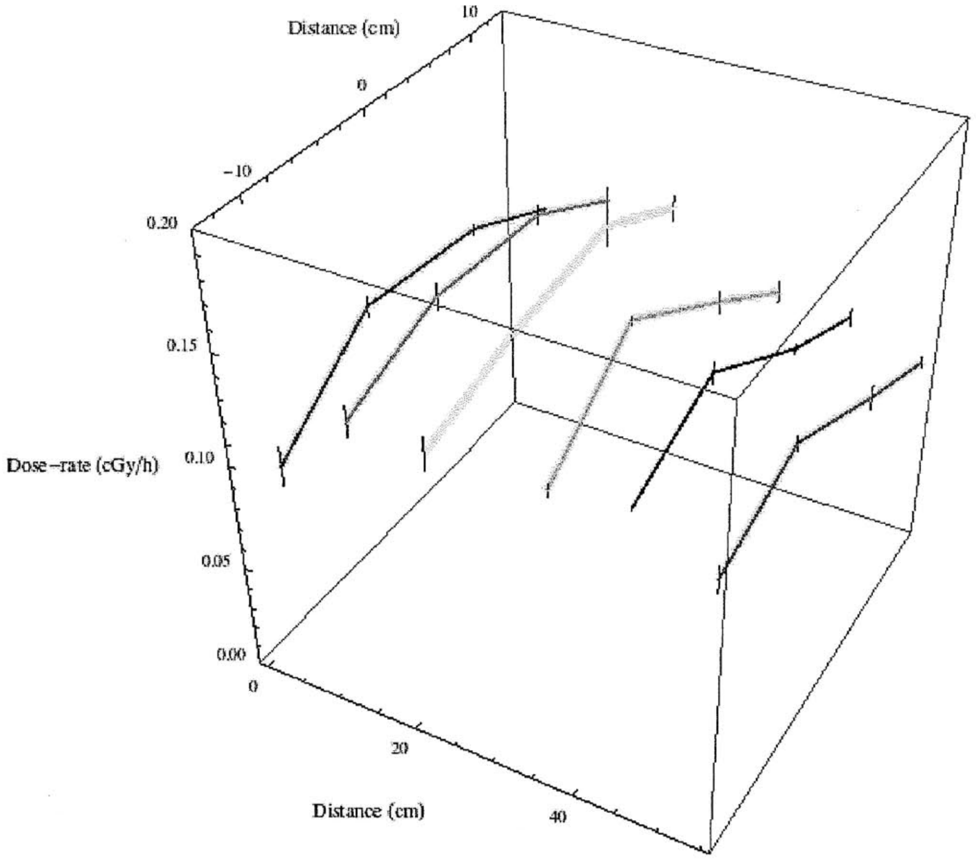

Figure 13. Dose-rate profile inside animal cages for the four ^{241}Am foil configuration.

This configuration provides a mean dose of 0.22 ± 0.01 cGy in one hour and R_x and R_y values of 0.82 ± 0.01 and 0.59 ± 0.02 respectively. This provides improved consistency a greater dose-rate relative to the one foil configuration, while providing for 24 animal cages to be simultaneously irradiated with the number of foils currently available.

5.3.3.3 Configuration with Nine ^{241}Am Foils

For animal irradiations which require higher dose-rates than possible with one or four foils, a configuration with nine ^{241}Am foils was designed. In this configuration, nine foils were aligned 4.5 cm below the animal platform in the pattern shown in Figure 14.

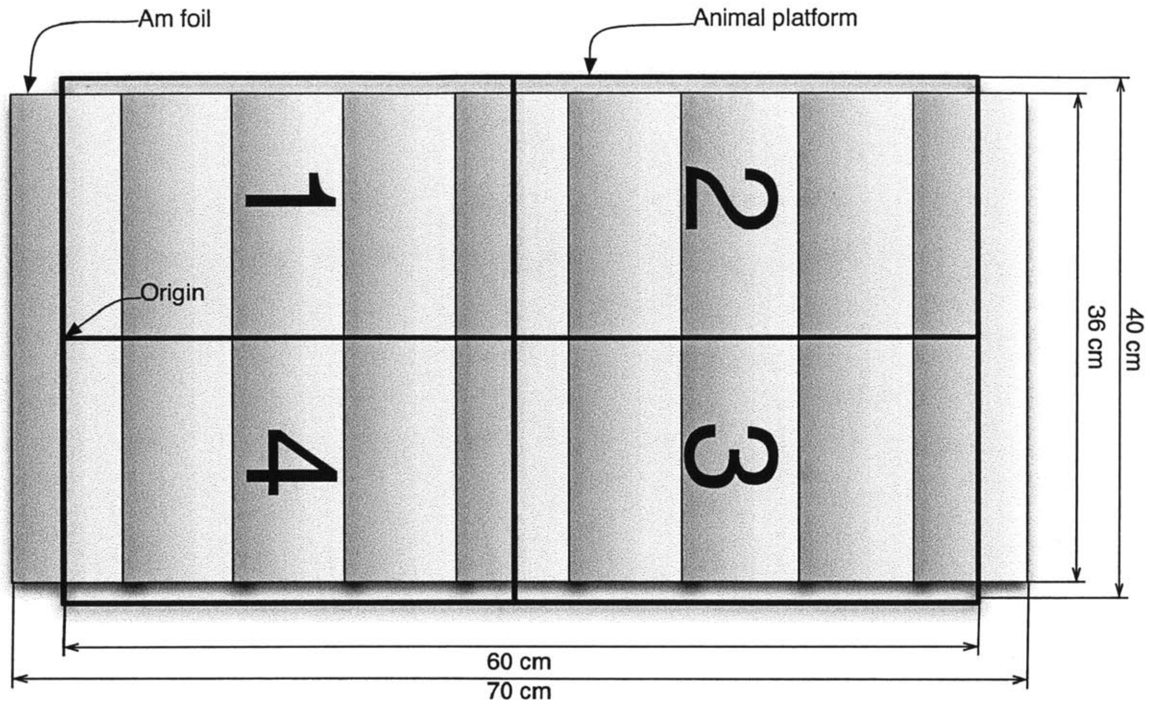

Figure 14. Diagram of the animal irradiator configuration with nine ^{241}Am foils.

The dose-rate profile at the surface of the platform for this configuration is shown in Figure 15. The dose-rate profile inside animal cages is shown in Figure 16.

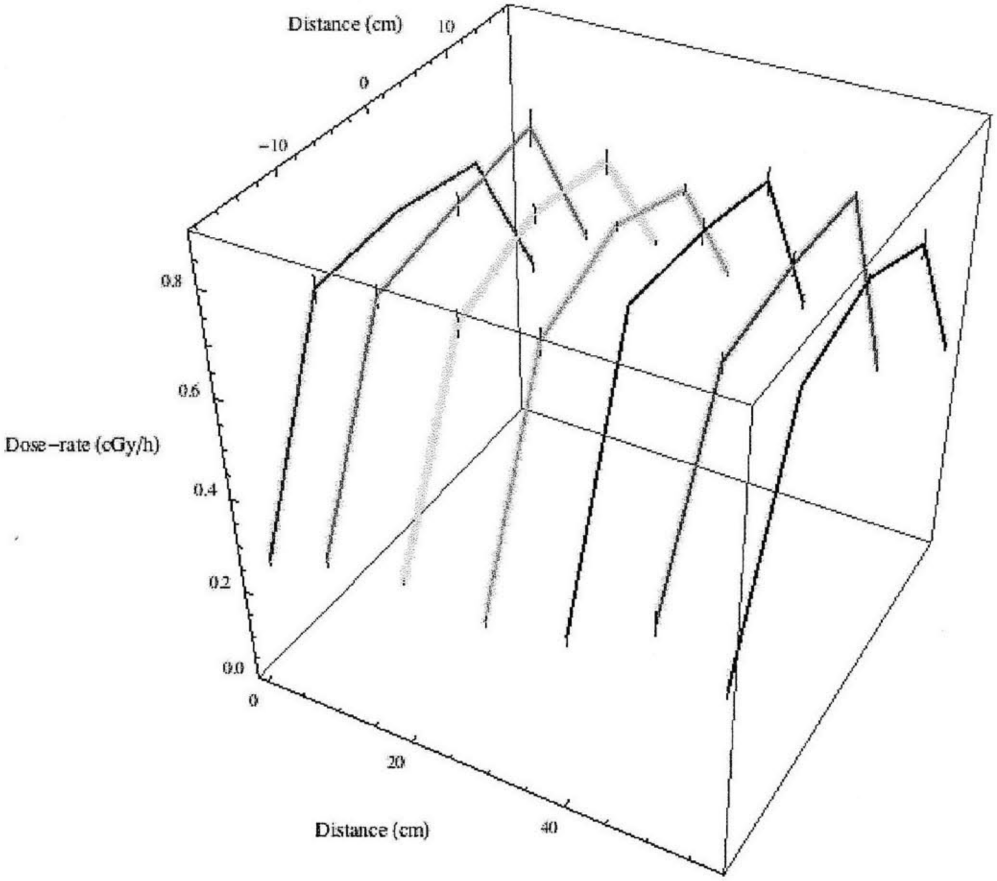

Figure 15. Dose-rate profile at the platform surface for the nine foil ^{241}Am animal irradiator configuration.

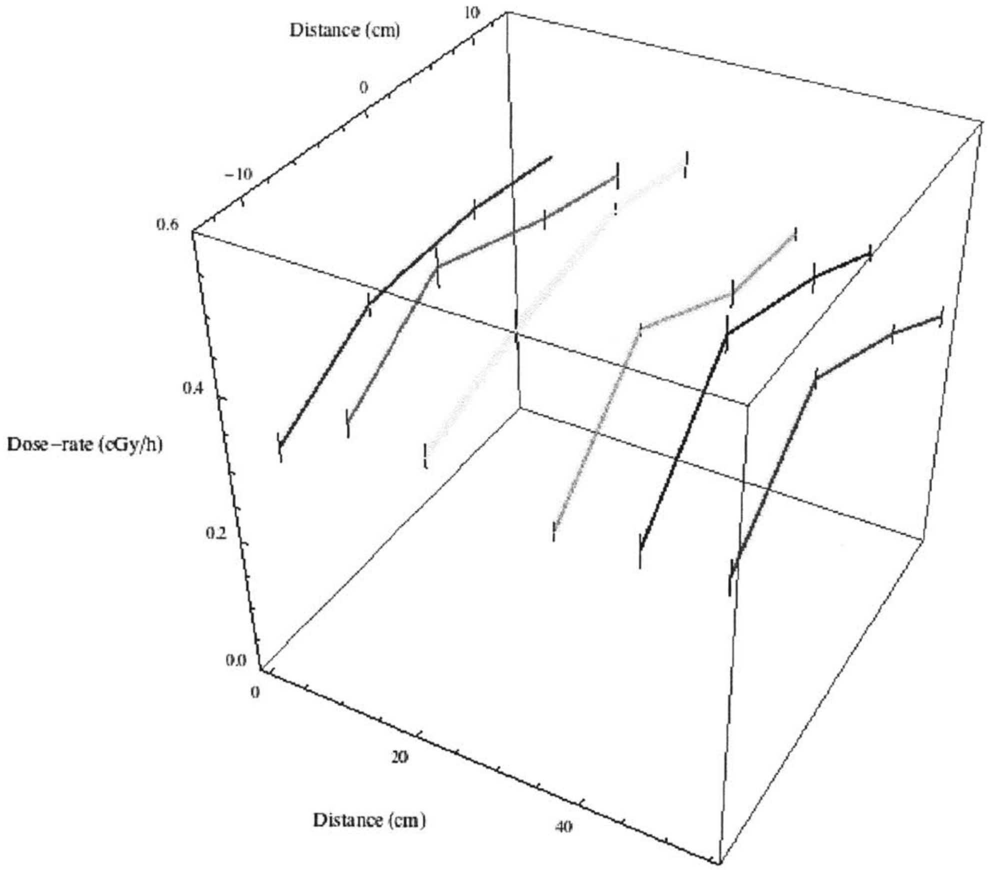

Figure 16. Dose-rate profile inside animal cages for the nine foil ^{241}Am animal irradiator configuration.

This configuration provides a mean dose of 0.66 ± 0.04 cGy in one hour and R_x and R_y values of 0.97 ± 0.01 and 0.51 ± 0.02 respectively. With this configuration a total of 12 animal cages may be irradiated simultaneously with the number of foils currently available.

5.3.3.4 Configuration with Twelve ^{241}Am Foils

In order to maximize the dose-rate to the animal platform, an irradiator configuration with twelve foils was designed. The combined area of twelve foils (4060 cm^2) is greater than the area of the animal platform (2400 cm^2), leaving a region of overlap as shown in Figure 17. For this design the foils were placed on an irradiator platform 4.5 cm below the animal platform. The dose-rate profile at the surface of the platform for this configuration is shown in Figure 18. The dose-rate profile inside animal cages is shown in Figure 19.

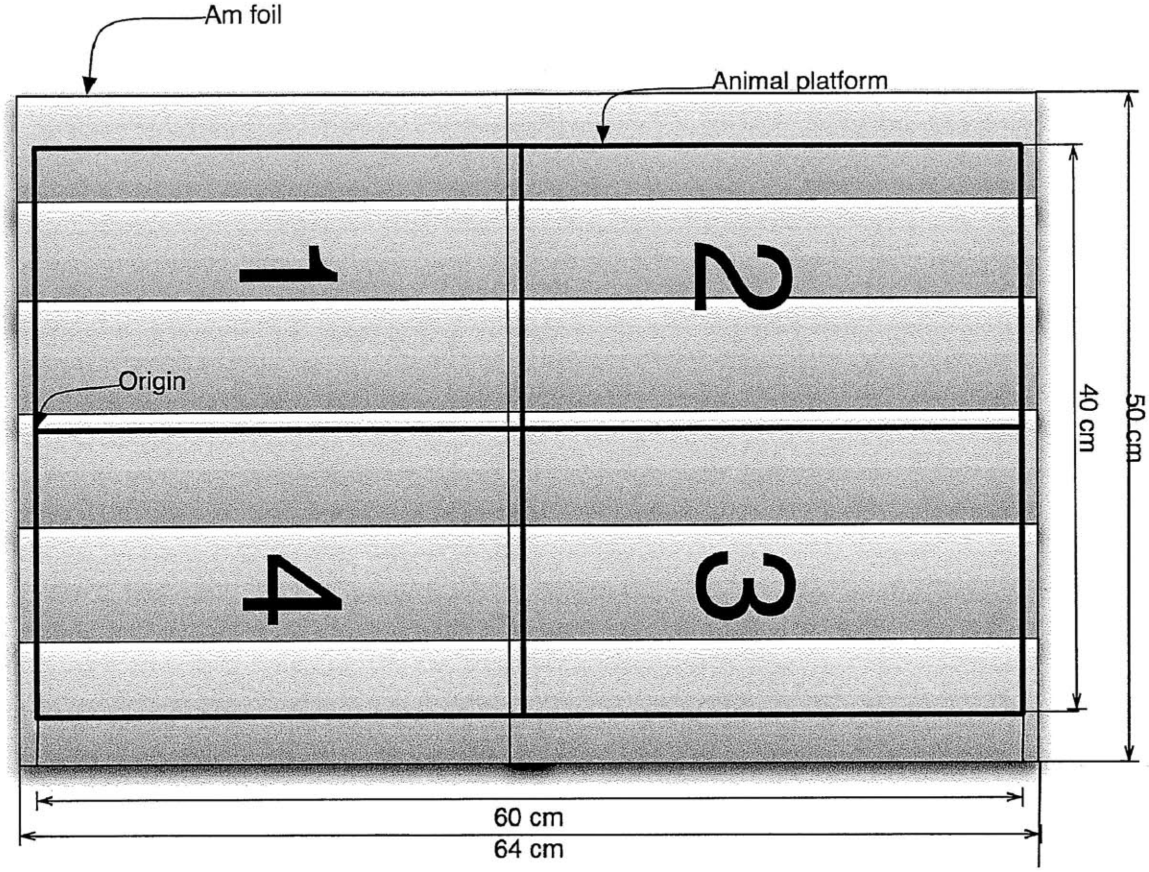

Figure 17. Dose-rate profile for the animal irradiator configuration with twelve ^{241}Am foils.

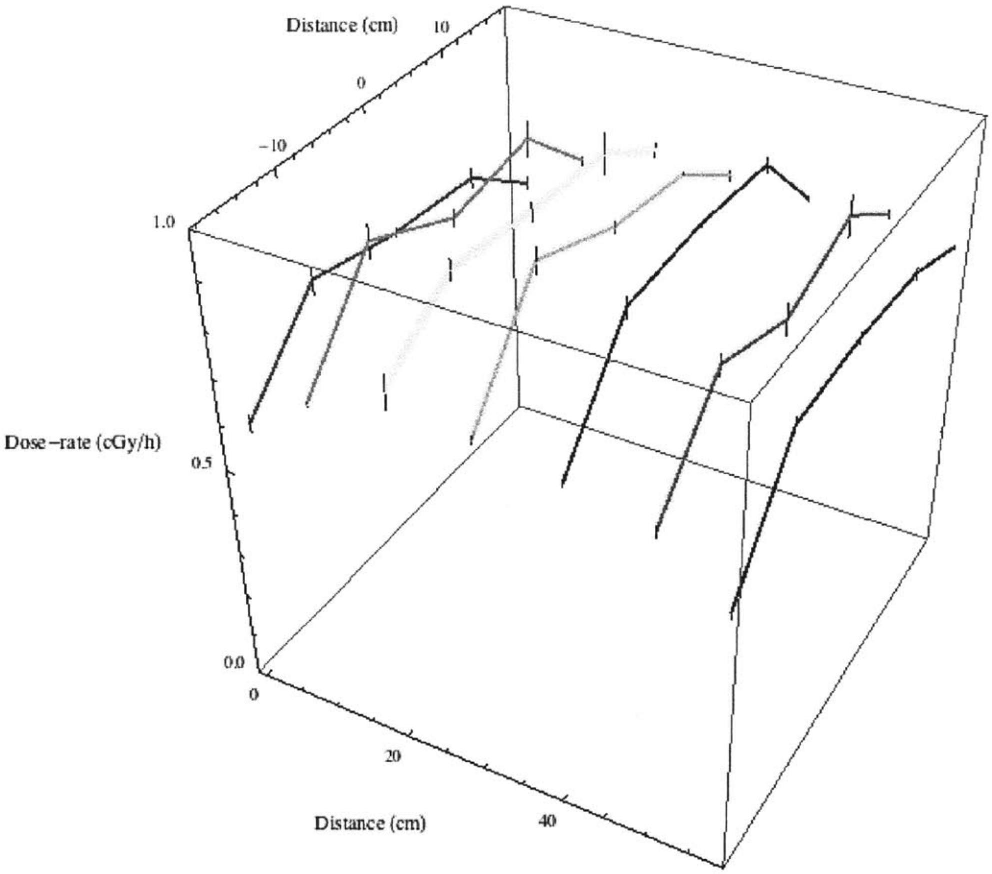

Figure 18. Dose-rate profile at the platform surface for the twelve foil ^{241}Am animal irradiator configuration.

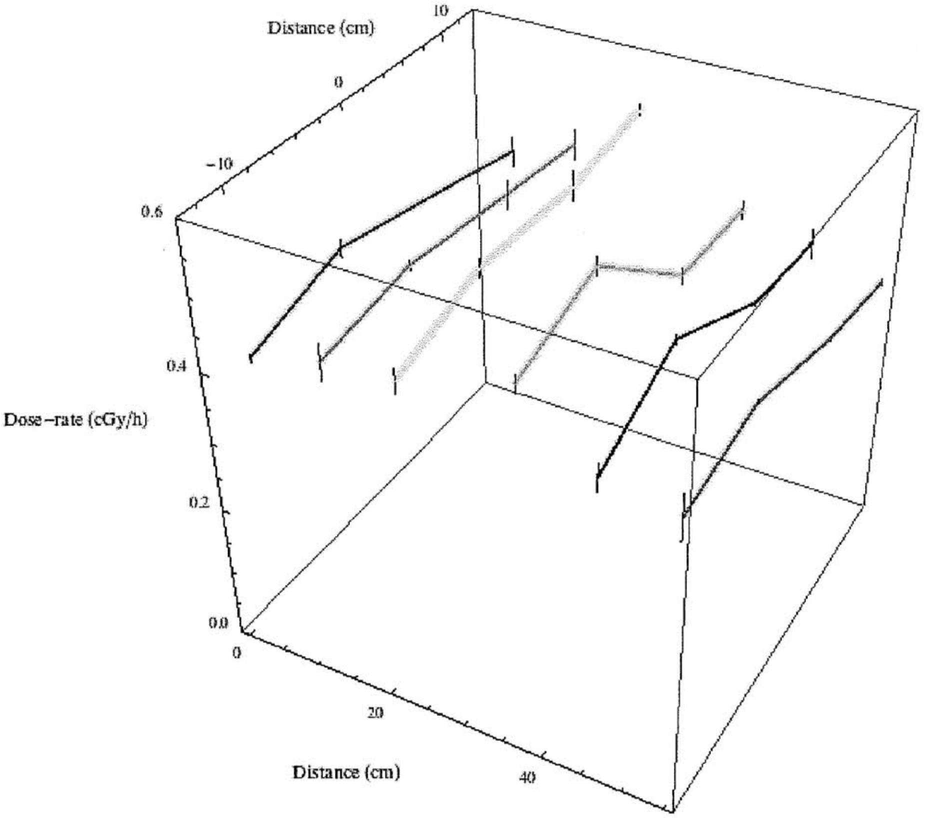

Figure 19. Dose-rate profile inside animal cages for the twelve foil ^{241}Am animal irradiator configuration.

This configuration provides a mean dose of 0.82 ± 0.06 cGy in one hour and R_x and R_y values of 0.85 ± 0.01 and 0.85 ± 0.02 respectively. With this configuration a total of 8 animal cages may be irradiated simultaneously with the number of foils currently available.

5.3.4 Comparisons of Foil Configurations

In order to compare the foil configurations for the purposes of meeting the design goals presented in Section 5.2, several quantities were calculated for each foil configuration. These quantities are described in detail 5.3.2. For each foil configuration, the ratios of dose along the sides of the platform to the dose along the center of the platform are reported for both directions. These quantities are labeled R_x and R_y, with x denoting the side 40 cm in length and y the side 60 cm in length. These ratios are reported in Table 2 along with mean dose and standard deviation of dose measurements across the surface of the animal platform for each foil configuration. All data in Table 2 are reported in terms of dose during a one hour time interval.

Number of Foils	Mean Dose on Platform (cGy)	±	Standard Deviation of Dose (cGy)	Mean Dose in Cages (cGy)	±	R_x on Platform	±	R_y on Platform	±	Number of Cages
1	0.075	0.023	0.05	0.046	0.002	0.24	0.01	0.28	0.01	124
4	0.22	0.01	0.05	0.13	0.01	0.82	0.03	0.59	0.02	24
9	0.66	0.04	0.18	0.43	0.03	0.97	0.03	0.51	0.02	12
12	0.82	0.06	0.09	0.50	0.03	0.85	0.02	0.85	0.02	8

Table 2. A comparison dose measurements for a one hour period for the different foil configurations.

In order to maximize total dose and dose consistency, the twelve foil configuration is the obvious choice. Only eight cages can be irradiated at one time with this configuration with the current number of ^{241}Am foils, so this configuration may not be practical for all experiments. Other foil configurations have also been evaluated which allow for 12, 24, and 124 cages to be irradiated concurrently.

Together with the shielding configuration described above, these foil configurations provide an apparatus for safely irradiating animals for long periods of time without the need for a dedicated facility, constantly operating x-ray tubes, or refilling of liquid source phantoms. These advantages make the ^{241}Am irradiators well suited for long term animal irradiation experiments.

5.4 References

1.NRC, "Radiation dose limits for individual members of the public", NRC Regulations 20.1301, Nuclear Regulatory Commission.
2. W. Olipitz, S. Hembrador, M. Davidson, J. Yanch, and B. Engelward, Health Physics, 98, 5, 2010, 727-734.
3. J.H. Hubbell and S.M. Seltzer, Tables of X-Ray Mass Attenuation Coefficients and Mass Energy-Absorption Coefficients, NISTIR 5632, National Institute of Standards and Technology.

Chapter 6: A Model for Projecting Biological Effectiveness of Ionizing Radiation at Dose-rates Less than 1 cGy/h

Relative biological effectiveness (RBE) is defined as the ratio of doses of two radiation fields required to produce the same biological effect. RBE was first defined to compare the effects of acute doses of radiation, but RBE has also been used to compare the effects of low dose-rate fields. RBE can be used to predict the relative biological effects of two fields, but since RBE is well known to vary with dose-rate it is important to account for this when predicting the relative effects of two fields. For example an RBE measurement made at a dose-rate of 1 Gy/min cannot not generally be used to determine RBE at 1 cGy/h.

In previous chapters RBE was determined experimentally for two fields at a dose-rate of 0.28 ± 0.02 cGy/h. In this chapter it is demonstrated how the measurements of cell survival at this dose-rate can be applied to predict the relative effects of these fields at lesser dose-rates. A method for calculating the maximum dose-rate at which the results of a cell survival assay can be used to predict RBE for dose-rates less than 1 cGy/h is also presented.

This method provides the ability to predict RBE for low dose-rates based on the results of biological experiments conducted at greater dose-rates (1-30 cGy/h). This differentiates the method from other methods for determining RBE using field energy characteristics and quality factors (as discussed in Chapter 4) or biological experiments conducted at acute dose-rates. The method provides several advantages over these approaches.

In this chapter the established methods for determining RBE and their limitations will be discussed. The underlying assumptions and limitations of this new method for determining RBE for dose-rates $<$ 1 cGy/h are also discussed.

6.1 Previous Work in Modeling RBE and Determining the Probabilities of Single Traversal Damage

RBE may be measured for two fields using experimental results for those fields, or it may be estimated based the results of other biological and/or physical data. As discussed in Chapter 4, RBE has been estimated based on the linear energy transfer characteristics of the radiation fields in question along with the quality factors for corresponding values of linear energy transfer as determined by the ICRP [27]. By weighting the frequency spectrum of linear energy transfer for a field by these quality factors, an estimate of RBE is found.

These quality factors are determined using RBE measurements from many separate experiments with different radiation fields. Any estimate of RBE based on these quality factors is then dependent on the accuracy of these quality factors and the assumption that the fields, cell lines, and assays used to determine these quality factors are suitable substitutes for the actual conditions for which RBE is being determined.

The ICRP has recommended that these quality factors not be assumed to provide an accurate description of the relative effects of different fields for these reasons [27]. According to the commission, the use of this method provides only a rough estimate of the relative effects of two fields with different linear energy transfer characteristics.

Many of the RBE measurements used to determine these quality factors were found for acute exposures of <1 Gy, using the initial slopes of dose-effect curves. This approach was chosen to avoid the dependence of the RBE on dose-squared at greater doses. This assumption that initial slopes of dose-effect curves at acute dose-rates are good predictions of dose-effect at low dose-rates is problematic due to observations that the initial slopes of dose-effect curves do not always predict the dose-effect relationship at low dose-rates. For example, Peacock et al. discuss cell survival curves from exposures at acute and low dose-rates to demonstrate that the initial slopes at acute dose-rates may vary greatly from the slopes at low dose-rates in some cases [14].

The method of using quality factors for determining RBE at low dose-rates requires assumptions that data from exposures with fields with different energy spectra at acute dose-rates can be used to directly determine RBE at low dose-rates. The model presented in this chapter demonstrates that these assumptions are not necessary for RBE measurements made with chronic exposures below a certain dose-rate. The model presented in this chapter allows for the use of low dose-rate biological data to project RBE at dose-rates at which biological effects may not be observable. A method for determining RBE at dose-rates <1 cGy/h for the actual energy spectra in question using biological data from exposures to the same fields at elevated dose-rates is also discussed in Section 6.7.

6.2 Previous Work Determining Dose-effect Relationships Using Biological Data from Low Dose-rate Data Exposures

Many measurements of RBE based on exposures at low dose-rates have been published. Below some dose-rate some biological effects become impossible or difficult to observe, and the dose-effect relationship cannot be observed. Attempts to determine a general value of RBE at low dose-rates based on an average of RBE values found at several low dose-rates have been published. For example Nath et al. describe the low dose-rate RBE for ^{125}I and ^{103}Pd using an average of the RBE values found for several dose-rates in the range 6-30 cGy/h [12].

However this approach does not account for the possible differences in the probabilities of multiple traversal damage (damage due to a combination of instances of energy deposition separated in time) for each field. If these probabilities are different, this would affect the RBE estimate made by averaging any dataset from exposures at more than one dose-rate. The method described in Section 6.7 provides a means of avoiding the effects of multiple traversal damage on RBE calculations.

Ruiz de Almodovar et al. discuss a method of determining the dose-rate below which irreparable damage due to multiple traversals is negligible using the shape of cell survival curves [26]. The study suggests that this threshold dose-rate is the point at which there is no apparent dependence on dose-squared in the cell survival curve. However the shape of cell survival curves cannot be relied on to provide information about the probability of multiple traversal damage at low dose-rates. At low dose-rates, multiple traversal damage is proportional to dose, rather than dose-squared, as will be demonstrated in detail in Section 6.6.

These methods of using low dose-rate data to determine RBE and the probability of damage due to single traversals (damage due to a single instance of energy deposition) may result in inaccuracy in any RBE projection for dose-rates at which multiple traversal damage is negligible. In order to make the best possible projection of RBE at these dose-rates, it is necessary to observe RBE at some elevated dose-rate at which multiple traversal damage is also negligible.

6.3 Assumptions Underlying the Model

In order to make any estimate of biological effectiveness at dose-rates less than 1 cGy/h based on data from exposures at greater dose-rates, some assumptions about the biological effects of ionizing radiation must be made. The most essential of these assumptions is that a single radiation traversal has some probability of irreparably damaging a biological system independent of any other radiation traversals. This assumption is justified based on track structure data from Goodhead which show that single ionizing radiation traversals can induce damage to biological molecules [2].

In these track structure studies and in this model, the volume of interest is assumed the cell nucleus which contains the DNA. This assumption is justified based on experiments linking observations of DNA damage to other biological effects. While ionizing radiation may damage mitochondrial DNA and other systems of the cell, redundancy of these systems makes damage to them less important in determining biological effects than damage to the cell nucleus.

It is also assumed that this probability of a single radiation traversal inducing irreparable damage does not change greatly with dose-rate for chronic exposures. Irreparable damage caused by multiple traversals will vary greatly with dose-rate, as repair probabilities change with the time delay between traversals. However there is no reason based on physics alone to expect that this probability of irreparable damage induction by a single radiation traversal is influenced by other traversals separated in time. Neither the density of ionization during nor the spatial dimensions of the cell are influenced by dose-rate. Since these factors determine the probability of irreparable damage due to a single traversal, there is no physical basis to expect this probability to be influenced by dose-rate.

Some biological mechanisms, such as those described by Stecca and Gerber [3] may preemptively be activated and provide a greater protection to a cell against ionizing radiation, but these mechanisms are assumed to be active across the range of chronic dose-rates considered in this model. This ability to assume the activation of biological mechanisms for reducing the probability of single traversal damage provides one advantage of using biological data from low dose-rate exposures rather than data from acute exposures, since these mechanisms will not be activated before dose is delivered at acute dose-rates.

Even at dose-rates less than 100 cGy/h multiple traversals have some probability of inducing reparable damage which combines to induce irreparable damage. This is evidenced by the findings of Ueno et al., who observed that cell survival per unit dose varies with dose-rate across the range 12-78 cGy/h [4]. Any measurement of biological effects at a dose-rate at which there is a non-negligible probability of multiple traversal damage would not be suitable for the determination of the probability of single traversal damage. In order to define a dose-rate at which multiple traversal damage is negligible, it was first assumed that there would be a finite probability of induction of irreparable damage for any two single traversals that caused separate instances of reparable damage to be concurrently present (unrepaired) within the same cell nucleus.

Serving as a basis for this assumption are the many studies at acute dose-rates which show a response proportional to dose-squared. The extension of this dependence on dose-squared at acute dose-rates to an analogous dependence on the total dose at low dose-rate is described in 6.5. This extension serves as a basis for using the observed biological response proportional to dose-squared relative to the response proportional to dose at acute dose-rates in determining the probability of multiple traversal damage relative to single traversal damage per unit dose at low dose-rates.

The model accounts for the effects of dose-rate and repair rate on the likelihood of induction of irreparable damage by multiple traversals. In order to do this the exponential repair model described by Dale [5] and verified experimentally by Cleaver et al. [11] is assumed to describe the probability, P_{repair}, of an instance of damage being repaired at a time t after the damage occurs in terms of a repair time constant, μ.

$$P_{repair} = 1 - e^{-\mu t} \tag{1}$$

The ability of repair mechanisms to accurately repair damage varies with dose-rate as these mechanisms are overwhelmed at greater dose-rates at which the density of damage sites becomes greater. These repair mechanisms may also be less effective for densely located damage sites resulting from densely ionizing radiation, such as heavy charged particles. It has been recognized that fields with greater linear energy transfer properties produce more densely-spaced damage [13]. For this reason repair rates are assumed to be dependent on both biological and radiation field properties in this model. Different repair rates are sampled in order to determine the influence of repair rate on the proportion of damage due to single traversals, but the resulting analytical model provides for repair rates to differ based on biological and radiation field properties.

These assumptions allow the determination of a threshold dose-rate below which multiple traversal damage is negligible based on experimental data. Calculating this threshold dose-rate for two fields provides a criterion for performing biological experiments that can be used to project RBE for dose-rates less than 1 cGy/h.

6.4 Limitations of the Model

The model described in this chapter provides a means of projecting RBE values for dose-rates at which biological effects are difficult to observe based on biological data from exposures at elevated dose-rates. The model predicts the maximum dose-rate at which an RBE measurement made can be assumed to be valid for all lesser dose-rates. Once this dose-rate is determined, RBE may be determined using any biological assay preferred, and this RBE may be assumed to be a good estimate of the RBE at lesser dose-rates.

This projection is made possible due to the assumption that the relative probabilities of single traversal effects do not change with dose-rate as discussed above. However it is possible that biological mechanisms result in differences in the probabilities of single traversal effects with dose-rate. Adaptive response to radiation may result in these probabilities being lower at low dose-rates than at elevated dose-rates.

Any assumption that projects RBE at dose-rates less than 1 cGy/h must assume that these differences are not significant, or otherwise no estimate for RBE at these dose-rates is possible. This model does provide the advantage that the dose-rates from which RBE is projected do allow for the possibility of adaptive response, while acute exposures would not allow for this effect.

Any experimental determination of RBE is based on the response of some biological sample to a radiation field. Since RBE may vary with biological sample, some variation in the RBE predicted with this method may be expected. For example a determination of RBE using low dose-rate exposures of mice may not accurately predict the RBE of the same fields in humans. This is true for any method of using one biological system to determine the effects of radiation on another biological system.

6.5 Determining the Dose-rate Below which Damage Due to Multiple Traversals is Negligible

At environmental dose-rates, energy deposition traversals occur less frequently than at acute dose-rates. With repair processes correcting reparable damage, instances of reparable damage have a smaller probability of being present concurrently with decreasing dose-rate. With a longer time between traversals at low dose-rates than at acute dose-rates, the probability of multiple instances of reparable damage existing concurrently becomes negligible as repair processes have long periods of time to act as described by the timeline in Figure 1.

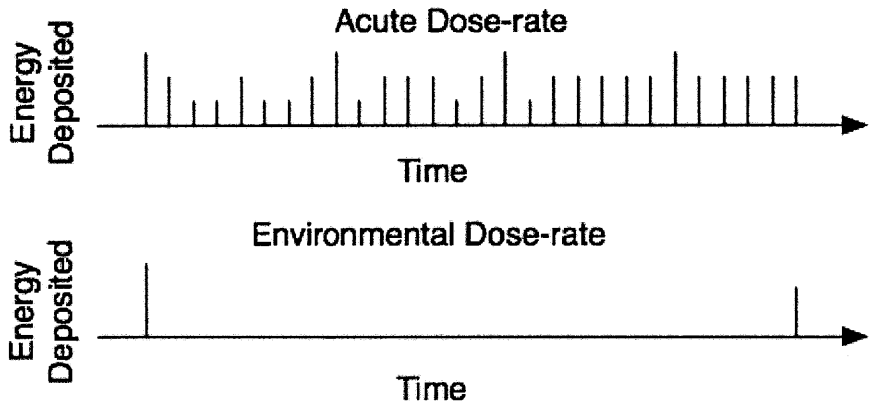

Figure 1. Timelines of energy deposition with magnitude of energy deposited per traversal indicated by height along the vertical axis.

Irreparable damage resulting from the combination of reparable damage caused by multiple traversals will occur at a rate that depends on dose-rate and repair rate. This dependence of the rate of irreparable damage due to multiple traversals is described in detail by Dale [5] based on the numerous observations of the dependence of biological effects on the square of the dose delivered in any time interval. Dale's description of the probability of repair of damage in terms of the time elapsed after a traversal and the repair time constant is used in this model, however his description is inadequate for determining the threshold dose-rate for single traversal damage. This is due to the model's assumption that energy is deposited within a nucleus constantly, rather than in discrete amounts separated in time.

At acute dose-rates the products of the doses corresponding to the traversals which could have caused separate instances of reparable damage is approximately equal to the total dose delivered squared. Many studies have shown a dependence of biological effects proportional to the total dose-squared at acute dose-rates. In order to find the analogous dependence on the products of doses at low dose-rates, it is important to consider how this dose-squared factor arises.

Considering each traversal individually, each depositing a dose d_i, the product, DD, of the doses corresponding to the traversals which could cause separate instances of reparable damage is given by Equation 2 in which N is the total number of traversals, and d is the dose delivered by the ith traversal. In this equation the second term represents the fact that if two reparable instances of damage caused by the same traversal combine to cause irreparable damage this irreparable damage is counted as due to a single traversal rather than multiple traversals.

$$DD = \left(\sum_{i}^{N} d_i \right)^2 - \sum_{i}^{N} d_i^{\,2} \qquad (2)$$

At acute dose-rates, as N becomes large, this expression is approximately equal to D^2. However for low dose-rates, repair occurs concurrently with dose delivery, so the number of instances of reparable damage present concurrently depends on the dose-rate and repair rate, and Equation 2 is not valid. Equation 3 describes the quantity DD for the low dose-rate case. In this equation DD is defined as twice the sum of the products of the doses corresponding to traversals which could cause reparable damage to be concurrently present within a cell, n is the number of traversals which could have caused reparable damage to be present during the time in which the reparable damage resulting from dose d_i is unrepaired.

$$DD = 2\sum_{i}^{N} d_i d_i + d_i d_{i+1} + d_i d_{i+2} + \ldots + d_i d_{i+n} \tag{3}$$

Equation 3 simplifies to Equations 4 and 5, in which the term sd_i represents the total dose delivered by traversals which could cause reparable damage to be concurrently present during the time the damage which could result from the ith traversal is unrepaired. This quantity sd_i may be simulated according to the methods presented in the following sections and is illustrated in Figure 2. This quantity sd_i does not depend on the total dose delivered but rather the dose-rate and repair rate, which is demonstrated in Section 6.6.

$$DD = 2\sum_{i}^{N} d_i \left(d_{i+1} + d_{i+2} + \ldots + d_{i+n}\right) \tag{4}$$

$$DD = 2\sum_{i}^{N} d_i \left(sd_i\right) \tag{5}$$

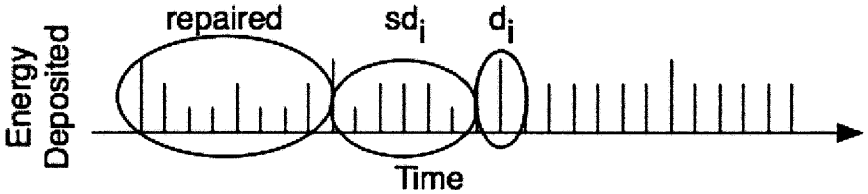

Figure 2. Timelines of energy deposition with magnitude of energy deposited per traversal indicated by height along the vertical axis.

In order to demonstrate that the quantity represented by Equation 5 is proportional to D rather than D^2, it is possible to consider the case in which all traversals deposit the same amount of energy and the same number of instances of reparable damage is present at all times. In this case (Equation 6), the product of doses corresponding to traversals that could cause reparable damage to be concurrently present is seen to be proportional to the total dose D. Further it can be seen that for acute dose-rates at which sd_i is the sum of all dose delivered by traversals prior to traversal i, $\langle sd \rangle = D/2$, and $DD = D^2$.

$$DD = 2\sum_{i}^{N} d_i(sd_i) = 2N\langle d\rangle\langle sd\rangle = 2D\langle sd\rangle \qquad (6)$$

Due to this dependence on the total dose delivered rather than the dose-squared, a measurement of a biological effect that is found to vary with dose at low dose-rate cannot be assumed to be due to single traversal damage alone. For example, Figure 3 describes how measurements of cell survival found to be dependent on dose rather than dose-squared could be mistaken for measurements of cell death due to single traversal damage rather than a combination of single and multiple traversal damage. Care must be taken to avoid attributing any biological result to single traversal damage when attempting to make a measurement of the probability of single traversal damage for comparing biological effectiveness based on this probability.

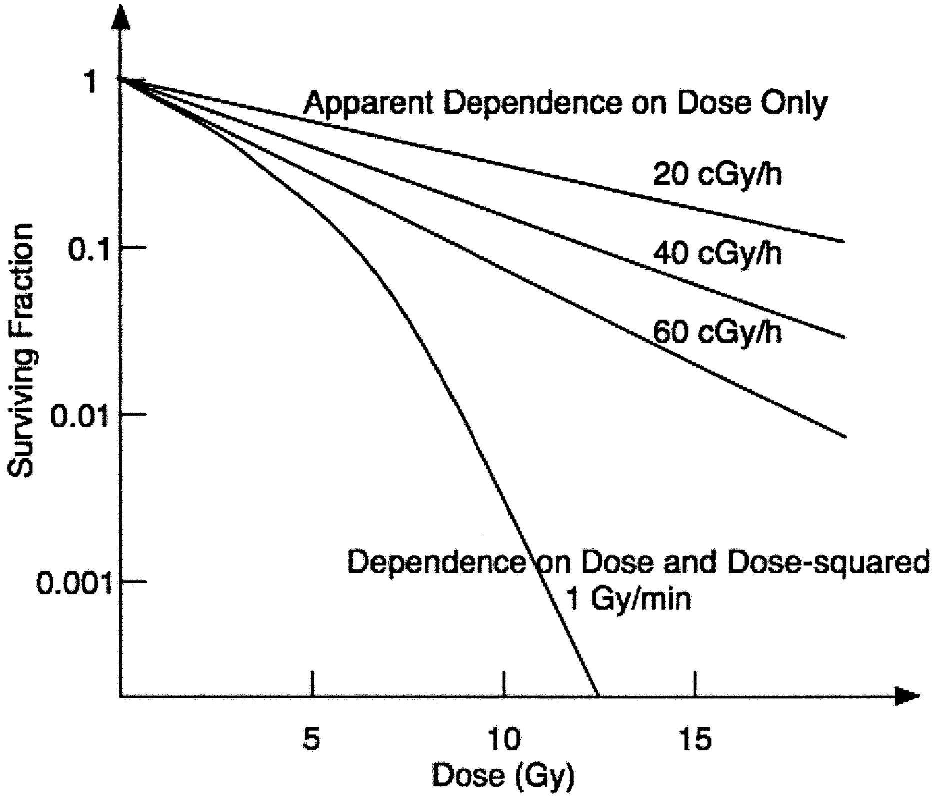

Figure 3. Cell survival curves with linear fit coefficients for several dose-rates.

As illustrated in Figure 3 and explained above, it is possible to measure cell survival data that are only dependent on the total dose rather than dose-squared delivered for several dose-rates. Because of the dependence of multiple traversal damage on total dose rather than dose-squared at low dose-rates, these cell survival curves cannot be used to determine the probability of single traversal damage alone, since some damage may be resulting from multiple traversals.

The following sections outline a method of determining the proportion of damage due to single traversals relative to the damage due to multiple traversals based on measurements of dose-rate, lineal energy transfer, repair rate, and an estimate of the proportion of damage due to single traversals relative to damage due to multiple traversals observed at acute dose-rates.

6.6 Monte Carlo Simulation of Time Delay and Repair Between Energy Deposition Traversals Based on Energy Deposited per Traversal

As discussed above, repair rate and dose-rate influence the relative proportions of single and multiple traversal damage. For a given dose-rate energy will be deposited within a cell nucleus in discrete amounts. The dose-rate and energy deposited per traversal will determine the mean delay between traversals. This section describes a method of determining the dependence of the proportions of single and multiple traversal damage based on dose-rate, mean energy deposited per traversal, repair rate, and measurements of these proportions at acute dose-rates.

Using the calculation of the proportions of single and multiple traversal damage, a method is presented for determining a dose-rate below which multiple traversal damage is negligible for the purpose of performing experiments for determining RBE at dose-rates below these levels.

Radioactive decay can be modeled as a Poisson process with a mean number of decays per unit time determined by the dose-rate of the field in question and the energy deposition data calculated using MCNP. By sampling an appropriate Poisson distribution of time delays between traversals determined by the dose-rate and energy deposited per traversal, histories including energy deposited per traversal and time between traversals were generated.

Several values of dose-rate, repair rate, and energy deposited per traversal were considered. In order to define an appropriate Poisson distribution for sampling the time between traversals, the mean number of traversals per unit time, $<H_T>$, was determined based on the dose-rate, R, the mean energy deposited per traversal, E_H, and the mass of the cell nucleus, M_C. which was assumed to be equal to 1.13×10^{-13} kg for a cell nucleus of diameter 6 μm (an approximate value for mammalian cells [1]).

$$\langle H \rangle = \frac{RM_C}{\langle E_H \rangle} \tag{7}$$

The Poisson distribution defined by this mean traversal rate was then used to sample the time delay between traversals in order to generate traversal histories. For each value of dose-rate and energy deposited per traversal considered, 100,000 traversal histories were simulated.

For each traversal in these histories, the probability of damage repair was also sampled at the time point of future traversals. The probability of repair was chosen based on the work of Dale [5], who describes the probability, P_{repair}, of an instance of damage being repaired at time t after the damage occurs as a function of μ, the repair time constant:

$$P_{repair} = 1 - e^{-\mu t} \tag{8}$$

This dependence of repair on time has been observed experimentally. For example, Cleaver et al. measured the repair of DNA strand breaks in Chinese Hamster V79 cells for exposure to tritiated water and found this relation to hold with at time constant $\mu = 7.7 \times 10^{-4}$ s^{-1}[11].

Although Dale derives expressions for the amounts of damage due to single and multiple traversals, this work is based on the assumption that energy is deposited within a cell continuously rather than in discrete amounts. As dose-rate decreases, this assumption cannot hold.

In model of Dale there is no allowance for differences in the proportions of single and multiple traversals due to differences in energy deposited per traversal. In order to demonstrate that energy deposited per traversal does influence the ratio of the probability of multiple traversal damage to the probability of single traversal damage, a set of 120 traversal histories were simulated. The results of the simulations of the ratio of the products of doses which could have caused reparable damage to be concurrently present to total dose delivered was calculated as a function of mean energy deposited per traversal.

The results are described in terms of mean lineal energy transfer rather than mean energy deposited per traversal using the relative of Kliauga and Dvorak [7], who describe the lineal energy for a sphere of diameter d in μm and a mean dose per traversal of z in cGy as in Equation 9:

$$y = 0.049d^2z \tag{9}$$

For this calculation d was chosen to be 6 μm, the diameter of a typical mammalian cell [1]. This choice was made for convenience, since lineal energy transfer is a quantity that can be measured experimentally for any radiation field using microdosimetry methods.

The results of these simulations for several different values of dose-rate and mean energy deposited per traversal described in terms of linear energy transfer in Figure 4. All data points in this figure had relative uncertainties of less than 0.02.

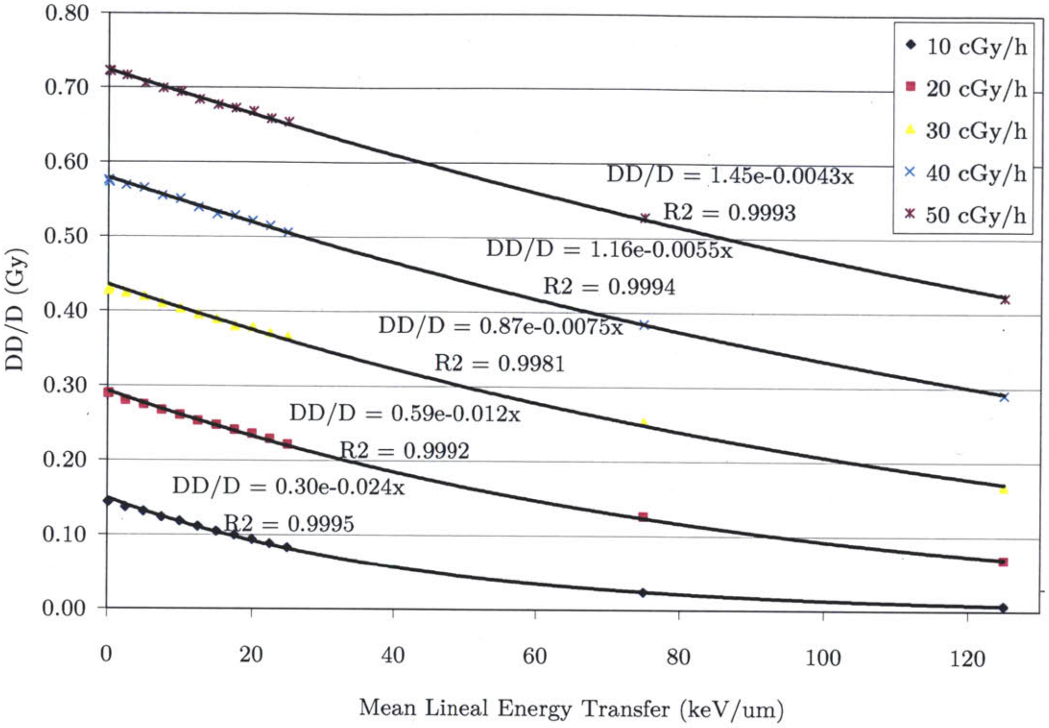

Figure 4. Values of DD/D for various dose-rates and lineal energy transfer values with a repair half-time of 1 hour.

By fitting these data and similar data for a repair half-time of 30 minutes to an exponential function, the relation for the ratio of multiple traversal damage to single traversal damage was found to be as described by Equation 10:

$$\frac{N_{multiple}}{N_{single}} = \frac{2R}{\mu}\frac{\beta}{\alpha}e^{-\frac{0.00342\mu}{RD_H}} \tag{10}$$

It should be noted that only the frequency mean of lineal energy transfer is important in determining this threshold dose-rate rather than the exact lineal energy transfer distribution. This was verified by simulating the ratio of single traversal damage to multiple traversal damage for different distributions of energy deposited per traversal but with the same mean value of energy deposited per traversal. For each distribution the same ratio resulted.

The threshold dose-rate, R_T, for which this fraction is less than a threshold L can be found by rearranging Equation 11:

$$R_T = \frac{0.00342\mu}{D\,ProductLog\left[\frac{0.00684\beta}{LD_H\alpha}\right]} \tag{11}$$

Below some threshold fraction, L (for example 0.05), damage due to multiple traversals is negligible compared to damage due to single traversals. Any comparison of the total effect per unit dose is then a comparison of the effect due to single traversals for the fields in question. This comparison of the effect per unit dose for each field determines RBE for the dose-rates used to observe the effect as well as dose-rates below this level, since the probability of single traversal damage is assumed not to change with dose-rate. In the following section this relation will be used to design an experiment for determining RBE for dose-rates below 1 cGy/h.

6.7 Determining RBE for Dose-rates <1 cGy/h

With an estimate of the threshold dose-rate below which multiple traversal damage is negligible, it is possible to determine the relative biological effects due to single traversal damage only. Based on the assumption of this model that the probability of effects due to single traversals per unit dose does not vary with dose-rate (as described in Section 6.2), it is then possible to predict the RBE between two fields for all dose-rates below this threshold dose-rate using biological data from exposures at or below this threshold.

In order to predict RBE for all dose-rates below this threshold dose-rate, the threshold dose-rate for each field should be calculated based on experimental measurements of lineal energy transfer, repair half life, and an estimate of the ratio of the probability of effect per unit dose-squared to the probability of effect per unit dose.

For each field lineal energy transfer can be measured using microdosimetry or referenced from literature sources if available. This method provides the advantage that RBE may be determined for any arbitrary field of mixed sources which may be encountered in industrial contamination for example.

For determining the threshold dose-rate for these fields, lineal energy transfer should be measured experimentally since literature sources are limited for mixed fields.

For tissue culture experiments the repair half life has been measured for many cell lines and radiation fields, and these data may be used if they are available for the cell line of interest. For animal experiments the repair half life can be estimated based on the known maximum repair half life observed for the organism of interest. The maximum repair half life should be used since the tissue with the maximum repair half life will have the greatest probability of having concurrent instances of reparable damage.

The ratio of the probability of effect per unit dose-squared to the probability of effect per unit dose (β/α) can be measured if acute exposures are possible, but in instances in which this is not possible, an estimate of the upper bound of this ratio can be based on data measured for the same biological sample with similar fields.

An estimation based on these results is justified since at acute dose-rates $DD=D^2$, and in this case the probability of irreparable damage due to multiple traversals per unit dose-squared measured in these experiments is seen to be the same quantity of interest at low dose-rates. Although the acute dose-rates at which these probabilities were observed are greatly different from dose-rates less than 1 cGy/h, it is important to recognize that the same physical dynamics determine these probabilities independent of dose-rate. The probabilities of cell kill per unit dose (single traversal damage) measured at acute dose-rates and low dose-rates were compared by Peacock et al. and shown to be within statistical uncertainty in most cases [14]. Similarly for damage due to multiple traversals, dose-rate does not influence the distance between the locations of any two energy traversals locations or the probability that damage resulting from these traversals will interact. Dose-rate only influences the number of concurrent instances of reparable damage, which has been accounted for in the calculations of DD presented above. The use of the β/α parameter also has advantages over the use of other parameters such as measurements of the number of DNA strand breaks per unit dose since a large dataset of these parameters is readily available from decades of literature reports.

With all these quantities determined using experimental data, the threshold dose-rate can be determined using Equation 11. Measurements of biological effects due to the fields in question can then be conducted at a dose-rate at or below this threshold dose-rate. If data are available for the biological sample of interest for a suitable reference field at a dose-rate below the threshold, then the dose-rate of the field in question can then be matched to this dose-rate to perform the biological assay of interest.

Any effects observed can be assumed to be due to single traversal damage, and therefore any comparison of the relative biological effects should hold for reduced dose-rates. Thus the RBE determined at this threshold dose-rate can then be assumed valid for all lesser dose-rates

By performing these measurements, the RBE of fields with dose-rates <1 cGy/h can be determined using the same energy spectrum at dose-rates 10-50 cGy/h, depending on the parameters measured. Advantages of this method are described in Section 6.8, and verification of this method is described in Section 6.9.

6.8 Advantages of Projecting Biological Effectiveness at Environmental Dose-rates Based on Low Dose-rate Biological Data

For some radiation fields it is possible to make an estimate of the probabilities of single traversal damage based on cell survival results at acute dose-rates. Using these probabilities, an estimate of the RBE of these fields can be made. However for some radiation sources it may not be possible or practical to measure biological effects at acute dose-rates. Several source characteristics may make measurement of biological effects at low dose-rates the best or only option for estimating the probability of single traversal damage per unit dose.

For photon-emitting radioactive isotopes which have a large half-life value (i.e. >100 years), the number of decays per unit mass may result in self attenuation by the source. This self attenuation would alter the energy spectrum of the photons emitted, resulting in a different field than exposures at low dose-rates would allow. For example in the case of ^{232}Th, which has a half-life of 1.405×10^{10} years and a mean photon energy of 60 keV [21]. This self attenuation is of particular importance if internal exposures are being considered, since there would be no attenuation by the source in this case.

For sources which emit β particles with a shorter range than photons, self attenuation is also a concern even for sources with a shorter half-life (less than 1 year). Also for experiments with animals with these isotopes, since it is necessary for time to elapse to allow for uptake of β emitting radioisotopes, and these isotopes cannot be purged from animals immediately, exposures at acute dose-rates of ~1 Gy/min are not biologically possible.

In other situations in which a limited quantity of an isotope is available due to half-life, expense, or safety/security considerations, it may be impractical to assemble a large enough amount of an isotope to perform an acute exposure.

One situation in which this method is particularly applicable is in the instance of determining RBE for mixed fields for which dose may be delivered by different types of particles. For fields for which photons deposit a significant portion of the total dose delivered, but heavy charged particles also contribute to dose, the need for the determination of the threshold dose-rate is most clear. It cannot be assumed that no multiple traversal damage is possible for these fields, since the β/α ratio for photons is nonzero. The dose-weighted mean of lineal energy transfer for such a field would be greater than the lineal energy transfer for pure-photon fields, leading to a greater value for the threshold dose-rate for these fields. This ability to perform experiments at the greatest possible dose-rate may provide the ability to measure some effects which would not be possible at lower dose-rates. For example in the study of Pettersen et al., changes in cell survival were unobservable at a dose-rate of 1.5 cGy/h, but were observable at 6.15 cGy/h [25].

In all these situations, determination of the probability of single traversal damage is best accomplished with low dose-rate exposures. In order to measure this probability effectively, without mistaking effects due to multiple traversals for traversals due to single traversals, it is necessary to perform these experiments at an appropriate dose-rate. This threshold dose-rate for single traversal damage as calculated by the methods presented above provides an upper limit for dose-rate for these exposures.

Knowledge of this upper limit provides the ability to observe biological effects at a maximum dose-rate at which multiple traversal damage is negligible. This ability to maximize the dose-rate at which biological effects are observed provides the ability to observe some effects that would otherwise have been unobservable.

The methods described in this chapter provide a means of estimating these probabilities, allowing for biological data at low dose-rates to be used to determine the relative probabilities of irreparable damage due to single traversals for different fields. These probabilities can then be used to estimate the relative biological effectiveness for these fields at environmental dose-rates at which damage due to multiple traversals is negligible.

6.9 Verification of RBE Values Found at Low Dose-rate Using Literature Sources

Ueno et al. analyzed survival of L5178Y mouse lymphocytic leukemia cells after exposure to ^{60}Co and tritiated water at low dose-rates [3]. RBE values of 1.4-1.6 were estimated based on 50% survival after irradiation at 12 cGy/h with both fields. This estimate of RBE is comparable to the RBE value of 1.7 reported by Furchner et al. for $LD_{50(30)}$ for ^{60}Co and tritiated water [18]. In this study CF1 mice were exposed to tritiated water at ^{60}Co photons at a dose-rate matching the dose-rate delivered by the tritiated water.

Another example for which two fields were analyzed with different endpoints is the work of Fairchild et al. and Dean et al. Fairchild et al. have estimated the RBE of ^{252}Cf to ^{226}Ra to be 2.86 based on survival of HeLa cells at 31 cGy/h [19]. Dean et al. estimate the RBE of ^{252}Cf to ^{228}Ra to be 3.01 for $LD_{50(30)}$ survival of mice [20]. At the dose-rate 31 cGy/h, it can be assumed that most of the reproductive cell death is the result of damage due to single traversals, based on the threshold dose-rate discussed in Section 6.6. In this case, these values of RBE vary within 10%, confirming the importance of a measurement of damage due to single traversals.

Although the correlation in these example does support the link between relative biological effects and the probability of damage due to single traversals per dose observed near the threshold dose-rate, more data are needed to firmly establish this link. In order to test the correlation of the probability of damage due to single traversals with other biological effects, more data comparing survival between two fields at dose-rates near the threshold dose-rate under controlled conditions are needed. More data comparing biological effects in vivo for the same fields would also be needed.

6.10 References

1. B. Alberts, P. Walter, Molecular Biology of the Cell, 4th Edition, Chapter 4, 191-234, (Garland Science, New York, 2002).
2. Goodhead, Advances in Radiation Biology, 16, 1992, 7-45.
3. C. Stecca, G. B. Gerber, Biochemical Pharmacology, 7, 1, 1998, 941-951.
4. A. M. Ueno, I. Furuno-Fukushi, H. Matsudaira, Radiation Research, 91, 1982, 447-456.
5. R.G. Dale, British Journal of Radiology, 58, 1985, 515-528.
6. J. C. McDonald, I. Ma, L. Zeitz, Radiation Research, 77, 1979, 221-232.
7. P. Kliauga, R. Dvorak, Radiation Research, 73, 1978, 1-20.
8. G. Muhrer, E.J. Pitcher, G.J Russell, F. Maekawa, Y. Kasugai, and H. Takada, Nuclear Instruments and Methods B, 547, 2-3, 2005, 555-568.
9. E. Browne and R.B. Firestone, Table of Radioactive Isotopes, ed. V.S. Shirley, (Wiley, New York, 1986).
10. J. Morton, H. Yabuki, E. A. Porter, S. Rockwell, R. Nath, Radiation Research, 119, 1989, 478-488.
11. J. E. Cleaver, G. H. Thomas, H. J. Burki, Science, 177, 4053, 1972, 996-998.
12. R. Nath, P. Bongiorni, Z. Chen, J. Gragnano, and S. Rockwell, Radiation Research, 163, 2005, 501-509.
13. D. T. Goodhead, International Journal of Radiation Biology, 65, 1, 1994, 7-17.
14. J. H. Peacock, J.J. Eady, S. M. Edwards, T. J. McMillan, and G.G. Steel, International Journal of Radiation Biology, 61, 1992, 479-487.
15. H. D. Thames, S. M. Bentzen, I. Turesson, M. Overgaard, and W. Ven Den Bogaert, International Journal of Radiation Biology, 56, 5, 1989, 701-710.
16. R. B. Tishler, C. R. Geard, International Journal of Radiation Oncology Biology Physics, 21, 1991, 975-982.
17. R. L. Wells and J. S. Bedford, Radiation Research, 94, 1983, 105-134.
18. J. F. Furchner, Radiation Research, 6, 1957, 483-490.

19. R. G. Fairchild, R. M. Drew, and H. L. Atkins, Radiology, 96, 1970, 171-174.

20. F. K. Dean, S. C. Bushong, N. Prasad, and S. Briney, Radiology, 104, 1972, 699-703.

21. L. Lacoste-Collin, S. Jozan, V. Cances-Lauwers, B. Pipy, G. Gasset, C. Caratero, M. Courtade-Saidi, Radiation Research, 168, 6, 2007, 725-732.

22. C. C. Ling, W. X. Li, and L. L. Anderson, International Journal of Radiation Oncology, Biology, Physics, 32, 2, 1995, 373-8.

23. E. J. Hall, W. Gross, R. F. Dvorak, A. M. Kellerer, and H. H. Rossi, Radiation Research, 52, 1972, 88-98.

24. C. J. Roberts, D. T. Goodhead, International Journal of Radiation Biology and Related Studies in Physics Chemistry and Medicine, 52, 6, 1987, 871-882.

25. E. O. Pettersen, I. Bjorhovde, A. Sovik, N. F. J. Edin, V. Zachar, E. O. Hole, J. A. Sandvik, and P. Ebbesen, International Journal of Radiation Biology, 83, 5, 2007, 331-345.

26. J. M. Ruiz de Almodovar, C. Bush, J. H. Peacock, G.G. Steel, S. J. Whitaker, and T. J. McMillan, Radiation Research, 138, 1994, S93-S96.

27. J. Valentin, Annals of the ICRP, 92, 2003.

28. E. C. Friedberg, G. C. Walker, W. Siede, R. D. Wood, R. A. Schultz, and T. Ellenberger, DNA Repair and Mutagenesis, 2nd Ed., (ASM Press, Washington, DC, 2006).

Chapter 7: Conclusion and Future Work

7.1 Summary of Conclusions

In this study ^{241}Am sources have been used to create irradiators for tissue culture and animal experiments. In order to use these ^{241}Am foils for biological work, a complete physical characterization of the energy spectrum and dose delivered by the sources was necessary. Since there no spectrometer exists with constant efficiency across the 10-60 keV energy range, and there is no standard source for dosimetry of unshielded ^{241}Am, new methods were developed for measuring the photon energy spectrum and dose delivered by the sources.

The best estimate of the photon energy spectrum emitted by the ^{241}Am foils was established using two spectrometers and literature data. The method for measuring this spectrum was also used to measure energy spectra for several shielding configurations. Chapter 2 provides a description of this method and the energy spectra of the ^{241}Am foils for various shielding configurations.

The best estimate of the dose delivered by the ^{241}Am foils was established using two dosimeters with corrections for energy efficiency based on experimental measurements and MCNP simulation. The maximum dose-rate delivered by a single ^{241}Am foil was measured to be 2.01 ± 0.12 cGy/h. These methods and results are reported in Chapter 3.

With the best estimates of the photon energy spectrum and dose-rate measurements established, the ^{241}Am foils were incorporated into irradiators for tissue culture experiments. Two irradiators were designed to deliver dose-rates of 0.28 ±0.02 cGy/h with significantly different photon fields. Tissue culture experiments were conducted using these irradiators in order to compare the biological effectiveness of the photons emitted by ^{241}Am. These experiments showed that the relative biological effectiveness for the two photon fields was greater than 2.0. These biological results were compared with theoretical models of biological effectiveness. A model of biological effectiveness incorporating MCNP-simulated secondary electron spectra was also proposed. The tissue culture irradiators and these results are reported in Chapter 4.

Since the biological effects of low energy low dose-rate radiation cannot be fully understood with tissue culture work alone, animal irradiators incorporating the

^{241}Am foil sources were also designed. In order to achieve maximum experimental flexibility, several foil configurations were considered. The mean dose-rates delivered by these configurations ranged from 0.046 ± 0.002 to 0.50 ± 0.03 cGy/h. Chapter 5 describes these configurations and a shielding apparatus for maintaining the safety of laboratory workers.

In summary the methods described in this thesis provide a means of determining RBE for low dose-rate fields based on biological exposures at low dose-rates rather than estimating RBE based on data obtained at acute dose-rates. The methods provide solutions to important problems of measuring low energy photon spectra accurately and performing accurate dosimetry of low energy photon fields with OSL dosimeters. These methods can be adapted and applied to low energy photon fields other than those based on ^{241}Am.

The model describing energy deposition in a cell nucleus at low dose-rates provides a basis for estimating the RBE for a wide range of low dose-rates using any determination of RBE based on exposures at dose-rates below a threshold value. Several important advantages to using data from low dose-rate exposures instead of acute exposures to determine RBE for other low dose-rate fields are discussed in order to motivate further investigation into RBE at low dose-rates.

7.2 Recommendations for Future Work

The ^{241}Am irradiators described in this project provide a platform for biological experiments which could add to the understanding of the biological impact of low dose-rate low-energy photon radiation. Further tissue culture experiments with the photon fields considered in this study could yield valuable information about the biological response of 10-30 keV photons relative to 60 keV photons. Further experimentation with different cell types could also yield valuable data that could influence the development of models for describing biological effectiveness for photons in this energy range.

The methods used for physical characterization of the sources used in this study could also be applied to other isotope sources for which dosimetry standards do not exist. By characterizing other isotope sources with photons in the 10-100 keV energy range, more irradiators could be developed. With these irradiators, a greater understanding of the relative biological effectiveness of photons in the 10-100 keV range could be achieved.

The methods used to develop tissue culture irradiators with different photon fields and equal dose-rates could also be used to develop different photon fields with the animal irradiator. Animal experiments could be used to determine the relative biological effectiveness of these photon fields for long-term experiments that could not be conducted with tissue culture.

Further biological experiments with both tissue culture and animals at low dose-rates could confirm that RBE does not vary with dose-rate below a certain threshold dose-rate as predicted by the model described in Chapter 6.

Appendix A: Weighting Dose Measurements at the Animal Platform Surface

In Table A1, dose weighting factors are listed along with location coordinates for each dose measurement made on the surface of the animal irradiator. Coordinates are given relative to the origin as described in Chapter 5 Figure 5.

X location	Y location	Weighting Factor
2	-18	0.015
2	-10	0.0225
2	0	0.025
2	10	0.0225
2	18	0.015
10	-18	0.0225
10	-10	0.03375
10	0	0.0375
10	10	0.03375
10	18	0.0225
20	-18	0.025
20	-10	0.0375
20	0	0.041667
20	10	0.0375
20	18	0.025
30	-18	0.025
30	-10	0.0375
30	0	0.041667
30	10	0.0375
30	18	0.025
40	-18	0.025
40	-10	0.0375
40	0	0.041667
40	10	0.0375
40	18	0.025
50	-18	0.0225
50	-10	0.03375
50	0	0.0375
50	10	0.03375
50	18	0.0225
58	-18	0.015
58	-10	0.0225
58	0	0.025
58	10	0.0225
58	18	0.015

Table A1. Weighting factors for the dose measurement on the animal platform surface.